University of Rzeszow

SCIENTIFIC DISCIPLINE PHYSICAL SCIENCES

DOCTORAL THESIS

Photon induced processes for LHC and EIC energies

Author: Barbara Linek

Supervisor: Prof. Marta Łuszczak, PhD, DSc

Completed in: Doctoral School of the University of Rzeszow

Rzeszów, 2024

Acknowledgements

First of all, I would like to express my sincere gratitude to my Supervisor, dr hab. Marta Łuszczak, Prof. UR for her invaluable assistance and support throughout the entire process of preparing my doctoral thesis. It was thanks to your inspiration and encouragement that I decided to pursue doctoral studies in the field of elementary particles, which turned out to be one of the most important decisions of my academic life.

Your support, both substantive and organizational has been incredibly valuable to me. I am grateful for your constant help with the preparation of documentation, involvement in formal matters, and financial support, which enabled me to participate in research internships, conferences, and trips for scientific consultations. Thanks to you, I had the opportunity to develop in an international research environment, which allowed me to broaden my horizons and gain valuable experience.

I would like to express my gratitude to dr hab. Wolfgang Schäfter, Prof. IFJ PAN for his unwavering support, generous assistance, and extraordinary patience with my many questions, as well as for hosting me at the Institute of Nuclear Physics Polish Academy of Science. His guidance and insightful advice have been invaluable, increasing my understanding and inspiring new strategies during my doctoral studies.

Special thanks also go to Prof. dr hab. Antoni Szczurek, for his support in substantive aspects as well as beyond science. Your support in difficult times and ability to remedy problems, similar to your great optimism, has enormously influenced where I am now.

I am also grateful to dr Izabela Babiarz, dr hab. Mariola Kłusek-Gawenda, Prof. IFJ PAN, dr. hab Piotr Lebiedowicz, and Paweł Jucha for their patience and support but also great atmosphere during my every visit.

I would also like to thank Roman Pasechnik from the Department of Astronomy and Theoretical Physics at Lund University, dr hab. Agnieszka Łuszczak, Prof. PK from the Department of Physics at the Faculty of Materials Science and Physics of the Cracow University of Technology, Bernhard Holzer from the European Organization for Nuclear Research, and Laurent Forthomme from AGH University of Krakow for hosting me during my internships and scientific consultations.

I am also grateful for financial support through grants with decision numbers:

- 31/NAWA-PROM-UR/2019,
- NIG/23/2023.

Abstract

This dissertation discusses various photon-induced processes for the LHC and EIC energies. It discusses the processes of production of charged lepton pairs in two-photon exchange and the production of diffraction dijets in electron-proton collisions.

The former mechanism has been considered in the context of muon and electron production in proton-proton collisions and refers to experimental data, explaining the reasons for the occurrence of a small number of leptons in the region of small rapidities (close to 0.0) and large invariant masses (300 - 1000 GeV). As part of this analysis, as in the case of the proton-yield collisions included further in the paper, different photon structure functions in the proton were included, as part of which the Kulagin-Barinov model was compared to experimental data for the first time. On the other hand, the amplitude of the studied processes was formulated according to the transverse factorization approach with the help of wave functions of bound states on the light cone. The influence of rapidity gap survival effects was also taken into account in both cases making it possible to exclude the involvement of diffraction dilepton production mechanisms.

The discussion further included the processes of jets production in proton-nucleus and electron-proton collisions. As part of it, six models of the unintegrated parton distribution functions in the proton were compared, four of which were subjected to a double Fourier-Bessel transform in order to go into the transverse momentum space of the produced quarks. This procedure made it possible to highlight the imperfections of the models fitted to the data, and the need to take into account additional mechanisms to correctly reproduce the experiments carried out on the HERA collider. In addition, correlations in the azimuthal angle were analyzed, showing their origin to be associated with elliptical unintegrated gluon distributions in the proton as well, as superimposed kinematic cuts.

The posted conclusions are based on the analysis of experimental data and theoretical models and indicate the need for further in-depth study of hadron structure, especially in the context of processes involving pomeron exchange.

Streszczenie

Niniejsza rozprawa omawia wybrane procesy indukowane fotonami dla energii akceleratorów LHC i EIC. Zbadano w niej procesy produkcji dwufotonowej par naładowanych leptonów oraz produkcję dijetów dyfrakcyjnych w zderzeniach elektron-proton.

Pierwszy z wymienionych mechanizmów został rozważony w kontekście produkcji mionów i elektronów w zderzeniach proton-proton. Odnosi się do danych eksperymentalnych, wyjaśniając przyczyny występowania niewielkiej ilości leptonów w obszarze małych rapidity (bliskich 0.0) i dużych mas niezmienniczych (300 - 1000 GeV). W ramach tej analizy, podobnie jak w przypadku zderzeń proton-jadro zamieszczonych dalej w pracy, uwzględniono różne funkcje struktury fotonów w protonie, w ramach czego po raz pierwszy porównano do danych eksperymentalnych model Kulagin-Barinov. Natomiast amplituda badanych procesów została sformułowana zgodnie z podejściem faktoryzacji poprzecznej z pomocą funkcji falowych stanów związanych na stożku świetlnym. Uwzgledniony został w obydwu przypadkach także wpływ efektów przeżycia przerwy w rapidity umozliwiający wykluczenie udziału mechanizmów dyfrakcyjnej produkcji dileptonów.

Dyskusji poddano także procesy produkcji jetów w zderzeniach proton-jądro oraz elektron-proton. W jej ramach porównano sześć modeli uogólnionych funkcji rozkładu gluonów w protonie, z których cztery poddano podwójnej transformacie Fouriera-Bessela celem przejścia do przestrzeni pędów poprzecznych produkowanych kwarków. Zabieg ten pozwolił na uwidocznienie niedoskonałości dopasowanych do danych modeli oraz konieczność uwzględnienia dodatkowych mechanizmów w celu poprawngo odwzorowania przeprowadzonych na zderzaczu HERA eksperymentów. Dodatkowo analizie poddano korelacje w kącie azymutalnym wykazując ich pochodznienie powiązane w eliptycznymi nieprzecałkowanymi rozkładami gluonów w protonie, jak również z nakładanymi cięciami kinematycznymi.

Zamieszczone wnioski oparte są na analizie danych eksperymentalnych oraz modeli teoretycznych i wskazują na konieczność dalszego, dogłębnego badania struktury hadronów, szczególnie w kontekście procesów uwzględniajacych wymianę pomeronu.

Preface

When the first research related to the creation of this dissertation was conducted it was known that at high energies gluon-gluon fusion was the dominant mechanism for the production of heavy quarks. The role of additional mechanisms for particle production, including the role of photon processes, had also already begun to be analyzed. The role of inelastic photon contributions to the production of W^+W^- pairs was estimated. In order to better understand the role of photons in hard processes, a new approach was proposed in which, for the first time in the literature, the transverse momentum of the incoming photons was taken into account. Functions of the unperturbed distributions of photons in the proton were developed. The probabilities of surviving the hastiness gap were estimated for the W^+W^- pair production process and for the quark-antiquark ($t\bar{t}$) pair production process initiated via a photon-photon fusion mechanism.

The goal of this work is to theoretically investigate selected photon-induced processes occurring in collisions of leptons, hadrons, and atomic nuclei in the high-energy region. As part of the analysis, completely new methods will be developed and unique calculations will be made on the exclusive processes of the production of a small number of Standard Model elementary particles in the output channel. These processes have not been analyzed in detail in the literature so far, because it was assumed that their contribution to particle production is negligible. There was also no way to measure these processes experimentally.

The motivation for studying exclusive and semi-exclusive processes in electron-proton and electron-nucleus collisions is the construction of the Electron-Ion Collider (EIC) at Brookhaven Laboratory in the USA. It will study electron-proton and electron-nucleus collisions over a wide range of energies: $20 < \sqrt{s} < 140\,\mathrm{GeV}$. Given the approximately thousand times higher luminosity of the new EIC, consideration has also been given to the convenience of verifying existing theoretical models describing exclusive and semi-exclusive processes within the framework of quantum chromodynamics (QCD).

The outline of thesis

- Chapter 1 describes the basic properties of collisions of elementary particles, as well as mentions methods for describing the structure of these particles based on the transverse factorization approach and Wigner distributions. It also includes information on operating and future particle colliders, which, in sum, provides an introduction to the further analyses presented in this dissertation;

- Chapter 2 describes the production of lepton pairs in proton-proton and proton-nucleus collisions, taking into account the photon's contribution to the parton structure of protons, based on the $k_\perp$-factorization approach. Considered kinematics corresponds to the ATLAS (A Toroidal LHC Apparatus) and ALICE (A Large Ion Collider Experiment) collaborations, working at the Large Hadron Collider (LHC);

- Chapter 3 refers to the production of charm quark-antiquark pairs in proton-nucleus collisions, again referring to the high energies obtained at the LHC. This analysis does not refer to experimental data but shows the results that are possible to measure based on the color dipole approach. This chapter also includes the contribution of photon-induced processes and the comparison of the contribution of both mentioned mechanisms;

- Chapter 4 incorporates the color dipole approach in the analysis of dijet production in electron-proton collisions regarding experimental data presented by the H1 and ZEUS collaborations worked at the experiments from 1992 to 2007 at the Hadron-Electron Ring Accelerator (HERA). This chapter not only compares the results obtained using various models available in the literature but also presents the predictions of these models for analogous production in EIC;

- Chapter 5 is a summary of the entire work and the conclusions drawn from it.

List of the scientific achievement

In general, this dissertation is written based on the following scientific articles, to which the author of the thesis made a significant contribution published in 2021-2024 in international scientific journals:

- [1] A. Szczurek, B. Linek, and M. Łuszczak, *Semiexclusive dilepton production in proton-proton collisions with one forward proton measurement at the LHC*, Phys. Rev. D **104**, 074009;
- [2] B. Linek, M. Łuszczak, W. Schäfer, A. Szczurek, *Production of e^+e^- in proton-lead collision: Photon-photon fusion*, Phys. Rev. D **106**, 094034 ;
- [3] B. Linek, A. Łuszczak, M. Łuszczak, R. Pasechnik, W. Schäfer and A. Szczurek, *Probing proton structure with $c\bar{c}$ correlations in ultraperipheral pA collisions*, JHEP 10 (2023) **179**;
- [4] B. Linek, M. Łuszczak, W. Schäfer, A. Szczurek, *Probing gluon GTMDs of the proton in deep inelastic diffractive dijet production at HERA*, Phys. Rev. D **110**, 054027;

The following post-conference articles were also created based on these analyses:

- [5] A. Szczurek, B. Linek, and M. Łuszczak, *Central dilepton production in proton-proton collisions with rapidity gap and with forward protons*, SciPost Physics, arXiv:2107.13294v1;
- [6] A. Szczurek, B. Linek, and M. Łuszczak, *Production of dileptons via photon-photon fusion in proton-proton collisions with one forward proton measurement*, Proceedings of Science, arXiv:2111.06627v1;
- [7] B. Linek, *Semiexclusive dilepton production in proton-proton collisions with one forward proton measurement at the LHC*, Proceedings of the Low-x 2021 International Conference, arXiv:2206.11264v1;
- [8] B. Linek, M. Łuszczak, W. Schäfer, A. Szczurek, *Two-photon fusion production of e^+e^- in proton – lead collision*, A. Phys. Pol. B Supp. 16(7) A29;

it was also extended to include results not included in the above-mentioned publications.

Active participant in conferences and schools

- B. Linek, M. Łuszczak, A. Szczurek, *Semi-exclusive dilepton production in proton-proton collisions with one forward proton measurement at the LHC*, Multidyscyplinarna Konferencja Doktorantów Uniwersytetu Szczecińskiego 2.0, 23-25.06.2021, Szczecin/online;
- B. Linek, M. Łuszczak, W. Schäfer, A. Szczurek, *Production of dileptons via photon-photon fusion in proton-proton collisions with one forward proton measurement at the LHC*, LXI Cracow School of Theoretical Physics, 20-24.09.2021, Cracow/online;
- B. Linek, M. Łuszczak, W. Schäfer, A. Szczurek, *Semi-exclusive dilepton production in proton-proton collisions with one forward proton measurement at the LHC*, Low–x 2021, 26.09-1.10.2021, Portoferraio/online;
- B. Linek, M. Łuszczak, W. Schäfer, A. Szczurek, *Analiza semi-ekskluzywnej produkcji dileptonu w zderzeniach proton-proton z pomiarem jednego protonu na detektorze protonów do przodu*, XV Rzeszowska Konferencja Młodych Fizyków, 1.07.2022, Rzeszow, Poland;
- B. Linek, M. Łuszczak, W. Schäfer, A. Szczurek, *Production of* e^+e^- *in proton-lead collision at the LHC energy*, New Vistas in Photon Physics in Heavy-Ion Collisions, 19-22.09.2022, Cracow, Poland;
- B. Linek, M. Łuszczak, W. Schäfer, A. Szczurek, *Two-photon fusion production of* e^+e^- *in proton-lead collision*, XXIX Cracow EPIPHANY Conference, 16-19.01.2023, Cracow, Poland;
- B. Linek, M. Łuszczak, W. Schäfer, A. Szczurek, *Produkcja par* e^+e^- *w zderzeniach proton ołów przy energiach akceleratora LHC*, XVI Rzeszowska Konferencja Młodych Fizyków, 2.06.2023, Rzeszow, Poland;
- B. Linek, *Photon included processes at LHC energy*, XIV Trans-European School of High Energy Physics, 14-22.07.2023, Bezmiechowa Górna, Poland;
- B. Linek, A. Łuszczak, M. Łuszczak, R. Pasechnik, W. Schäfer, A. Szczurek, *Study of proton structure using* $c\bar{c}$ *correlation in ultraperipheral* pA *collisions, Forward Physics in ALICE 3*, 18-20.10.2023, Heidelberg, Germany;

- B. Linek, M. Łuszczak, W. Schäfer, A. Szczurek, *Dyfrakcyjna produkcja didżetów w akceleratorze HERA z wykorzystaniem GTMD*, XVII Rzeszowska Konferencja Młodych Fizyków, 6-7.06.2024, Rzeszow, Poland;
- B. Linek, M. Łuszczak, W. Schäfer, A. Szczurek, *Diffractive dijets at HERA and EIC using GTMDs*, 42nd International Conference on High Energy Physics, 17-24.07.2024, Prague, Czech Republic;
- B. Linek, M. Łuszczak, W. Schäfer, A. Szczurek, *GTMD approach in the production of diffractive dijets in DIS*, Polish Particle and Nuclear Theory Summit 2024, 11-13.09.2024, Cracow, Poland.

Scientific internships and study tours

- Department of Astronomy and Theoretical Physics at Lund University, Scientific consultation on angular correlations in heavy meson production, 10-23.06.2022, Lund, Szwecja, Departure supervisor: Roman Pasechnik,
  Financed by: *NAWA PROM-Międzynarodowa wymaina stypendialna doktorantów i kadry akademickiej*, contract number: 31/NAWA-PROM-UR/2019
- Department of Physics at the Faculty of Materials Science and Physics of the Cracow University of Technology, Scientific consultation on the production of heavy quarks, 8-22.12.2022, Cracow, Poland, Departure supervisor: dr hab. Agnieszka Łuszczak, prof. PK;
- Institute of Nuclear Physics Polish Academy of Sciences, Scientific consultation, 14-28.02.2023, Cracow, Poland, Departure supervisor: dr hab. Wolfgang Schäfter, prof. IFJ PAN;
- European Organization for Nuclear Research, Job Shadowing Internship, 7-18.12.2023, Meyrin, Switzerland, Departure supervisor: Bernhard Holzer,
  Financed by: *Granty dla młodych naukowców Uniwersytetu Rzeszowskiego*, decision number: NIG/23/2023;

Other activities

- Organization of the XVII Rzeszowska Konferencja Młodych Fizyków, 6-7.06.2023, Rzeszow, Poland.

Contents

List of Figures

List of Tables

Chapter 1

Introduction

In the 19th century, physics seemed to be fully understood, but observations from the 20th century made this field again turn out to be a great mystery to mankind. The particles that make up our world also turned out to be different than previously thought. In 1912, Ernest Rutherford, by scattering $^4\mathrm{He}$ nuclei on $^{79}\mathrm{Au}$ atoms, demonstrated the validity of the new atomic model assuming the existence of a positively charged nucleus and electrons orbiting around it. In 1935, Hideki Yukawa presented the first model of the interactions between the particles that make up an atomic nucleus, and in 1961 the Nobel Prize went to Robert Hofstadter for measuring the proton form factors. In 1967-1969, experiments on the scattering of leptons on nuclei began and have continued to this day. In 1990 Friedman, Kendall, and Taylor obtained the Nobel Prize for Deep Inelastic Scattering.

1.1 Collisions of elementary particles

The academic example of elementary particle collisions is electron-proton scattering, which results in the exchange of intermediate photons as shown in Fig.1.1. The exchanged particle is virtual. Its virtuality is given for the electron-proton collision by the formula (see Ref. [9]):

$$Q^2 \equiv -q^2 = -(k_e - k_{e'})^2 > 0. \tag{1.1}$$

Another aspect is whether or not the target is destroyed. In the first case, one speaks of elastic collisions, while in the second case of inelastic ones. The latter results in a proton remnant having a mass M_X. Feynman diagrams for this kind of situation are shown in Fig. 1.1. The figure also shows the energy of the γp system W^2 that equals in this case

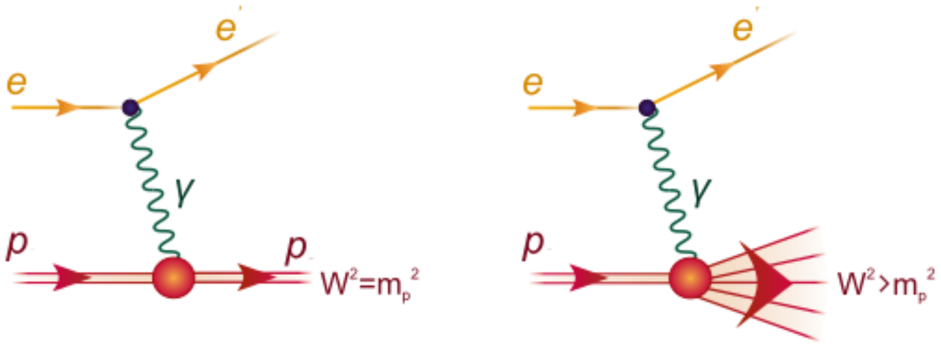

Figure 1.1: Electron-proton scatterings: elastic on the left, and inelastic on the right.

the invariant mass, which is mathematically represented as:

$$W^2 \equiv (P+q)^2 = M_X^2 \geq m_p^2 \simeq 1\,\mathrm{GeV}^2. \tag{1.2}$$

Relationship $Q^2 \gg m_p^2$, $W^2 \gg m_p^2$ is the criterion for the occurrence of so-called Deep Inelastic Scattering (DIS). The most important parameter, apart from the parton virtuality in DIS, is the Bjorken variable x_{Bj} (see [9])

$$x_{Bj} = \frac{Q^2}{2P\cdot q} = \frac{Q^2}{2m_pE_\gamma} \geq 0, \tag{1.3}$$

and the inelasticity y

$$y = \frac{P\cdot q}{P\cdot k_e} = \frac{E_\gamma}{E_e} = 1 - \frac{E_e^{'}}{E_e}. \tag{1.4}$$

Both of these variables are the Lorentz invariants and satisfy the condition $0 \leq x_{Bj},\, y \leq 1$ which can be seen from

$$(P+q)^2 \geq m_p^2 \implies (q^2+2P\cdot q) \geq 0 \implies \frac{-q^2}{2P\cdot q} \leq 1. \tag{1.5}$$

Moreover, for $S=(P+k_e)^2 \gg m_p^2$, it is true that

$$x_{Bj}yS = Q^2. \tag{1.6}$$

An alternative method of describing DIS is to use the scattering angle $\theta_e^{'}$ (as shown in Fig. 1.2) and the energy of the scattered electron $E_e^{'}$. In this approach, photon virtuality and x_{Bj} are expressed in terms of energy and scattering angle of the electron in the laboratory frame as:

$$Q^2 = 2E_eE_e^{'}(1-\cos\theta_e^{'}), \quad x_{Bj} = \frac{E_e^{'}}{E_p}\left[\frac{1-\cos\theta_e^{'}}{2-(E_e^{'}/E_e)(1+\cos\theta_e^{'})}\right], \tag{1.7}$$

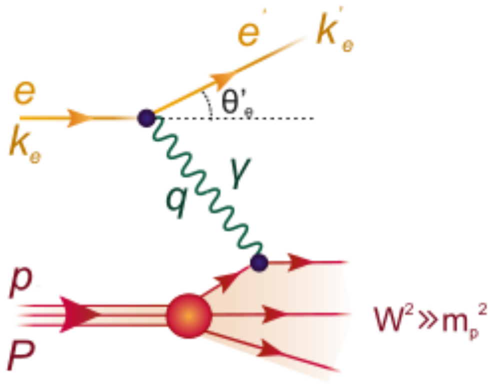

Figure 1.2: Deep inelastic electron-proton scattering.

from which it is clear that for $\theta_e^{'} \to 0$, $Q^2 \to 0$ and $x_{Bj} \to 0$. These relationships are the criteria for photoproduction and small-x limit, respectively.

The quantity describing the collisions is the scattering amplitude, expressed in terms of hadronic and leptonic currents given by the electro-weak current:

$$A(\ell N \to \ell^{'} X) = \bar{u}_{\ell'}(k^{'}, \lambda)\Gamma^\mu u_\ell(k, \lambda)\, \frac{i g_{\mu\nu}}{Q^2 + m_B^2} \langle X | J^\nu(0) | P, s\rangle, \tag{1.8}$$

for the photon exchange:

$$\Gamma^\mu = e\gamma^\mu, \quad m_B = 0, \tag{1.9}$$

and the particle polarizations are denoted as λ and s. For the unpolarized DIS with γ exchange, the cross-section for $\ell N \to \ell^{'} X$ equals:

$$\frac{d\sigma}{dE_e^{'} d\Omega_e^{'}} \sim \frac{1}{(Q^2)^2} L^{\mu\nu}(k, k^{'}) W_{\mu\nu}(q, P), \tag{1.10}$$

with the leptonic tensor (for $m_l = 0$):

$$L^{\mu\nu}(k, k^{'}) = \left[k^\mu k^{'\nu} + k^\mu k^{'\nu} - g^{\mu\nu}(k \cdot k^{'})\right], \tag{1.11}$$

and the hadronic tensor:

$$W_{\mu\nu}(q, P) = \sum_s \int d^4x e^{iq\cdot x} \langle P, s | J_\mu(x) J_\nu(0) | P, s\rangle. \tag{1.12}$$

In addition, using parity conservation, the most general form of the hadronic tensor is:

$$W_{\mu\nu} = -\left(g_{\mu\nu} + \frac{q_\mu q_\nu}{Q^2}\right) F_1 + \frac{1}{P\cdot q}\left(p_\mu + q_\mu \frac{P\cdot q}{Q^2}\right)\left(p_\nu + q_\nu \frac{P\cdot q}{Q^2}\right) F_2. \tag{1.13}$$

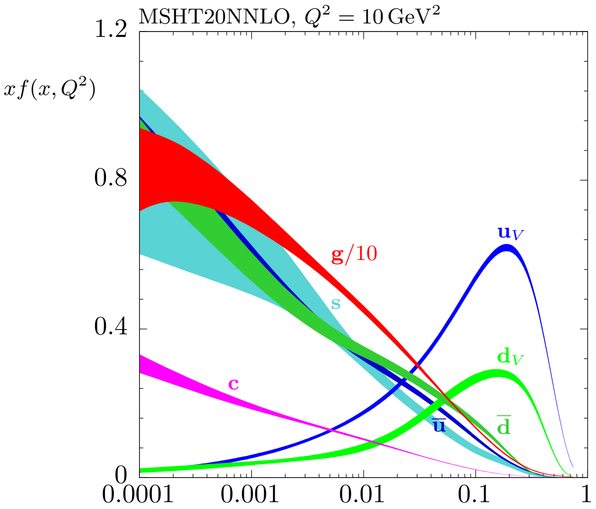

Figure 1.3: MSHT20 NNLO Parton distribution functions (PDFs) at $Q^2 = 10\,\mathrm{GeV}^2$ with associated 68% confidence level uncertainty bands (see Ref. [10]).

Due to the conservation of the electromagnetic current, it is true, that $q^\mu W_{\mu\nu} = 0$ (gauge invariance).

One may get the impression that Fig. 1.1 depicts particles as point objects but the pointlike elements that make up a proton are called partons and carry a fraction ξ of its momentum, which in the simplest case is equal to the Bjorken-x variable:

$$(\xi P + q)^2 = 0 \implies \xi = \frac{Q^2}{2P \cdot q} = x_{Bj} = \frac{Q^2}{Q^2 + W^2 - m_p^2}. \tag{1.14}$$

It is possible to introduce number distributions of a parton carrying fraction x of the proton's momentum, called the Parton Distribution Function (PDFs), an example of which is shown in Fig. 1.3.

These distributions reproduce the schematic particles seen in the earlier diagrams. They illustrate the presence of free quarks (valence, sea quarks) but also gluons, which includes the effects of quantum chromodynamics occurring in the proton. The proton structure function not including any corrections (the case represented schematically in the left diagram from the Fig. 1.5) is expanded by:

$$F_2(x) = \int_0^1 d\xi \sum_f \left[e_f^2\, \xi \delta(\xi - x) \right] q_f(\xi) = \sum_f e_f^2 x \{ q_f(x) + \bar{q}_f(x) \}, \tag{1.15}$$

where e_f is the charge of the quarks.

The interaction in the initial and final states occurs at large space-time distances (of the order of the proton mass inverse), which is much larger than the quark-time interaction.

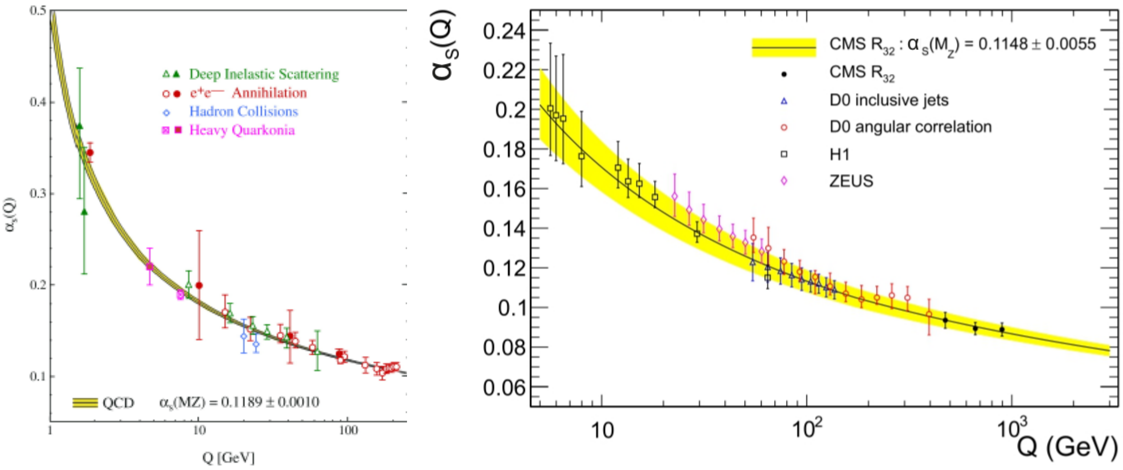

Figure 1.4: The measurements of the Q^2 dependence of the strong coupling $\alpha_s(Q)$ including small scale region from the Ref. [11] (left), and first $\mathcal{O}(\mathrm{TeV})$ range determination from the CMS experiment from the Ref. [12] (right).

Due to that fact, the quark distributions cannot come from the perturbation theory and carry information on the nonperturbative structure of the proton. As will be presented letter after QCD corrections they acquire a scale-dependencies (Q^2 dependence), which is calculable in perturbation theory. Considering all the above aspects, it should be stated that PDFs contain a rather limited amount of information.

1.2 Structure of the proton

The structure of the proton is more complicated than it might seem so far. This is because the quarks observed in it behave like free particles, even though it is not possible to observe individual quarks outside such structures because of the confinement property of the strong interaction. The fact that quarks probed at short distances behave as free particles is related to the phenomenon of asymptotic freedom. These interactions are proportional to the running coupling constant, whose experimental measurements for HERA and ALICE kinematics are shown in Fig. 1.4. For large Q^2 this coupling is expressed as:

$$\alpha_s(Q^2) = \frac{g_s^2}{4\pi} = \frac{12\pi}{(33 - 2n_f)\ln(Q^2/\Lambda_{QCD}^2)} \to 0, \tag{1.16}$$

where $\Lambda_{QCD} \simeq 200 - 400\,\mathrm{MeV}$.

According to this phenomenon, the strong interaction depends on the distance on which the quarks are resolved. Therefore, considering these chromodynamic (QCD) phe-

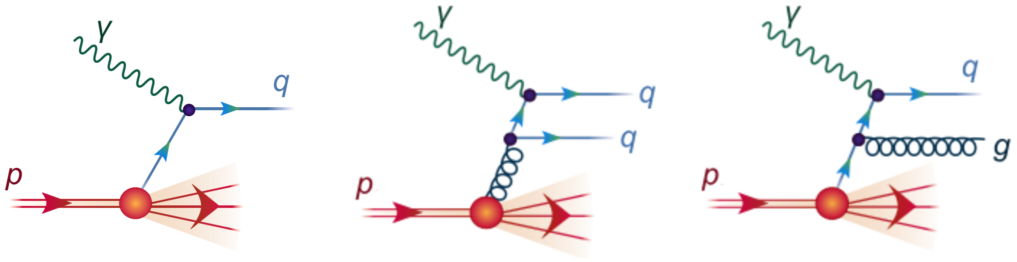

Figure 1.5: Quark productions in photon-proton scattering.

nomena, the distributions of partons depend on the scale as well. For this situation, the structure-function $F_2(x,Q^2)$ is expressed in the collinear factorization approach (in which $F_L = 0$ at the leading order) as:

$$\begin{aligned} F_2(x,Q^2) &= \int_0^1 d\xi \sum_{f,\bar{f}} \Big[e_f^2 \xi \delta(\xi - x) + \alpha_s(Q^2) C_q(\xi, x) + \cdots \Big] q_f(\xi, Q^2) \\ &+ \int_0^1 d\xi \Big[\alpha_s(Q^2) C_G(\xi, x) + \cdots \Big] G(\xi, Q^2) + \mathcal{O}\left(\frac{\Lambda^2}{\mathrm{Q}^2}\right), \end{aligned} \tag{1.17}$$

including the coefficient functions $C_q(\xi,x)$ and $C_G(\xi,x)$ correlated with appropriate process corrections (see Fig. 1.5) which are multiplied by the universal PDFs. The omitted terms $\mathcal{O}(\Lambda^2/Q^2)$ are referred to as higher twists.

From the optical theorem, it is known that the total γp cross-section is proportional to the imaginary part of the forward scattering amplitude (a sum over transverse and longitudinal photons is implied):

$$F_2 = \frac{Q^2}{4\pi\alpha_{em}} \sigma_{\gamma^* p} = \mathrm{Im}\,\mathrm{A}(\gamma^*\mathrm{p} \to \gamma^*\mathrm{p}). \tag{1.18}$$

Taking into account the above corrections, the photon-proton exchange reaction should be treated not only as the emission of a quark reacting with a photon but also as the emission of a series of n gluons, according to Fig. 1.6, and including the sum of all these interactions:

$$F_2(x,Q^2) = \sum_{n=0}^{\infty} a_n(x) \frac{\alpha_s^n}{n!} \left(\ln \frac{Q^2}{m^2} \right)^n, \tag{1.19}$$

with

$$\frac{\alpha_s^n}{n!} \left(\ln \frac{Q^2}{m^2} \right)^n = \alpha_s \int_{m^2}^{Q^2} \frac{dk_{\perp n}^2}{k_{\perp n}^2} \cdots \int_{m^2}^{k_{\perp 3}^2} \frac{dk_{\perp 2}^2}{k_{\perp 2}^2} \int_{m^2}^{k_{\perp 2}^2} \frac{dk_{\perp 1}^2}{k_{\perp 1}^2}, \tag{1.20}$$

and strongly ordered decreasing transverse momenta $k_{\perp n}$:

$$m^2 \ll k_{\perp 1}^2 \ll k_{\perp 2}^2 \ll \cdots \ll k_{\perp l}^2 \ll Q^2. \tag{1.21}$$

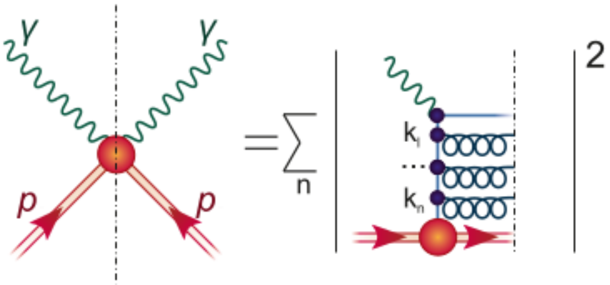

Figure 1.6: Formation of a series of gluons in the photon-proton reaction.

1.2.1 DGLAP evolution equation

As the above discussion shows the PDFs depend on the factorization scale μ_F, and are described by the integro-differential Dokshitzer-Gibrov-Lipatov-Alterelli-Parisi (DGLAP) evolution equations at the leading-order (see Refs [13, 14, 15]):

$$\begin{aligned}\frac{\partial f_q(x,\mu_F^2)}{\partial \mu_F^2} &= \frac{\alpha_s(\mu_F^2)}{2\pi}\int_x^1 \frac{dz}{z}\Big[P_{qq}\Big(\frac{x}{z}\Big)f_q(z,\mu_F^2)+P_{qg}\Big(\frac{x}{z}\Big)f_g(z,\mu_F^2)\Big],\\ \frac{\partial f_g(x,\mu_F^2)}{\partial \mu_F^2} &= \frac{\alpha_s(\mu_F^2)}{2\pi}\int_x^1 \frac{dz}{z}\Big[\sum_q P_{gq}\Big(\frac{x}{z}\Big)f_q(z,\mu_F^2)+P_{gg}\Big(\frac{x}{z}\Big)f_g(z,\mu_F^2\Big].\end{aligned} \tag{1.22}$$

In the above equation, $f_g(x,\mu_f^2)$ is the gluon density, while $f_q(x,\mu_F^2)$ corresponds to the quark and antiquark distributions of a given flavor in the proton. There are also so-called splitting functions that describe the probability of finding gluon/quark with momentum fraction x, that is emitted from an appropriate quark/gluon with momentum fraction z in the interval $\mu_F^2 \to \mu_F^2 + d\ln(\mu_F^2)$:

$$\begin{aligned}P_{qq}(z) &= C_F\left(\frac{1+z^2}{(1-z)_+}+\frac{3}{2}\delta(1-z)\right),\\ P_{qg}(z) &= T_F\Big(z^2+(1-z)^2\Big),\\ P_{gq}(z) &= C_F\frac{1+(1-z)^2}{z},\\ P_{gg}(z) &= 2C_A\Big(\frac{1-z}{z}+\frac{z}{(1-z)_+}+z(1-z)\Big)\\ &+ \Big(\frac{11}{6}C_A-\frac{2}{3}T_F n_F\Big)\delta(1-z),\end{aligned} \tag{1.23}$$

where $C_F = 4/3$, $T_F = 1/2$, $C_A = 2$, n_F is the number of quark flavors, and $(1-z)_+$ means, that for $x = 1$:

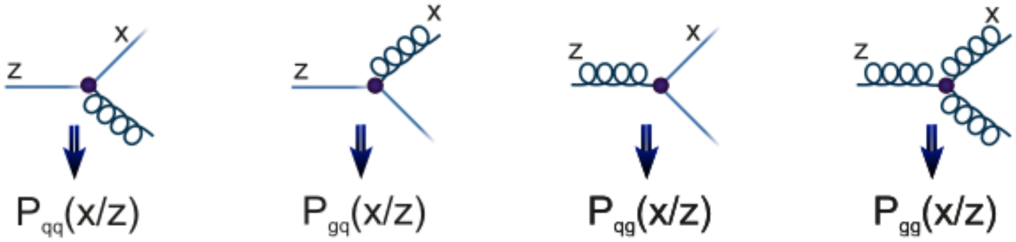

Figure 1.7: Different splitting function of photon-proton interactions.

$$\int_0^1 \frac{dz f(z)}{(1-z)_+} = \int_0^1 dz \frac{f(z)-f(1)}{1-z} = \int_0^1 dz \ln(1-z)\frac{d}{dz}f(z). \tag{1.24}$$

That function can be derived perturbatively as a power series of α_s. Moreover, all of them except P_{qg} are singular for $z \to 0$ or $z \to 1$, which corresponds to the dominance of soft and collinear gluon emissions. Therefore, in the calculation of the cross-section, they are absorbed into the PDFs definition.

1.2.2 Transverse factorization approach

It is possible to reduce the unintegrated parton distribution functions (UPDF) to the two-dimensional collinear PDFs $f_i(x, \mu_F^2)$ if the dependence of $k_\perp$ is integrated out:

$$f_i(x, \mu_F^2) \simeq \int_0^{\mu_F^2} dk_\perp^2 \mathcal{F}_i(x, k_\perp^2, \mu_F^2). \tag{1.25}$$

There are however subtleties to this relation regularization e.g. the presence of a Sudakov form factor which are omitted in this schematic discussion.

A certain limitation of this approach is that only to some extent of the UPDFs obey the relevant pQCD evolution equations. In particular, in the non-perturbative (small $k_\perp$) range, parton densities are described only by parameterizations and phenomenological models. It should be mentioned that in high-energy cases, quark-induced mechanisms can sometimes be neglected (as in the cases considered in this thesis). In such a situation, only non-integrated gluon densities are considered, but slightly differently defined unintegrated gluon distribution functions are also available in the literature. Caution is necessary in such situations, as they differ in the following transformation:

$$\mathcal{F}_g(x, k_\perp^2, \mu^2) \equiv \frac{1}{k_\perp^2} f_g(x, k_\perp^2, \mu^2). \tag{1.26}$$

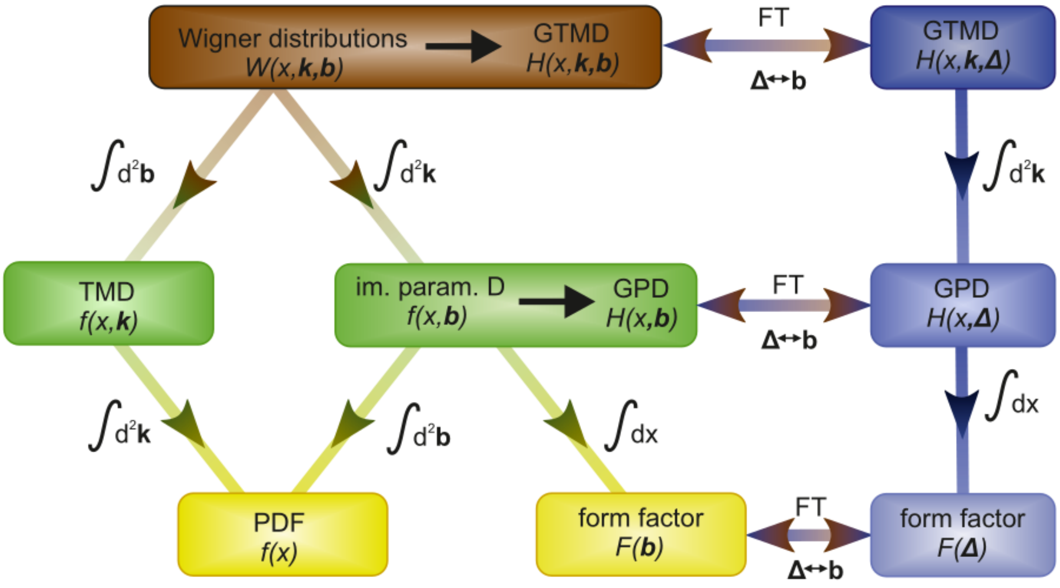

Figure 1.8: Different approaches used to describe the structure of the protons.

This approach provides an alternative to the standard collinear approach by being useful for studying many high-energy processes such as photoproduction [16, 17], hadroproduction [18, 19], description of DIS functions [19, 20, 21, 22] and DIS processes [23, 24].

1.2.3 Wigner distributions

The structure functions discussed so far used in the $k_\perp$ factorization provide a tree-dimensional description of the interior of the proton. There are also approaches that map the proton's structure in three or even five dimensions. These distribution functions are used e.g. in the dipole approach, and can be used to describe diffraction mechanisms of particle production. These are approaches derived from Wigner distributions, which transform into each other after applying appropriate integration and Fourier transforms. There are Wigner distribution functions $W(x, \vec{k}_\perp, \vec{b}_\perp)$, Transverse Momentum Dependence Distributions (TMDs), and Generalized Parton Distributions (GPDs). The TMDs take into account only the dependence on transverse momenta, while GPDs reflect the dipole size dependence. The relation between these approaches is illustrated in Fig. 1.8.

It is assumed that if the structure of the colliding particles is correctly described, the final state of the collision and the behavior of both the resulting particles and those that took part in it from the beginning will be well described. This conclusion implies the need to build particle colliders that make it possible to relate theoretical predictions to experimental data which can be measured using various detectors.

However, both the experimental conditions and the available technology used in the detectors contribute to limiting the possibility of reproducing the desired kinematics, hence various colliders are created with different parameters that are imposed primarily on the initial and final states of the collision, and the different luminosities of the collided particle beams are also taken into account. Currently, the largest facility of this type is the Large Hadron Collider (LHC) at the European Organization for Nuclear Research (CERN), very interesting results were also provided by the now defunct Hadron-Electron Ring Accelerator (HERA), where mainly the electron-proton (electron-nucleus) and positron-proton collisions were studied. Moreover, the Electron-Ion Collider (EIC) will be built soon, which will enable the study of electron-proton and electron-nucleus collisions, taking into account the much greater luminosity of the particles but also enabling spin polarization of the beams. There is also The High Energy Accelerator Research Organization (KEK) in Japan, the defunct SLAC (Stanford Linear Accelerator Center) National Accelerator Laboratory in the USA, and smaller ones.

The phase space of individual accelerators is shown in Fig. 1.9. This figure shows primarily the differences in collision energies in individual accelerators, the largest of which is characterized by Future Circular Collider FCC and the smallest by EIC. Moreover, only EIC will allow the study of the photon virtuality region smaller than $1\,\mathrm{GeV}$ at the area of x described so far. The planned expansion of the LHC to FCC-eh (electron-hadron Future Circular Collider) or LHeC (Large Hadron-electron Collider) may allow for deeper knowledge about the area of smaller x (if they are built), which will significantly improve the possibilities of expanding knowledge about the properties of elementary particles.

Individual approaches to describing the structure of hadrons and various mechanisms of lepton and quark production for appropriate kinematic areas are presented in the further chapters of this thesis.

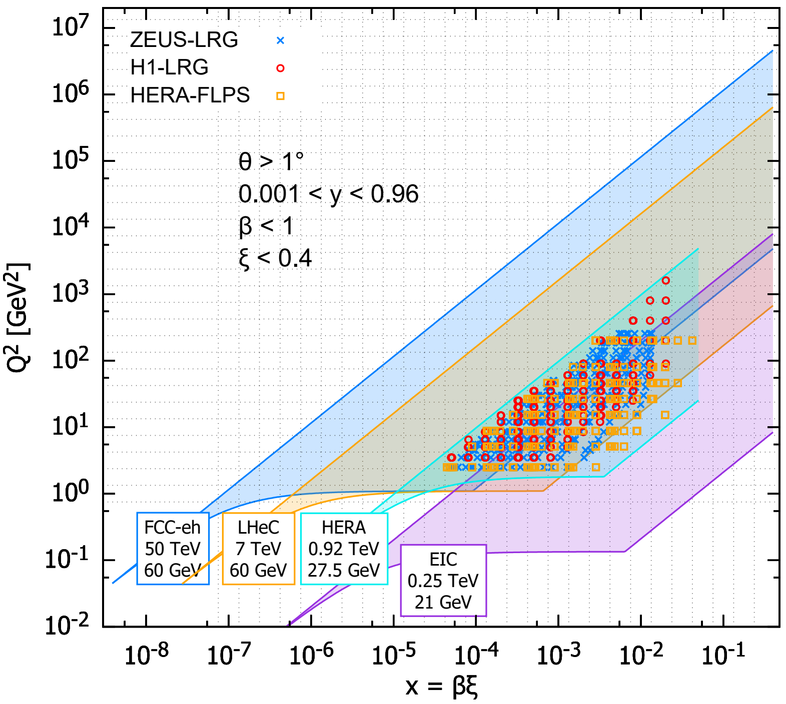

Figure 1.9: Phase space of HERA and future colliders (see Ref. [25]).

Chapter 2

Charged lepton pair production in two-photon exchange

The processes of producing pairs of charged leptons initiated by photon exchange are divided into two parts. First, there is the emission of photons and the production of lepton pair by photon-photon fusion, and second possible additional interactions between protons or their remnants occur, as shown in Fig. 2.1 (see for example Ref. [26]). These processes can be distinguished by examining the final state of the collision but in practice during the experiment, this is accomplished by measuring protons in the forward proton detectors installed at the ATLAS [27, 28, 29, 30] and ALICE [31, 32, 33] collaborations.

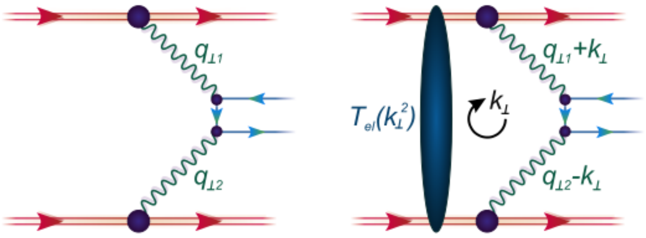

Figure 2.1: Amplitudes for production of the photon-induced lepton pair: bare one on the left, and screened on the right [26].

The theoretical analysis of these processes is considered in the literature using two different approaches. The first one treats photons as collinear partons of a proton and requires taking into account a hard scale, e.g. by large photon virtualities or large transverse momenta of leptons [34, 35, 36, 37, 38]. In the second one, used in further analyses, the

$\gamma^* p \to X$ vertices are parameterized according to the proton structure functions. It is then assumed that photons are collinear or have transverse momenta and non-zero virtuality [39, 40]. This approach called the transverse factorization or $k_\perp$-factorization approach, which was already generally mentioned, was initially used to analyze gluon exchange processes. It uses unintegrated photon distributions in the proton and off-shell matrix elements for $\gamma\gamma \to l^+ l^-$ sub-processes.

The UPDs of the protons are expressed by proton structure functions, which have been quite well studied experimentally, particularly in the perturbation region used in the DGLAP evolution equation. Outside this area, these functions are much less known and described using various parameterizations e.g. from Refs. [41, 42, 43, 44, 45] therefore the possibility of their use is limited in various ways and not very well tested in all kinematic domains.

Taking into account photons as partons in the proton makes it possible to write its distribution $\gamma(z, Q^2)$ as carrying the z part of the proton's light cone momentum according to the DGLAP equation [34, 35]:

$$\begin{aligned} \frac{d\gamma(z,Q^2)}{d\ln Q^2} &= \frac{\alpha_{em}}{2\pi}\int_x^1 \frac{dy}{y}\Bigg\{\sum_f e_f^2 P_{\gamma\leftarrow q}(y) \\ &\times \left[q_f\Big(\frac{z}{y},Q^2\Big)+\bar{q}_f\Big(\frac{z}{y},Q^2\Big)\right]+P_{\gamma\leftarrow\gamma}(y)\gamma\Big(\frac{z}{y},Q^2\Big)\Bigg\}, \end{aligned} \tag{2.1}$$

with splitting functions $P_{\gamma\leftarrow q}(y) = \frac{1+(1-y)^2}{y}$, $P_{\gamma\leftarrow\gamma} = -\frac{2}{3}\sum_f e_f^2 \delta(1-y)$, and then include them along with gluons and quarks distributions in the complete set DGLAP equations:

$$\begin{aligned} \frac{dq_f(z,Q^2)}{d\ln Q^2} &= \frac{dq_f(z,Q^2)}{d\ln Q^2}\bigg|_{\text{QCD}} + \frac{\alpha_{em}}{2\pi}\int_x^1 \frac{dy}{y}\delta P^{\text{QED}}_{q\leftarrow q}(y) q_f\Big(\frac{z}{y},Q^2\Big) \\ &+ \frac{\alpha_{em}}{2\pi}\int_x^1 \frac{dy}{y} P_{\gamma\leftarrow q}(y)\gamma\Big(\frac{z}{y},Q^2\Big). \end{aligned} \tag{2.2}$$

The small value of the α_{em} parameter makes the impact of photons on the density of quarks and antiquarks negligible, which is the case in the approach of Glück et al. [34]. If the area of interest is higher-order perturbative corrections to the QCD splitting functions, an approach that includes the photon density like the Durham [35, 36] and NNPDF [37] groups approach is used.

According to the Glück et al. approach, with sufficiently large virtuality Q_0^2, the photon parton density can be calculated based on the collinear splitting of quarks ($q \to q\gamma$) and antiquarks ($\bar{q} \to \bar{q}\gamma$):

$$\frac{d\gamma(z,Q^2)}{d\ln Q^2} = \frac{\alpha_{em}}{2\pi}\sum_f e_f^2 \int_z^1 \frac{dx}{x} P_{\gamma\leftarrow q}\Big(\frac{z}{x}\Big)\Big\{q_f(x,Q^2) + \bar{q}_f(x,Q^2)\Big\}, \tag{2.3}$$

which gives the photon density equation

$$\begin{aligned}\gamma(z,Q^2) &= \sum_f \frac{\alpha_{em} e_f^2}{2\pi}\int_{Q_0^2}^{Q^2}\frac{d\mu^2}{\mu^2}\int_z^1 \frac{dx}{x}P_{\gamma\leftarrow q}\Big(\frac{z}{x}\Big) \\ &\times \Big\{q_f(x,\mu^2) + \bar{q}_f(x,\mu^2)\Big\} + \gamma(z,Q_0^2) \\ &= \frac{\alpha_{em}}{2\pi}\int_{Q_0^2}^{Q^2}\frac{d\mu^2}{\mu^2}\int_z^1\frac{dx}{x}P_{\gamma\leftarrow q}\Big(\frac{z}{x}\Big)\frac{F_2(x,\mu^2)}{x} + \gamma(z,Q_0^2). \end{aligned} \tag{2.4}$$

This approach takes into account the Weizsäcker-Williams flux from coherent emission $p \to p\gamma^*$ without proton decay according to [40]. However, the photon density at low scale $\gamma(z,Q_0^2) = 0$ leaves the possibility to dominates at very large $Q^2 \gg Q_0^2 \sim 1\mathrm{GeV}^2$, the part predicted perturbatively from quark and antiquark distributions.

Approaches from Refs [35, 36, 37] also require the assumption of photon density at the initial scale $\gamma(z,Q_0^2)$, which is modeled in this case as:

$$\begin{aligned}\gamma(z,Q_0^2) &= \frac{\alpha_{em}}{2\pi}\int_z^1\frac{dy}{y}\left\{\frac{4}{9}\ln\Big(\frac{Q_0^2}{m_u^2}\Big)u\Big(\frac{z}{y},Q_0^2\Big) + \frac{1}{9}\ln\Big(\frac{Q_0^2}{m_d^2}\Big)d\Big(\frac{z}{y},Q_0^2\Big)\right\} \\ &\times \frac{1+(1-y)^2}{y}. \end{aligned} \tag{2.5}$$

Both proposals presented by Glück et al. and Duhram group do not include the contribution of the photon for the $2 \to 2$ processes, although the latter group, like NNPDF [37], presented a different approach in which the photon distribution is fully incorporated into the coupled DGLAP evolution equation. Of course, also in this case the photon parton density on the initial scale $\gamma(z,\,Q_0^2)$ needs to be determined, which the Duhram group modeled. At the same time, NNPDF decided to fit it into the experimental data.

Above $u(x,Q_0^2)$ and $d(x,Q_0^2)$ are valence-like distributions at the initial scale Q_0^2. However, important is the fact that the input distribution $\gamma(z,Q_0^2)$ contains only a coherent, i.e. elastic, contribution. The integral over virtualities converges quickly in such a situation, becoming independent of this parameter as soon as $Q_0^2 \gtrsim 0.7\,\mathrm{GeV}^2$.

In the next section, the approach that calculates photon parton distributions directly from the proton structure functions is discussed. This approach has been developed in Refs [39, 46] for light-energy kinematics, analogous to $k_\perp$-factorization. A more general formalism built on the same idea can be found in Refs [47, 48].

2.1 Proton-proton collisions

Ones of the simplest processes of this type are proton collisions. Therefore, the next few subsections will be devoted to the production of muons (and therefore, due to small differences, also electrons) in proton-proton collisions. The kinematics of these processes, with a further discussion of the mechanisms of proton-proton exchange, will be presented in these collisions.

2.1.1 Kinematics

In the case of proton-proton collisions four situations can occur, as shown in Fig. 2.2. Both protons can be destroyed - in a double inelastic or inelastic-inelastic collision, only one of them can be destroyed - in elastic-inelastic or inelastic-elastic processes collectively called single disassociation, and both protons can survive in a fully elastic, or elastic-elastic, collisions.

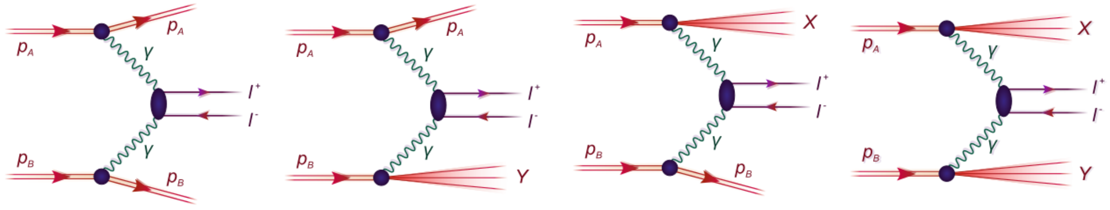

Figure 2.2: Different mechanisms of two-photon dilepton production in proton-proton collision.

For these ultrarelativistic collisions of protons A and B with four-momenta p_A and p_B which fulfill the off-shell conditions $p_A^2 = m_A^2$, $p_B^2 = m_B^2$ it is possible to introduce the following light-like momenta:

$$p_1 = p_A - \frac{m_A^2}{\tilde{s}} p_B, \quad p_2 = p_B - \frac{m_B^2}{\tilde{s}} p_A, \tag{2.6}$$

where

$$\tilde{s} = s \cdot \frac{1}{2}\left\{1 + \sqrt{1 - \frac{4m_A^2 m_B^2}{s^2}}\right\}, \quad s \equiv 2(p_A \cdot p_B), \tag{2.7}$$

therefore $p_1^2 = p_2^2 = 0$. As a result of high-energy kinematics, the following values of any colliding particles should be considered small:

$$\epsilon \sim \frac{m_{1,2}^2}{s}, \quad \frac{\vec{p}_{\perp\,1,2}^{\,2}}{s}, \quad \frac{m_{1,2}|\vec{p}_{\perp\,1,2}|}{s}, \tag{2.8}$$

and in particular

$$s = E_{cm}^2(1 + \mathcal{O}(\epsilon)), \quad 2(\mathrm{p}_1 \cdot \mathrm{p}_2) = \mathrm{s}(1 + \mathcal{O}(\epsilon)). \tag{2.9}$$

This work assumes exact calculations in terms of power-law consistency for a small parameter ϵ, hence no further distinction is made between quantities differing by the value $\mathcal{O}(\epsilon)$, wherever possible. Moreover, introducing the Sudakov distribution for the arbitrary four-vector a:

$$a = \alpha p_1 + \beta p_2 + a_\perp, \tag{2.10}$$

and the Gribov-decomposition of the metric tensor

$$g_{\mu\nu} = g_{\mu\nu}^\perp + \frac{p_{1\mu}p_{2\nu} + p_{2\mu}p_{1\nu}}{(p_1 \cdot p_2)}. \tag{2.11}$$

The euclidean components of the transverse part of the four-vector $a_\mu^\perp \equiv g_{\mu\nu}^\perp a_\nu$ are denoted by $\vec{a}_\perp$ so that

$$(a^\perp \cdot b^\perp) = -\vec{a}_\perp \cdot \vec{b}_\perp. \tag{2.12}$$

2.1.2 Amplitude of the dilepton production

Denoting the momentum of the produced leptons as p_+ and p_-, one can express the amplitude of their production closely to the study in [49] as:

$$M = -i\frac{(4\pi\alpha_{em})^2}{q_1^2 q_2^2} V_\mu^{A\to X}(p_A, p_X) g_{\mu\alpha} \bar{u}_\lambda(p_-) T_{\alpha\beta} v_{\bar{\lambda}}(p_+) g_{\beta\nu} V_\nu^{B\to Y}(p_B, p_Y), \tag{2.13}$$

with

$$T_{\alpha\beta} = \gamma_\alpha \frac{\hat{q}_1 - \hat{p_+} + m}{(q_1 - p_+)^2 - m^2}\gamma_\beta + \gamma_\beta \frac{\hat{q}_2 - \hat{p}_+ + m}{(q_2 - p_+)^2 - m^2}\gamma_\alpha, \quad \hat{q}_1 \equiv q_{1\mu}\gamma_\mu, \quad \text{etc.} \tag{2.14}$$

and

$$\sqrt{4\pi\alpha_{em}} V_\mu^{A\to X}(p_A, p_X) = \langle X(p_X)|j_\mu^{em}(0)|A(p_A)\rangle, \tag{2.15}$$

which square is related to the hadronic tensor:

$$W_{\mu\nu}^A(q) \equiv \sum_X (2\pi)^3 \delta^{(4)}(p_X - p_A - q) V_\mu^{\dagger A\to X}(p_A, p_X) V_\nu^{A\to X}(p_A, p_X). \tag{2.16}$$

Moreover, as follows from the Gribov metric tensor decomposition, the leading contribution to the upper energy limit can be obtained by substituting photon propagators [39]

$$g_{\mu\alpha} \to \frac{2}{s} p_{2\mu} p_{1\alpha}, \quad g_{\beta\nu} \to \frac{2}{s} p_{2\nu} p_{1\beta}. \tag{2.17}$$

As a result of the above transformations, a compact representation of the production amplitude can be obtained [50, 51]:

$$\mathcal{M} = -is \frac{(8\pi\alpha_{em})^2}{q_1^2 q_2^2} N_1(q_1) B_{\lambda\bar{\lambda}}(k_+, k_-; q_1, q_2) N_2(q_2), \tag{2.18}$$

with

$$N_1(q_1) = \frac{1}{s} p_{2\mu} V_\mu^{A\to X}(p_A, p_X), \quad N_2(q_2) = \frac{1}{s} p_{1\nu} V_\nu^{B\to Y}(p_B, p_Y), \tag{2.19}$$

and

$$B_{\lambda\bar{\lambda}}(k_+, k_-; q_1, q_2) \;=\; \frac{1}{s} p_{1\alpha} p_{2\beta} \bar{u}_\lambda(k_-) T_{\alpha\beta} v_{\bar{\lambda}}(k_+), \tag{2.20}$$

which is taken into account in the standard normalization as

$$d\sigma(AB \to X l^+ l^- Y) = \frac{1}{2s} \overline{|\mathcal{M}|^2} d\Phi(s; \{p_i\}_{i\in X}, \{p_j\}_{j\in Y}, k_+, k_-). \tag{2.21}$$

Here $d\Phi$ is the phase-space elements. Also, for the photon four vectors q_1 and q_2 the Sudakov decomposition is possible

$$q_1 = \alpha_1 p_1 + \beta_1 p_2 + q_{1\perp}, \quad q_2 = \alpha_2 p_1 + \beta_2 p_2 + q_{2\perp}, \quad q_i^2 = \alpha_i \beta_i s - \vec{q}_{\perp i}^{\,2}, \tag{2.22}$$

and

$$q_\pm = \alpha_\pm p_1 + \beta_\pm p_2 + q_{\pm\perp}, \tag{2.23}$$

in which the Sudakov parameters

$$\beta_1 = -\frac{M_X^2 - m_A^2 + \vec{q}_{\perp 1}^{\,2} + \alpha_1 m_A^2}{(1-\alpha_1)s}, \quad \alpha_2 = -\frac{M_Y^2 - m_B^2 + \vec{q}_{\perp 2}^{\,2} + \beta_2 m_B^2}{(1-\beta_2)s} \tag{2.24}$$

are determined based on the on-shell conditions $p_A^2 = m_A^2, \quad p_X^2 = M_X^2, \quad p_B^2 = m_B^2$, $p_Y^2 = M_Y^2$ which also implies $\alpha_2 \sim \beta_1 \sim \frac{q^2}{s}$ and $\alpha_1 \sim \beta_2 \sim \frac{m}{\sqrt{s}}$. Moreover, the virtualities of photons are expressed as follows:

$$\begin{aligned} Q_1^2 \;&\equiv\; -q_1^2 = \frac{1}{1-\alpha_1}\Big\{\vec{q}_{\perp 1}^{\,2} + \alpha_1(M_X^2 - m_A^2) + \alpha_1^2 m_A^2\Big\}, \\ Q_2^2 \;&\equiv\; -q_2^2 = \frac{1}{1-\beta_2}\Big\{\vec{q}_{\perp 2}^{\,2} + \beta_2(M_Y^2 - m_B^2) + \beta_2^2 m_B^2\Big\}. \end{aligned} \tag{2.25}$$

2.1.3 Off-shell cross-section

In the transverse factorization approach, the photon-photon contribution to inclusive cross-section for dilepton production can be written as:

$$\frac{d\sigma^{(i,j)}}{dy_+dy_-dp_{\perp+}dp_{\perp-}} = \sum_{i,j} x_1\gamma^{(i)}(x_1,\vec{q}_{\perp 1})x_2\gamma^{(j)}(x_2,\vec{q}_{\perp 2})\frac{d\sigma(p_+,p_-;\vec{q}_{\perp1},\vec{q}_{\perp2})}{dy_+dy_-d^2\vec{p}_{\perp+}d^2\vec{p}_{\perp-}} \tag{2.26}$$

where

$$x_1 = \frac{m_{\perp+}}{\sqrt{s}}e^{y_-} + \frac{m_{\perp-}}{\sqrt{s}}e^{y_-}, \qquad x_2 = \frac{m_{\perp+}}{\sqrt{s}}e^{-y_+} + \frac{m_{\perp-}}{\sqrt{s}}e^{-y_-},$$
$$m_{\perp\pm} = \sqrt{\vec{p}^{\,2}_{\perp\pm} + m_l^2} \tag{2.27}$$

and indices i and j denote $i, j = el, inel$ correspond to elastic or inelastic components of the colliding particles.

The last part of the above equation is the off-shell cross-section for the fusion of two virtual photons into leptons, written as

$$\begin{aligned}\frac{d\sigma^*(p_+,p_-;\vec{q}_{\perp1},\vec{q}_{\perp2})}{dy_1dy_2d^2\vec{p}_{\perp+}d^2\vec{p}_{\perp-}} &= \frac{\alpha^2_{em}}{\vec{q}^{\,2}_{\perp1}\vec{q}^{\,2}_{\perp2}}\sum_{\lambda,\bar\lambda}\Big|B_{\lambda\bar\lambda}(p_+,p_-;q_1,q_2)\Big|^2 \\ &\times\ \delta^{(2)}(\vec{q}_{\perp1}+\vec{q}_{\perp2}-\vec{p}_{\perp+}-\vec{p}_{\perp-}).\end{aligned} \tag{2.28}$$

Parameterizing the lepton four-momenta in terms of their Sudakov parameters $p_\pm = \alpha_\pm p_1 + \beta_\pm p_2 + p_{\perp\pm}$ and $\beta_\pm = (\vec{p}^{\,2}_{\perp\pm}+m^2)/(\alpha\pm s)$ allows to obtain a particularly simple form of the off-shell cross-section variables [49]:

$$z_\pm = \frac{\alpha_\pm}{\alpha}, \quad \vec{k}_\perp = z_-\vec{p}_{\perp+} - z_+\vec{p}_{\perp-}. \tag{2.29}$$

While the off-shell matrix element included photon 1 being in the longitudinal or transverse polarization states, the full matrix element squared including interference contribution is written as [39]:

$$\begin{aligned}\sum_{\lambda\bar\lambda}\Big|B_{\lambda\bar\lambda}(p_+,p_-;q_1,q_2)\Big|^2 &= \frac{1}{s^2}\sum_{\lambda\bar\lambda}\Big|p_{1\alpha}p_{2\beta}\bar{u}_\lambda(p_-)T_{\alpha\beta}v_{\bar\lambda}(p_+)\Big|^2 \\ =\ 2z_+z_-\vec{q}^{\,2}_{\perp1}&\Bigg\{\underbrace{4z_+^2z_-^2\vec{q}^{\,2}_{\perp1}\Phi_0^2}_{L} + \underbrace{(z_+^2+z_-^2)\vec{\Phi}^2_\perp + m_l^2\Phi_0^2}_{T} \\ +\ &\underbrace{\left\{\vec{\Phi}_\perp\times\frac{\vec{q}_{\perp1}}{|\vec{q}_\perp|}\right\}^2 - \left(\frac{\vec{\Phi}_\perp\cdot\vec{q}_{\perp1}}{|\vec{q}_{\perp1}|}\right)^2}_{TT'} + \underbrace{4z_+z_-(z_+-z_-)\Phi_0\Big(\vec{q}_{\perp1}\vec{\Phi}_\perp\Big)}_{LT}\Bigg\},\end{aligned} \tag{2.30}$$

with familiar structures which will also be discussed later

$$\begin{aligned}
\Phi_0 &= \frac{1}{(\vec{k}_\perp + z_+\vec{q}_{\perp 2})^2 + \varepsilon^2} - \frac{1}{(\vec{k}_\perp - z_-\vec{q}_{\perp 2})^2 + \varepsilon^2}, \\
\vec{\Phi}_\perp &= \frac{\vec{k}_\perp + z_+\vec{q}_{\perp 2}}{(\vec{k}_\perp + z_+\vec{q}_{\perp 2})^2 + \varepsilon^2} - \frac{\vec{k}_\perp - z_-\vec{q}_{\perp 2}}{(\vec{k}_\perp - z_-\vec{q}_{\perp 2})^2 + \varepsilon^2},
\end{aligned} \tag{2.31}$$

and $\varepsilon = m_l^2 + z_+ z_- Q_1^2$.

Taking into account the constraints resulting from the conservation of momentum and energy implies the occurrence of a condition on the masses of the generated dissociative systems for elastic-inelastic, inelastic elastic, and double inelastic contribution:

$$\begin{aligned}
W_{\gamma_1 p_2} &= \sqrt{s_{\gamma_1 p_2}} = \sqrt{x_1 s - \vec{q}_{\perp 1}^{\,2}} > M_Y + M_{ll} > M_Y, \\
W_{\gamma_2 p_1} &= \sqrt{s_{\gamma_2 p_1}} = \sqrt{x_2 s - \vec{q}_{\perp 2}^{\,2}} > M_X + M_{ll} > M_X,
\end{aligned} \tag{2.32}$$

with the invariant mass of the dilepton system given by

$$M_{ll}^2 = m_{\perp +}^2 + m_{\perp -}^2 + 2 m_{\perp +} m_{\perp -} \cosh(y_+ - y_-) - (\vec{p}_{\perp +} + \vec{p}_{\perp -})^2. \tag{2.33}$$

Moreover, due to the explicit use of the smallness of the Sudakov parameters given in Eq. (2.24) in the expansion of photon momentum for estimating off-shell matrix elements. Thus, to correctly approximate, for example, $q_1 = x_1 p_1 + q_{1\perp}$, to satisfy the condition

$$x_1 \gg \frac{M_X^2 - m_A^2 + \vec{q}_{\perp 1}^{\,2} + x_1 m_A^2}{(1 - x_1)s}, \quad \text{and} \quad x_2 \gg \frac{M_Y^2 - m_A^2 + \vec{q}_{\perp 2}^{\,2} + x_2 m_A^2}{(1 - x_2)s}, \tag{2.34}$$

which means, that one should not aim for too large invariant masses of the proton remnants, at a given center-of-mass energy. Photons coupled to the elastic transition represent a case in which the cutoff of the form factor at $\vec{q}_{\perp 1}^{\,2}$ and $\vec{q}_{\perp 2}^{\,2}$ is strong enough, to satisfy Eq. (2.34) very well in the energy range considered next.

2.1.4 Photon densities

Unintegrated photon densities $\mathcal{F}^{(i)}_{\gamma^*/A}$ may correspond to elastic collisions $(i = el)$ which correspond to the electric $G_E(Q^2)$ and magnetic $G_M(Q^2)$ Sachs form factors, that are expressed by the independent Dirac form factors $F_1(Q^2)$ and $F_2(Q^2)$ [52]:

$$\begin{aligned}
G_E(Q^2) &= F_1(Q^2) - \tau F_2(Q^2), \quad \tau = \frac{Q^2}{4m_p^2}, \\
G_M(Q^2) &= F_1(Q^2) + F_2(Q^2).
\end{aligned} \tag{2.35}$$

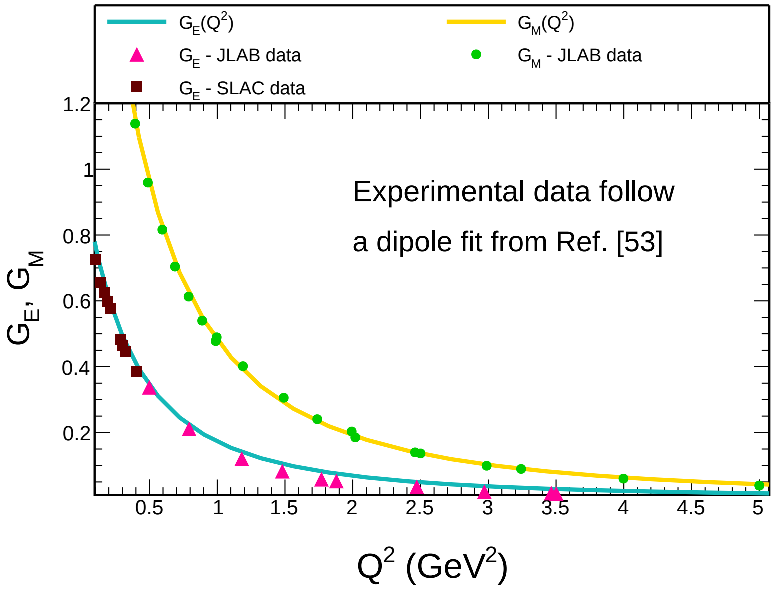

Figure 2.3: Q^2 dependence of the electromagnetic form factors of the proton. The upper figure corresponds to Eq. 2.36, while the bottoms are comparison with experiments from Ref. [53].

For the proton, it can also be written as in Ref. [39]:

$$\begin{aligned} G_E(Q^2) &= \frac{1}{(1-Q^2/0.71GeV^2)^2}, \\ G_M(Q^2) &= \mu G_E(Q^2), \end{aligned} \tag{2.36}$$

with the proton magnetic moment $\mu = 2.79$. The distributions of these form factors are visible in Fig. 2.3.

The Dirac form factors are also correlated with the electromagnetic current (for details see Ref. [52]:

$$\begin{aligned} \langle p', s'|j_\mu|p,s\rangle &= e\bar{u}(p',s')\Big(\gamma_\mu F_1(Q^2) + \frac{i}{2m}\sigma_{\mu\nu}q^\nu F_2(Q^2)\Big)u(p,s), \\ \sigma_{\mu\nu} &= \frac{i}{2}(\gamma_\mu\gamma_\nu - \gamma_\mu\gamma_\nu), \end{aligned} \tag{2.37}$$

where $e = \sqrt{4\pi\alpha_{em}}$ is the elementary charge. Furthermore, for the $Q^2 = 0$ the $F_1(0) = 1$ gives magnetic moment, while $F_2(0) = \mu_{an} = 1.792847351(28)$ gives "anomalous" magnetic moment.

The integrated photon densities may also correspond to the inelastic collisions $(i = inel)$ which depend on the proton structure function F_T and F_L [39, 46]:

$$\begin{aligned}
\mathcal{F}^{(el)}_{\gamma/A}(\alpha,\vec{q}_\perp^{\,2}) &= \frac{\alpha_{em}}{\pi}(1-\alpha)\left\{\frac{\vec{q}_\perp^{\,2}}{\vec{q}_\perp^{\,2}+\alpha^2 m_A^2}\right\}^2 \frac{4m_p^2 G_E^2(Q^2)+Q^2 G_M^2(Q^2)}{4m_p^2+Q^2} \\
&\times \left(1-\frac{Q^2-\vec{q}_\perp^{\,2}}{Q^2}\right), \qquad (2.38) \\
\mathcal{F}^{(inel)}_{\gamma/A}(\alpha,\vec{q}_\perp^{\,2}) &= \frac{\alpha_{em}}{\pi}(1-\alpha)\int_{M_{Thr}}^{\infty}\frac{dM_X^2 F_2(M_X^2,Q^2)}{M_X^2+Q^2-m_p} \\
&\times \left(1-\frac{Q^2-\vec{q}_\perp^{\,2}}{Q^2}\right)\left\{\frac{\vec{q}_\perp^{\,2}}{\vec{q}_\perp^{\,2}+\alpha(M_X^2-m_p^2)+\alpha^2 m_A^2}\right\}^2. \qquad (2.39)
\end{aligned}$$

Only the F_2 function is visible in the above equation, which is related to the approximation occurring with dependence:

$$\begin{aligned}
F_T(x_{Bj},Q^2) &= 2x_{Bj}F_1(x_{Bj},Q^2), \\
F_2(x_{Bj},Q^2) &= \frac{F_T(x_{Bj},Q^2)+F_L(x_{Bj},Q^2)}{1+4x_{Bj}^2 m_A^2/Q^2}, \qquad (2.40)
\end{aligned}$$

which in the high energy limit gives $F_2 \sim F_T + F_L$. The F_2 function, similar to photon parton distributions, is mapped by various models. Four of them are used in this analysis:

- the oldest one is the ALLM parametrization, created to describe experimental data from HERA by H. Abramowicz, E. M. Levin, A. Levy, U. Maor including only F_2 function that can be found in Ref. [41, 42];
- the FFJLM function that was originally used to describe JLab data with a fairly narrow range of Q^2 and W^2 by R. Fiore, A. Flachi, L. L. Jenkovszky, A. I. Lengyel and V. K. Magas also including only F_2 function, see Ref. [43];
- the LUX-like function which is based on the very popular LUX parametrization proposed by A. V. Manohar, P. Nason, G. P. Salam and G. Zanderighi that precisely describes a wide range of x_{Bj} and Q^2 using F_2 and F_L structure functions in Ref. [47];
- the KB parametrization that is one of the newest ones (created in 2021 by S. A. Kulagin and V. V. Barinov) and therefore is not fully confronted with experimental data. It also includes F_2 and F_L structure functions and is described in Ref. [54].

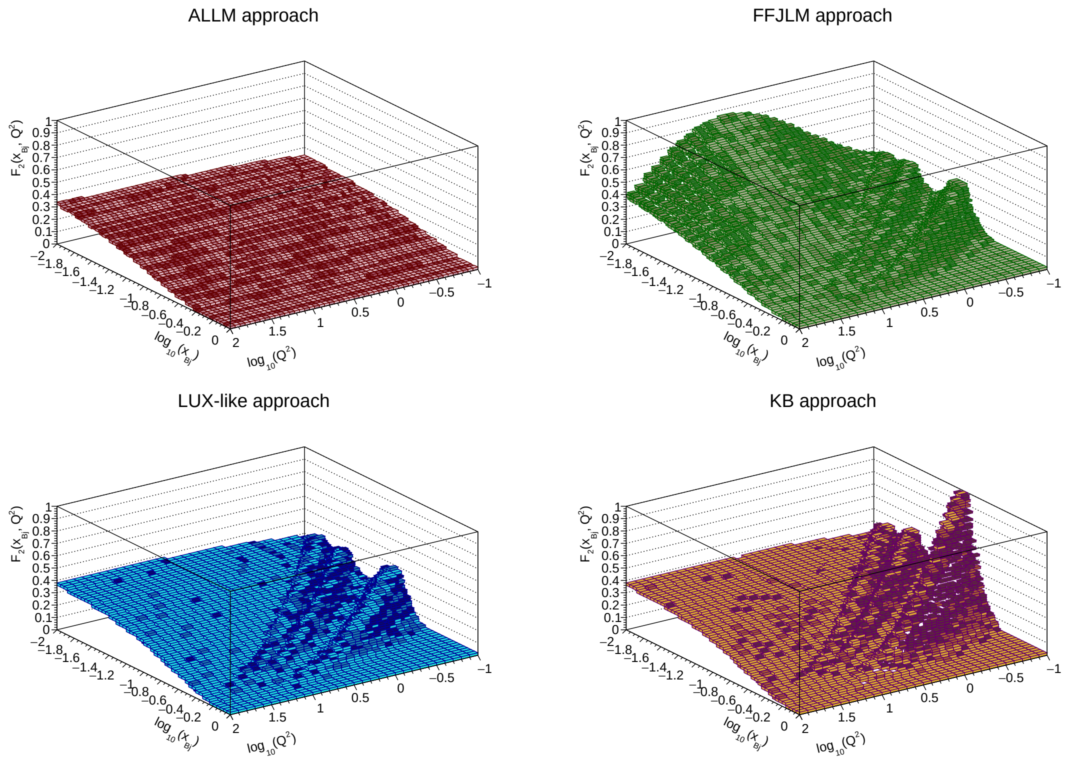
ALLM approach

FFJLM approach

LUX-like approach

KB approach

Figure 2.4: Different parametrizations of the structure functions depending on the $\log_{10}(x_{Bj})$ and $\log_{10}(Q^2)$.

The distributions of these functions in their most important kinematic variables are visible in Fig. 2.4, where we can notice the differences between them. Firstly, the ALLM parametrization does not contribute resonances seen in other cases, the most important of which are $\Delta(1232)$ and $N(1440)$. The value of FFJLM increases significantly in the small x-Bjorken and intermediate virtuality regions, although otherwise, its shape is quite similar to LUX-like, which also coincides with the KB model, but in this newest function, the resonance values are higher, especially one resonance at high x_{Bj} and low Q^2.

2.1.5 Low mass dilepton production in proton-proton collision with one forward proton measurement at the LHC

Until recently, no experimental study of lepton production by measuring forward protons had been conducted, so it was not possible to relate theoretical predictions to experimental data. However, the study of proton collisions by the CMS+TOTEM (Total Cross Section, Elastic Scattering and Diffraction Dissociation) and ATLAS collaborations, in which the proton was measured after the collisions in the PPS (Precision Proton Spectrometer) and AFP (ATLAS Forward Proton Detector), respectively allowed the experimental separation of fully elastic cases and those in which one proton survives the collision [27, 55].

By analyzing the collisions corresponding to the ATLAS collaboration studies, the four-momenta of intermediate photons can be approximated as:

$$q_1 \approx \left(x_1 \frac{\sqrt{s}}{2}, \vec{q}_{\perp 1}, x_1 \frac{\sqrt{s}}{2} \right), \quad q_2 \approx \left(x_2 \frac{\sqrt{s}}{2}, \vec{q}_{\perp 2}, -x_2 \frac{\sqrt{s}}{2} \right). \tag{2.41}$$

while the longitudinal momentum fraction of the photons reflecting the measurement of forward protons takes into account only lepton variables and approximates the produced dilepton as a single object:

$$\xi_{ll}^{+} = \frac{M_{ll}}{\sqrt{s}} \exp(+Y_{ll}), \quad \xi_{ll}^{-} = \frac{M_{ll}}{\sqrt{s}} \exp(-Y_{ll}), \tag{2.42}$$

where

$$\xi_1 = \xi_{ll}^{+}, \quad \xi_2 = \xi_{ll}^{-}. \tag{2.43}$$

The analysis of these processes also takes into account the use of the SuperChic 4 generator based on the impact parameter space (see Ref. [56]), in which this proton energy loss is calculated more directly from the energy of both outgoing protons (E_A and E_B):

$$\xi_1 = \frac{\sqrt{s}/2 - E_A}{\sqrt{s}/2}, \quad \xi_2 = \frac{\sqrt{s}/2 - E_B}{\sqrt{s}/2}. \tag{2.44}$$

Important for further analysis of these specific collisions are invariant mass, rapidity, and transverse momentum of the lepton pair:

$$\begin{aligned} M_{ll} &= \sqrt{(E_{l^+} + E_{l^-})^2 - (\vec{p}_{l^+} + \vec{p}_{l^-})^2}, \\ Y_{ll} &= \frac{1}{2} \ln \frac{E_{l^+} + E_{l^-} + (p_{z\,l^+} + p_{z\,l^-})}{E_{l^+} + E_{l^-} - (p_{z\,l^+} + p_{z\,l^-})}, \\ p_{\perp ll} &= |\vec{p}_{\perp ll}| = \sqrt{(\vec{p}_{\perp\,l^+} + \vec{p}_{\perp\,l^-})^2}, \end{aligned} \tag{2.45}$$

and masses of the proton remnants

$$M_X^2 = E_X^2 - p_X^2, \quad M_Y^2 = E_Y^2 - p_Y^2. \tag{2.46}$$

Theoretically, protons can also be emitted from the remnant system, which would require taking into account additional fragmentation of proton remnants that are not fully

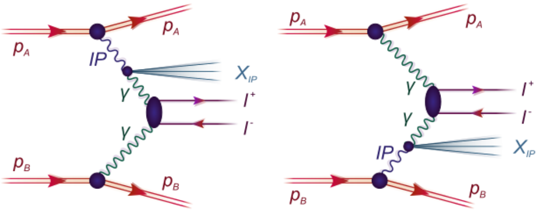

Figure 2.5: Dilepton diffractive production mechanism in the proton-proton collision.

controlled. However, such protons have a small longitudinal momentum fraction x_i, for which $\xi_i = 1 - x_i > 0.1$, which is beyond the measurement capabilities of Roman pots for both the ATLAS and CMS experiments.

The only additional process that can be detected by the above-mentioned detectors is the diffraction mechanism visible in Fig. 2.5. However, it has been shown, based on HERA measurements, that it is recorded only in $10\,\%$ cases of measurements from Ref. [57]. Moreover, the pomeron remnant that occurs in such a case would destroy the rapidity gap veto and the rapidity gap, which is also taken into account in this analysis. This discussion allows one to exclude the involvement of this mechanism as well while contributing to a significant reduction in the contribution of double dissociation.

This analysis concerns the processes of two-photon dimuon production in proton-proton collisions for an accelerator energy of $13\,\mathrm{TeV}$. It should be mentioned that typical lepton cuts were used during the calculations, which are $-2.5 < y_1, y_2 < 2.5$, $p_{\perp 1}, p_{\perp 2} > 15\,\mathrm{GeV}$ and $0.035 < \xi_{1,2} < 0.08$, while did not take into account all the conditions imposed by the ATLAS collaboration in Ref. [27], such as the mass window around Z-boson mass m_Z and the lepton acoplanarity. The calculations were made using the codes owned by our group which are realized in the transverse momentum space and the SuperChic 4 generator based on the impact parameter space that allowed to analyze the survival of the rapidity gap, see Ref. [56]. Similarly, the results for muons and electrons turned out to be so close that the presented muon distributions are almost identical to those for electrons, especially for such high cuts on the muon/electron transverse momentum, which is shown in the case of the total cross-section in Table 2.2.

Table 2.1 contains the total cross-sections for dimuon production depending on the type of collision, the used cuts, and the soft rapidity gap survival effect. The results of calculations in which only the rapidity cuts of the muon pair were taken into account show that the double inelastic collision cross-section is the largest when soft gap survival

reaction	$\sigma_{without\,GSE}$	$\sigma_{with\,GSE}$	S_G
$-2.5 < Y_{ll} < 2.5, \quad p_{\perp\,1,2} > 15\,\mathrm{GeV}$			
elastic-elastic	0.54438	0.50402	0.926
inelastic-elastic	0.89595	0.64283	0.717
elastic-inelastic	0.89587	0.64254	0.717
inelastic-inelastic	1.62859	0.24172	0.148
$-2.5 < y_{1,2} < 2.5$ in addition			
elastic-elastic	0.42268	0.39355	0.931
inelastic-elastic	0.69241	0.51092	0.738
elastic-inelastic	0.69246	0.51087	0.738
$0.035 < \xi_{ll}^{\pm} < 0.08$ in addition			
elastic-elastic, cut on ξ_1	0.00762	0.00675	0.886
elastic-elastic, cut on ξ_2	0.00762	0.00675	0.886
inelastic-elastic, cut on ξ_2	0.02496	0.01324	0.530
elastic-inelastic, cut on ξ_1	0.02393	0.01238	0.517
$p_{\perp\,ll} < 5\,\mathrm{GeV}$ in addition			
inelastic-elastic, cut on ξ_2	0.00807	0.00437 (*)	0.541
elastic-inelastic, cut on ξ_1	0.00807	0.00437 (*)	0.542

Table 2.1: Integrated cross-section in pb for $\mu^+\mu^-$ production for $\sqrt{s} = 13\,\mathrm{TeV}$. The first rows of the table contain the results of calculations without any additional cuts - they include cuts on $p_{\perp\,1,2}$ and Y_{ll}, while the subsequent rows include cuts on $y_{1,2}, \xi$ and $p_{\perp\,ll}$, respectively. Additionally, the results are presented with (first column) and without (second column) rapidity gap survival effect, taking into account model no. 4 as implemented in SuperChic 4 (see also [58]). The last column refers to the average gap survival factor S_G, which is the ratio of the cross-sections from the other two. The (*) means 10 000 events only.

effects are not taken into account. After including them, it turns out that the cross-section decreases several times, thus giving the lowest cross-section among all the considered types of collisions. The decrease in the value of the cross-section after taking into account the soft gap survival effects is also visible for the remaining collisions, but it is much smaller, in particular for double elastic collisions, taking into account both the pair rapidity cuts and the single lepton.

Imposing cuts on $y_{1,2}$ causes a decrease in the total cross-section by approximately $0.2\,\mathrm{pb}$, while additional cuts on $\xi_{1,2}$ reduces its value by several dozen times, and a cut on $p_{\perp\,ll}$ contributes to another three-fold decrease in its value. In general, the calculated cross-sections are larger than the ATLAS collaboration's experimental data (see Ref. [27]), which is due to their use of more conditions.

It may also be noticed that individual dissociations, which usually give the same cross-section, differ in their value when applying cuts to ξ_1 and ξ_2 both, when the soft gap survival effect is taken into account, as well as when it is omitted. This is related to whether the cut is applied to the proton or its remnant.

The last column of Table 2.1 refers to the gap survival factor

$$S_G = \frac{\sigma_{with\,GSE}}{\sigma_{without\,GSE}}. \tag{2.47}$$

It reaches the highest value of approximately $90\,\%$ for fully elastic cases, while for double inelastic cases, it is only $15\,\%$, which means that the dimiuons produced in these inelastic processes rather come from mechanisms other than simple two-photon exchange and excludes them from further analysis. For single dissociations, it is more than $70\,\%$ when the forward proton is not measured and more than $50\,\%$ when it is measured.

It is also interesting to compare the results from different models of the proton structure function, which was achieved by performing calculations using codes owned by our group. The results of these calculations for a situation that does not take into account the rapidity gap survival effects are presented in Table 2.2. The first three columns correspond to the use of structure functions LUX-like, ALLM, and FFJLM, respectively, while the last one refers to electron production using the LUX-like function for the inelastic protons.

Both elastic-elastic and inelastic collision results for the LUX-like function coincide with the results from the SuperChic generator for all cuts used. Larger differences appear in the remaining structure functions. For most of the assumed conditions, larger results correspond to ALLM, while the additional cut on $p_{\perp,ll}$ is characterized by the largest cross-section at FFJLM, which almost does not decrease compared to the results for the forward proton measurement.

The results of calculations for the production of electrons in analogous collisions confirm that, as assumed, the resulting differences are minimal, which is related to the similarity of muons and electrons, including the insignificant difference in masses between them. Similar results exist for both the elastic and inelastic cases and all superimposed cuts.

reaction	LUX-like	ALLM	FFJLM	$pp \to e^+e^-$ LUX-like
$-2.5 < Y_{ll} < 2.5, \quad p_{\perp\,1,2} > 15\,\mathrm{GeV}$				
elastic-elastic	0.53950			0.53936
inelastic-elastic	0.81306	0.72981	0.61800	0.81512
elastic-inelastic	0.81306	0.72849	0.61680	0.81374
inelastic-inelastic	1.36146	1.07518	0.71843	1.36372
$-2.5 < y_{1,2} < 2.5$ in addition				
elastic-elastic	0.41925			0.41926
inelastic-elastic	0.63456	0.57121	0.48982	0.63465
elastic-inelastic	0.63364	0.57025	0.48927	0.63357
$0.035 < \xi_{ll}^{\pm} < 0.08$ in addition				
elastic-elastic, cut on ξ_1	0.00755			0.00755
elastic-elastic, cut on ξ_2	0.00755			0.00755
inelastic-elastic, cut on ξ_2	0.01836	0.01664	0.00957	0.01836
elastic-inelastic, cut on ξ_1	0.01833	0.01663	0.00957	0.01832
$p_{\perp\,ll} < 5\,\mathrm{GeV}$ in addition				
inelastic-elastic, cut on ξ_2	0.00766	0.00704	0.00955	0.00766
elastic-inelastic, cut on ξ_1	0.00765	0.00702	0.00955	0.00765

Table 2.2: Integrated cross-section in pb for $\mu^+\mu^-$ production for $\sqrt{s} = 13\,\mathrm{TeV}$ for different parametrization of structure functions calculated using our group codes. The first rows of the table contain the results for calculations without any additional cuts - they include cuts on $p_{\perp\,1,2}$ and Y_{ll}, while the subsequent rows include cuts on $y_{1,2}, \xi_{ll}^{\pm}$ and $p_{\perp\,ll}$, respectively. Additionally, the last column presents results for electron-positron production.

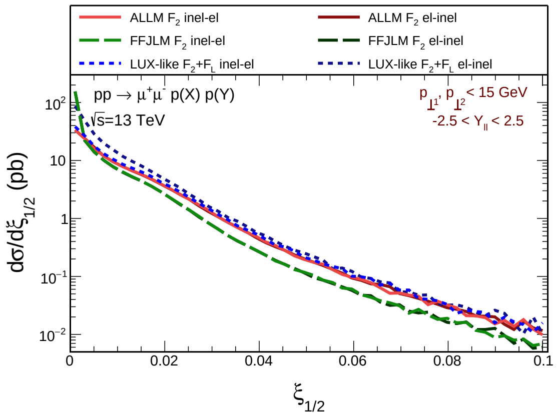

Figure 2.6: Dimuon $\xi_{1,2}$ dependence of the cross-section for different contributions and models considered.

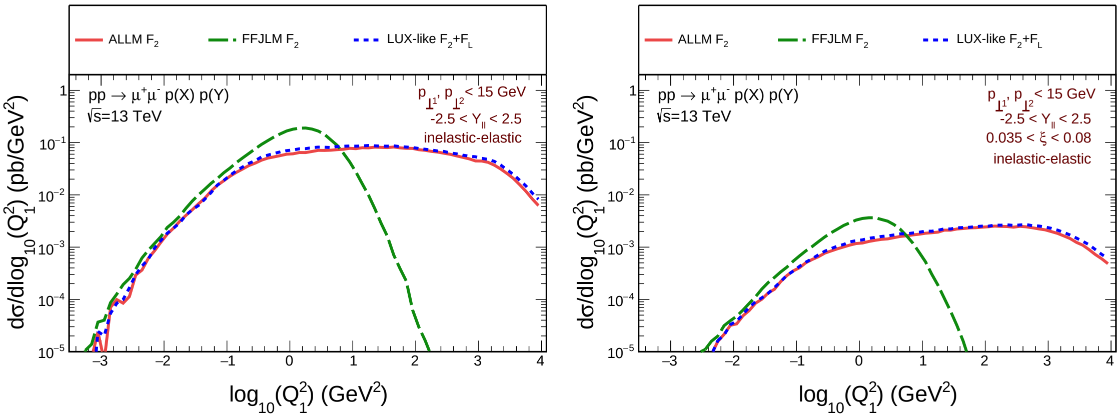

Figure 2.7: Photon virtuality dependence of the cross-section for different models without (left) and with (right) ξ cuts.

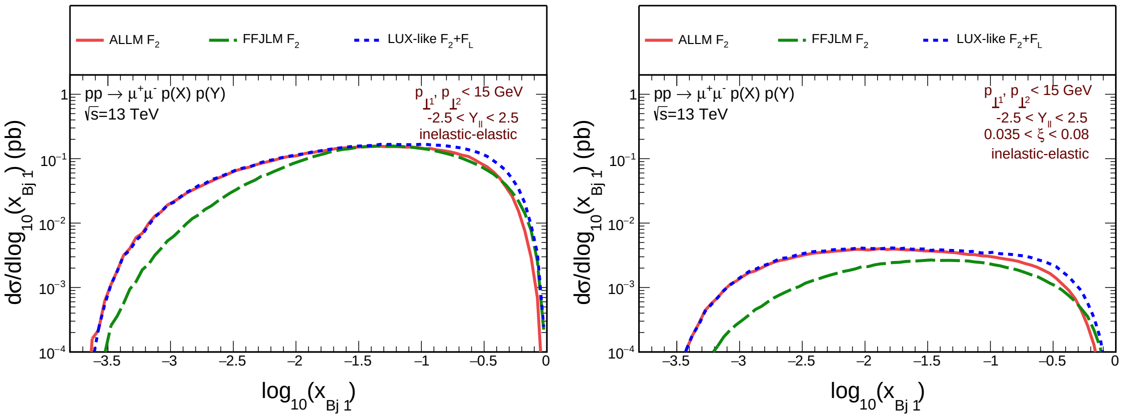

Figure 2.8: Bjorken variable x_{Bj} dependence of the cross-section for different models considered without (left) and with (right) ξ cuts.

A more accurate understanding of the results visible in Table 2.1 and Table 2.2 is possible by analyzing the distributions of cross-sections in various kinematic variables. The first is the distribution in $\xi_{1,2}$ for double elastic and single dissociations, respectively from Fig. 2.6, where a very noticeable drop in the differential cross-section of five orders of magnitude is visible. This corresponds to a significant decrease in the cross-section when protons are measured in the forward proton detector.

An equally important aspect is the dependence of the structure functions on their variables, visible in the differential cross-section distributions in the Q^2 and the x_{Bj}.
In Fig. 2.7 shows a significant similarity of the distributions for the ALLM and LUX-like functions in Q^2, while FFJLM shows the highest value at Q^2 close to 0.0 and then decreases by as much as four orders of magnitude before $Q^2 = 2.0\,\mathrm{GeV}^2$. This situation is similar before and after taking into account the cuts on ξ, which affects the approximation of the values of the differential cross-sections without changing the shape of the curves.

Whereas, the distribution in the Bjorken variable x visible in Fig. 2.8 is characterized by much smaller differences between the individual structure functions. Again, the results corresponding to ALLM and LUX-like almost coincide with each other, but this time the FFJLM distribution only has a slightly faster decline with decreasing x_{Bj}.

This situation is opposite for the distributions of the proton remnant mass from Fig. 2.9, wherein the range of 1000 GeV a decrease in the cross-section by three orders of magnitude is visible, while at FFJLM it is almost instantaneous and the cross-section is close to zero already at $M_X \sim 100\,\mathrm{GeV}$.

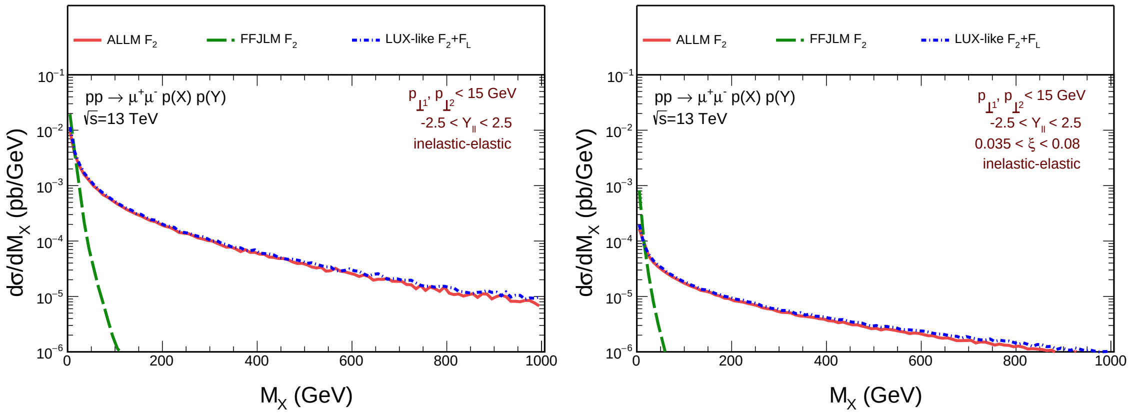

Figure 2.9: Proton remnant mass dependence of the cross-section for different models considered without (left) and with (right) ξ cuts.

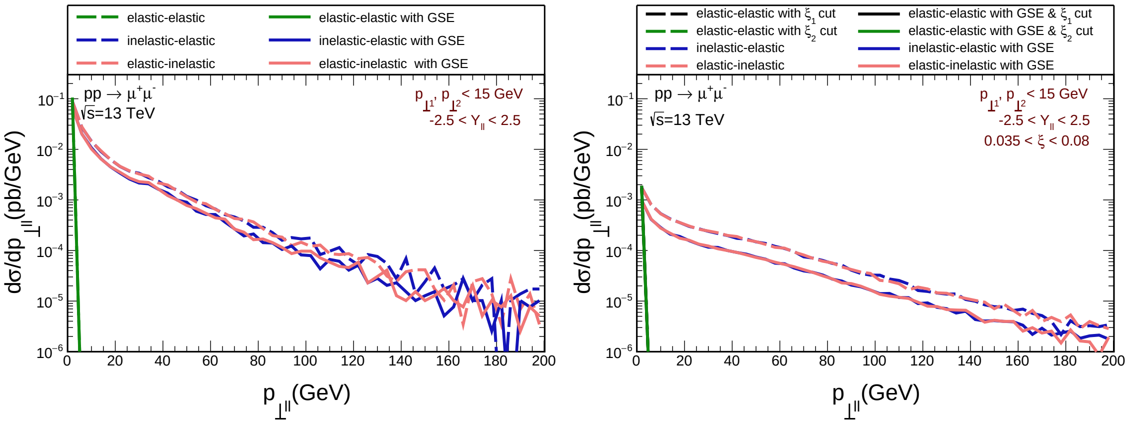

Figure 2.10: Dimuon transverse momentum dependence of the cross-section for different contributions considered without (left) and with (right) ξ cuts (SuperChic calculation).

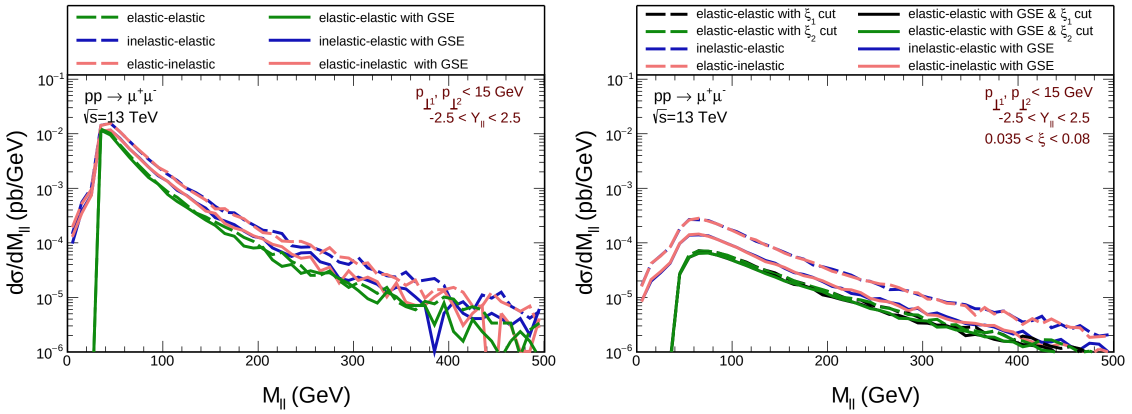

Figure 2.11: Dimuon invariant mass dependence of the cross-section for different contributions considered without (left) and with (right) ξ cuts (SuperChic calculation).

Similar to Fig. 2.6 is the case in Fig. 2.10, where the distribution of the differential cross-section in $p_{\perp\,ll}$ also decreases by four orders of magnitude over the entire analyzed range. Therefore, imposing a drastic cut on $p_{\perp\,ll} < 5\,\mathrm{GeV}$, where the difference in the value of the total cross-section is within one order of magnitude, contributes to a significant reduction in the value of the differential cross-section. The situation is analogous for cases taking into account forward proton measurement, although here the maximum reaches only the order of $10^{-3}\,\mathrm{pb/GeV}$ with a similar level of minimum values. Double elastic collisions, however, in both cases are characterized only by a peak corresponding to very small transverse momenta, not contributing to momenta greater than $10\,\mathrm{GeV}$, as expected.

However, the distribution of the cross-section as a function of the invariant mass of the muon pair visible in Fig. 2.11 starts with an increase corresponding to the masses below $M_{ll} < 60\,\mathrm{GeV}$ which is associated with the occurrence of small virtualities for both elastic and inelastic cases based on FFJLM and this, in combination with the imposed cuts, contributes to the production of pairs of particles with slightly larger invariant masses, after that a slow decrease in the cross-section with a further increase in the mass value may be observed. A similar effect is visible when cuts on $\xi_{1,2}$ are taken into account, but in this case, larger differences are seen in the cross-section values for the double elastic and single dissociation cases. Furthermore, similarly to the distributions in $p_{\perp\,ll}$, taking into account the effects of surviving a rapidity gap contributes to a slight decrease in the values of the inelastic-elastic and elastic-inelastic distributions while maintaining the shape of the curves. These distributions overlap for both types of single dissociations.

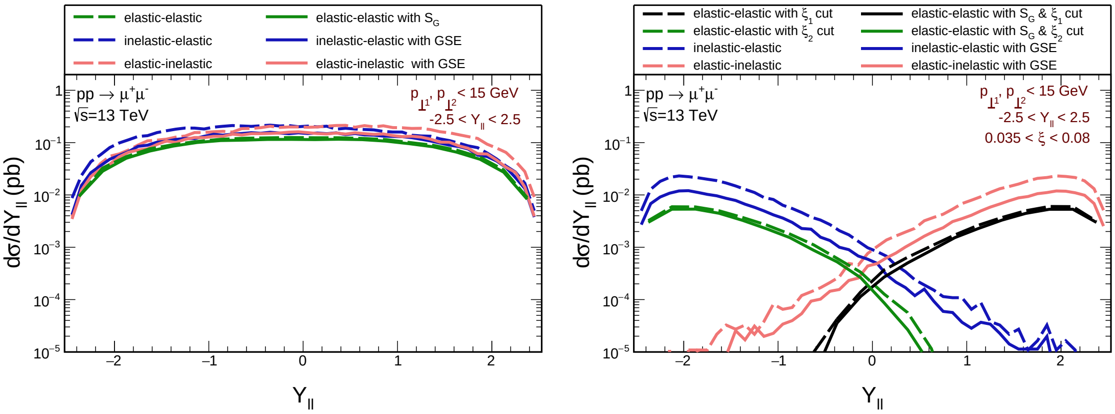

Figure 2.12: Dimuon rapidity dependence of the cross-section for different contributions considered without (left) and with (right) ξ cuts (SuperChic calculation).

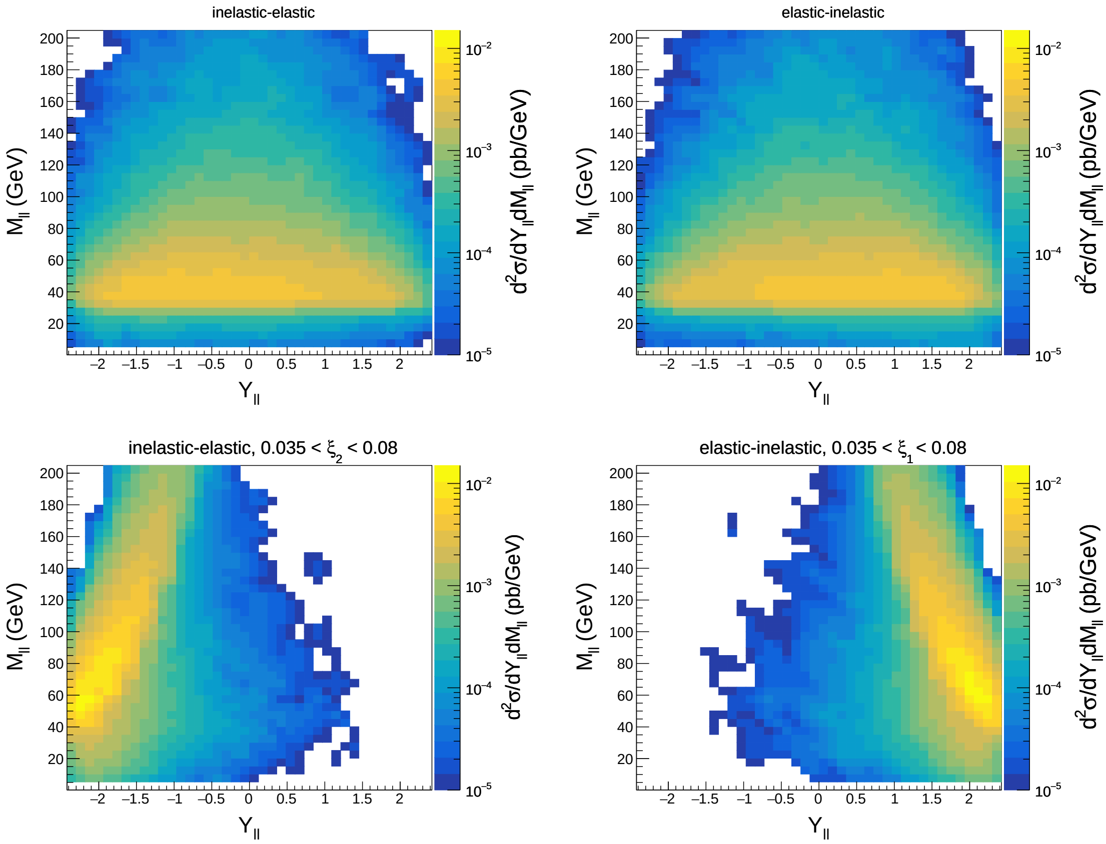

Figure 2.13: Two-dimensional dimuon rapidity and invariant mass dependence of the cross-section for different contributions considered without (top) and with (bottom) ξ cuts (SuperChic calculation).

The effects of imposing a cut on $\xi_{1,2}$ are particularly visible for the rapidity distributions of the muon pair in Fig. 2.12. It is visible that before this cut is applied, the distributions of inelastic-elastic and elastic-inelastic collisions almost overlap, especially when the soft gap survival effects are taken into account. Applying the cut implies that the distribution for each of them decreases as one approaches the opposite side of the system. In general, a minimum of single dissociations is obtained for $Y_{ll} \approx 0$. This effect is also visible for double elastic collisions.

The superimposition of the results of the decrease in cross-sections in the functions M_{ll} and Y_{ll} is shown in Fig. 2.13. It is evident from this figure that the maximum cross-section for muon production when forward protons are not measured corresponds to a rapidity close to zero and masses in the range $30 < M_{ll} < 60\,\mathrm{GeV}$. This situation changes dramatically when a cut on $\xi_{1,2}$ is applied. The chance of finding a muon in especially $Y_{ll} \approx 0$ is then much smaller, although it is possible with large masses. This is the reason for the dip observed in $d\sigma/dY_{ll}$ at $Y_{ll} = 0$ by the ATLAS collaboration in Ref. [27].

Similarly to the total cross-section, gap survival factors were calculated for the differential cross-sections as a ratio of the cross-section with the rapidity gap survival effect (GSE) to its counterpart without including this effect:

$$\begin{aligned} S_G(M_{ll}) &= \frac{d\sigma/dM_{ll}\big|_{with\,GSE}}{d\sigma/dM_{ll}\big|_{without\,GSE}}, \\ S_G(p_{\perp\,ll}) &= \frac{d\sigma/dp_{\perp\,ll}\big|_{with\,GSE}}{d\sigma/dp_{\perp\,ll}\big|_{without\,GSE}}, \\ S_G(Y_{ll}) &= \frac{d\sigma/dY_{ll}\big|_{with\,GSE}}{d\sigma/dY_{ll}\big|_{without\,GSE}}. \end{aligned} \tag{2.48}$$

The distributions of the gap survival factor, similar to the distributions of the differential cross-sections, are presented depending on the imposition of cuts on the forward proton. In Ref. [1] the significant oscillations in the distribution of the gap survival factor in M_{ll}, $p_{\perp\,ll}$, and Y_{ll} occurs. They were thought to be caused by insufficient calculation statistics but the occurrence of oscillations in the distributions in the functions of the M_{ll} (Fig. 2.14), $p_{\perp\,ll}$ (Fig.2.15), and Y_{ll} (Fig. 2.16) corresponds rather to the significant decrease of the differential cross section in these variables. Therefore, in this thesis, it was decided to present only those areas of M_{ll}, $p_{\perp\,ll}$, and Y_{ll} for which the decrease in the differential cross section does not exceed two orders of magnitude. It is now clearly visible, that in the value of the gap survival factor visible in the functions of M_{ll}, and $p_{\perp\,ll}$

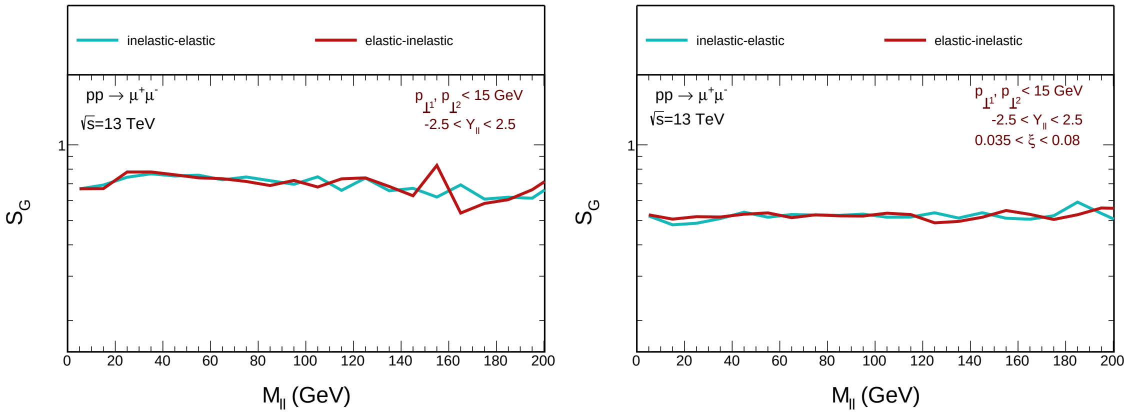

Figure 2.14: Dilepton invariant mass dependence of the gap survival factor without (left) and with (right) ξ cuts (SuperChic calculation).

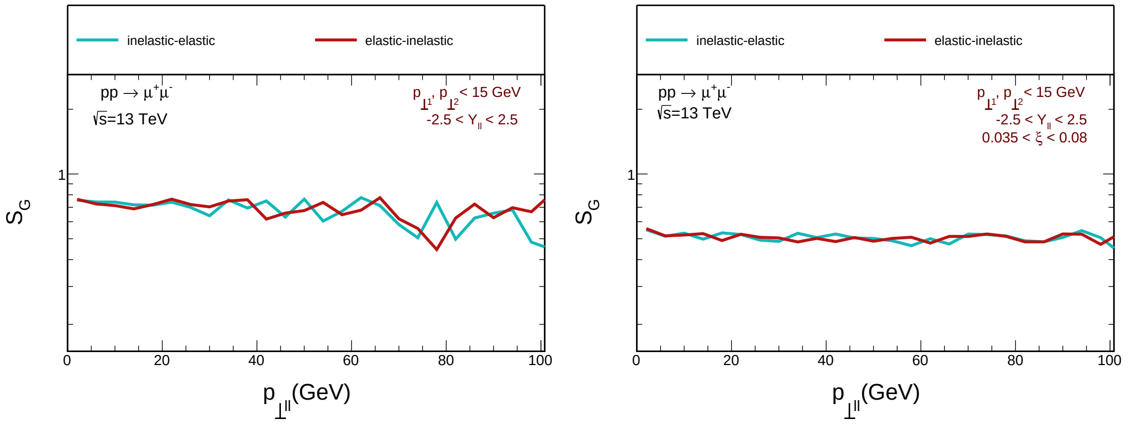

Figure 2.15: Dilepton transverse momentum dependence of the gap survival factor without (left) and with (right) ξ cuts (SuperChic calculation).

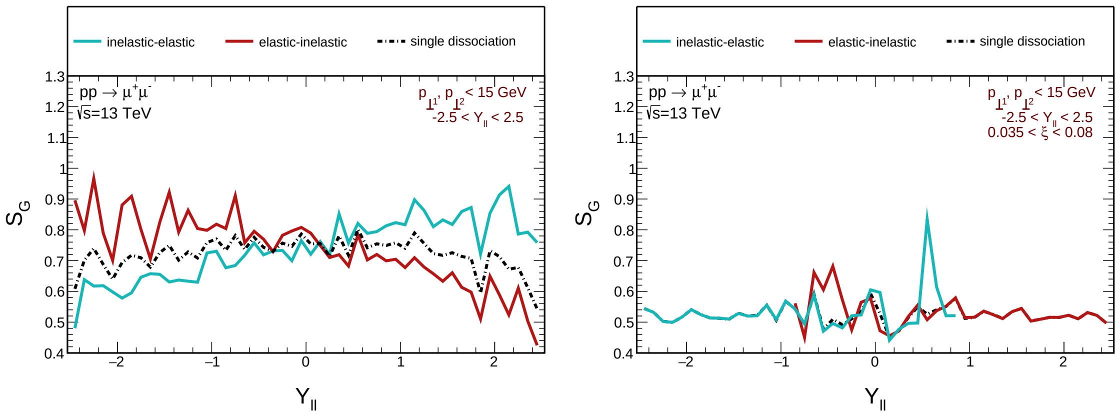

Figure 2.16: Dilepton rapidity dependence of the gap survival factor without (left) and with (right) ξ cuts (SuperChic calculation).

the linear relationship occurs. In addition, the averaged value for calculations assuming a proton measurement is compared across these variables, as are the distributions taking into account the overlap of these cuts. However, the value of the gap survival factor for the second of these cases is several percent lower.

The oscillations occurring in the gap survival factor distribution in the dilepton rapidity function are larger when taking into account cuts to the longitudinal momentum of the proton. However, in this case, also the dependence of the factor for single dissociation is almost linear. There is a strong dependence of the gap survival factor on Y_{ll} both for the inelastic-elastic and elastic-inelastic cases, as well as for single dissociation when the proton is not measured. This effect may be difficult to measure experimentally as in this case, one measures the sum of both components, where the effect averages and becomes more or less independent of the rapidity.

Both the total values and the dependence on various variables of the gap survival factor indicate the destruction of the rapidity gap by the particles produced, which also needs to be explained. However, the rapidity gap was not explicitly imposed in [27] and [55]. The most probable is the (mini)jet emission in single dissociation processes. The resulting quark-antiquark pair creates hadrons (mainly pions) that can destroy the rapidity gap, which was discussed in e.g. [59, 60, 26]. The diagram of such emission for inelastic-elastic and elastic-inelastic collisions is shown in Fig. 2.17.

Fig. 2.18 shows the distribution of the differential cross-section as a function of the rapidity of such a jet for inelastic-elastic and elastic-inelastic contributions. The corresponding gap survival factor is 0.8 and 0.5, respectively. The probability of no emission

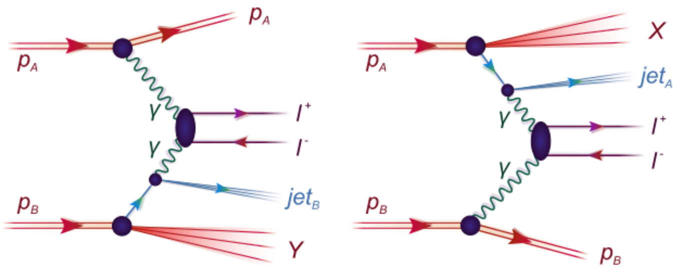

Figure 2.17: (mini)jet production diagram due to quark/antiquark knock-out.

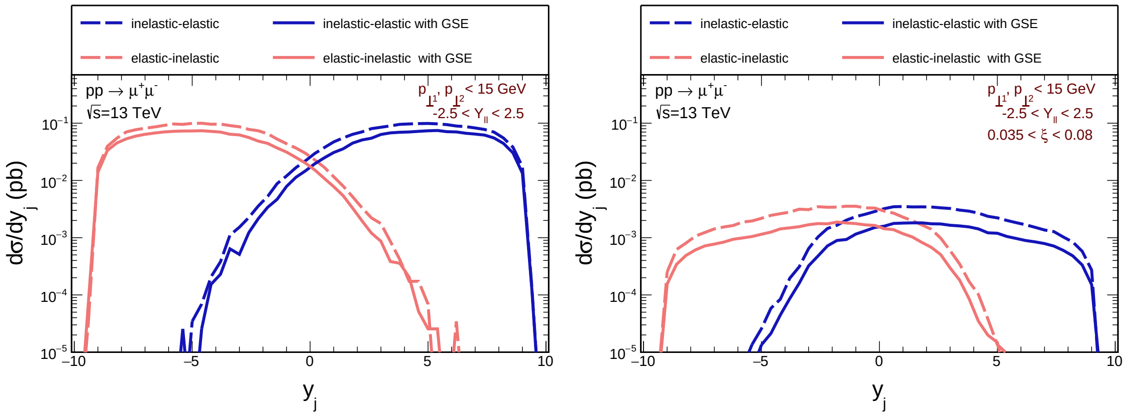

Figure 2.18: Rapidity of the (mini)jet dependence of the cross-section for single dissociations including gap survival effect correction (solid lines) and neglecting this effect (dashed lines), without (left) and with (right) ξ cuts (SuperChic calculation).

around the $\gamma\gamma \rightarrow \mu^+\mu^-$ vertex is however, more difficult to calculate and requires taking into account the remnant hadronization which is model dependent. The results of these two methods of calculation agree in terms of their order and magnitude.

Finally, Table 2.3 shows the probability that the (mini)jet has $y_{jet} < -2.5$ or $y_{jet} > 2.5$, which means that it is outside the main detector. The values obtained are in magnitude consistent with the gap survival factor values in Table 2.1. As before, applying cuts to $\xi_{1,2}$ reduces the corresponding gap survival factor (minijet), while imposing a cut to $p_{\perp,ll} < 5\,\text{GeV}$ increases it back, as in the ATLAS experiment. This condition must, of course, be taken into account when the rapidity gap survival condition is imposed experimentally. The situation is less clear when μ^+ and μ^- are separated, as in the ATLAS [27] experiment.

This analysis assumes that (mini)jet particles emitted from the same vertex as the leptons always mix conditions as long as they are emitted in the same rapidity range

contribution	without GSE	with GSE
$-2.5 < Y_{ll} < 2.5$		
inelastic-elastic	0.76278	0.78898
elastic-inelastic	0.76304	0.78756
$-2.5 < y_{1,2} < 2.5$ in addition		
inelastic-elastic	0.76926	0.78744
elastic-inelastic	0.77366	0.79250
$0.035 < \xi^{\pm}_{1,2} < 0.08$ in addition		
inelastic-elastic	0.53118	0.53614
elastic-inelastic	0.52430	0.53976
$p_{\perp\, ll} < 5\,\mathrm{GeV}$		
inelastic-elastic	0.83462	0.84350 (*)
elastic-inelastic	0.83144	0.84960 (*)

Table 2.3: Gap survival factor due to (mini)jets emission. The first rows of the table contain the results for calculations without any additional cuts - they include cuts on $p_{\perp\, 1,2}$ and Y_{ll}, while the subsequent rows include cuts on $y_{1,2}, \xi_{1,2}$ and $p_{\perp\, ll}$, respectively. The (*) means 10 000 events only.

as the measured leptons. The range considered is related to the geometry of the main ATLAS (and CMS) detector. In practice, the experiment rather assumes the condition on $R(track, l^+) > R_0$ and $R(track, l^-) > R_0$, which means that there is no emission in the cones around both leptons, for the ATLAS experiment, $R_0 = 0.01$ was used. However, it would be interesting to experimentally examine the gap survival factor as a function of R_0.

2.2 Proton-lead collisions

Dileptons can also be produced similarly in nuclear or proton-nucleus collisions, among others. In both of those collisions, the contribution of two-photon exchanges is rather small, but imposing appropriate conditions on the rapidity gap, as in [61], makes it possible to measure photon mechanisms also in this type of collisions. The gap survival probability is expected to depend on the kinematics of the process, which should be applied when asking for a rapidity gap. However, the modeling of the latter goes beyond the scope of this analysis. Furthermore, it concentrates on the contribution to inclusive observables. It is true that until recently, nucleus-nucleus collisions, in particular, were divided into real hadronic collisions, with impact parameter $b < R_1 + R_2$, where the mechanisms involved are analogous to those in classic proton-proton collisions, and ultraperipheral collisions with $b > R_1 + R_2$ dominated by photon-photon fusion. It turns out, however, (see e.g. [62]) that two-photon processes are also present in semi-central collisions, where they actually dominate at very large transverse momenta of the lepton pair. Proton-nucleus collisions have not been thoroughly studied in this respect, although in [63] an analysis corresponding to the ATLAS experimental equipment is visible, and in [64] the ALICE collaboration presents measurements of dilepton production as part of the exchange of photons in proton-nucleus collisions, which makes it possible to relate the theoretical predictions to experimental data.

The main difference in this case concerning proton-proton collisions will be the fact that the nucleus is only a source of elastic photons, hence there are only two types of collisions shown in Fig. 2.19, which are double elastic and single dissociations.

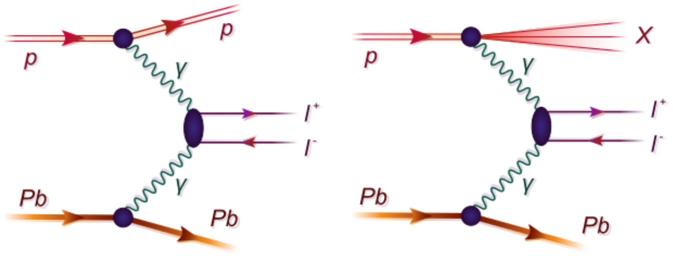

Figure 2.19: Different mechanisms of electron-positron production in proton-nucleus collisions for $\gamma\gamma$ mechanism.

In the $\mathrm{k}_\perp$ factorization approach, the cross-section on $p + Pb \to Pb + l^+l^- + X(p)$, where X(p) is a proton or its remnant, is expressed as follows:

$$\begin{aligned}\sigma &= S^2 \int dx_p dx_{Pb} \frac{d^2\vec{q}_\perp}{\pi} \left[\frac{d\gamma^p_{el}(x_p, Q^2)}{dQ^2} + \frac{d\gamma^p_{ine}(x_p, Q^2)}{dQ^2} \right] \\ &\times \gamma^{Pb}_{el}(x_{Pb}) \sigma_{\gamma^*\gamma \to l^+l^-}(x_p, x_{Pb}, \vec{q}_\perp),\end{aligned} \tag{2.49}$$

where $\sigma_{\gamma^*\gamma\to l^+l^-}$ is the off-shell elementary cross-section from Eq. (2.28), while γ^p_{el} and γ^p_{ine} are elastic and inelastic photon fluxes of the proton from Eq. (2.39), respectively. A rapidity gap survival factor that depends on the kinematics of the process is $S \le 1$, however, for the inclusive observables it equals one.

Then, to correctly express the elastic photon flux of the nucleus $\gamma_{el}^{Pb}(x_{Pb})$, according to [40] there should be a replacement:

$$\frac{4m_p^2 G_E^2(Q^2) + Q^2 G_M^2(Q^2)}{4m_p^2 + Q^2} \to Z^2 F_{em}^2(Q^2), \tag{2.50}$$

where $Z = 82$ is the charge of the nucleus and $F_{em}(Q^2)$ is its charge form factor. This factor in the case of the ^{208}Pb nucleus may be expressed by the parametrization used in the STARlight MC generator [65]:

$$F_{em}(Q^2) = \frac{3}{(QR_A)^3}\Big[\sin(QR_A) - QR_A\cos(QR_A)\Big]\frac{1}{1+a^2Q^2}, \tag{2.51}$$

with $Q = \sqrt{Q^2}$, $R_A = 1.1A^{1/3}\,\mathrm{fm}$, A $= 208$ and $a = 0.7\,\mathrm{fm}$.
Importantly, despite the dependence of the fluxes on the $\vec{q}_\perp$ direction, for collinear case, the averaging over $\vec{q}_\perp$ directions in the off-shell cross-sections replaces the average of photon polarization.

2.2.1 Production of e^+e^- in p-Pb collision for ALICE kinematics

The experimental measurements of dielectron production in proton-lead collisions in $5.02\,\mathrm{TeV}$ presented in [64] by the ALICE collaboration assume the division of the kinematic region into two regions of invariant masses, which are the low-mass region (LMR) covering masses in the range $0.5 < M_{ee} < 1.1\,\mathrm{GeV}$ and the intermediate-mass region (IMR) with masses in the range $1.1 < M_{ee} < 2.7\,\mathrm{GeV}$, while the total cross-sections for such processes calculated based on codes owned by our group are presented in Table 2.4.

Structure function approaches	σ_{LMR} (nb)	σ_{IMR} (nb)
elastic	2938.72	507.04
ALLM	329.72	179.07
FFJLM	653.07	347.08
LUX-like	346.53	191.40
KB	387.93	205.27

Table 2.4: Total cross-section for e^+e^- production in pPb collisions in both ALICE mass regions and different approaches.

This table includes the four structure functions mentioned in Section 2.1.4, which are ALLM [41, 42], FFJLM [43], LUX-like [47] and KB [54], whose dependence on Bjorken-x and photon virtuality are shown in Fig. 2.4.

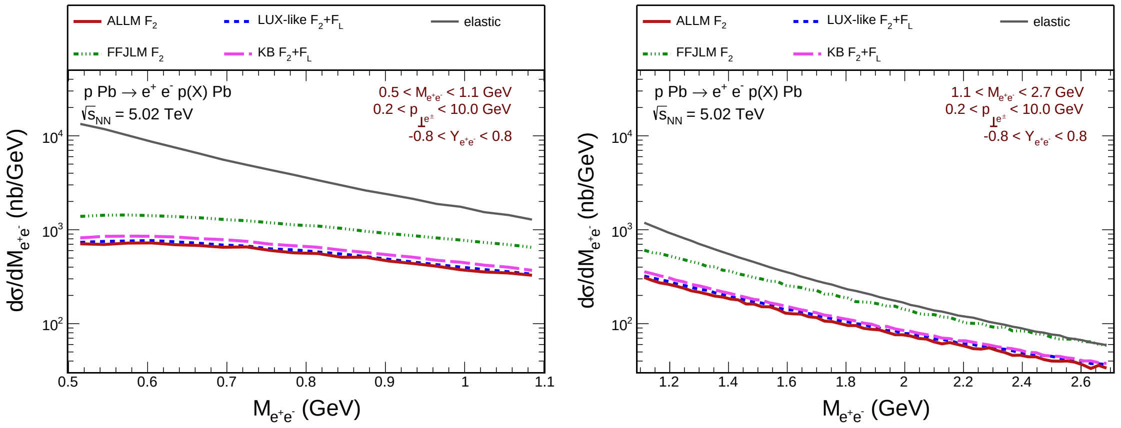

Figure 2.20: Dielectron invariant mass dependence of the cross-section for LMR (left) and IMR (right).

The cross-section is approximately twice as large for LMR as for intermediate masses in the case of proton dissociation, and this difference is much greater in the case of semi-elastic collisions. The results corresponding to the ALLM, LUX-like, and KB parametrizations are quite similar, while FFJLM significantly outperforms them in both mass areas. The elastic collisions have the main contribution, which is expected in this kinematic.

The differences in the total values of the cross-sections also correspond to the distribution of the differential cross-section as a function of the dielectron invariant mass from Fig. 2.20, which shows a significant dominance of elastic cases in the area of small masses. The predominance of elastic processes is also visible for IMR, but this cross-section almost coincides with the distribution based on FFJLM at the upper limit of the considered area. The results obtained based on this parametrization give curve shapes identical to the others, but they differ in value.

The dielectron transverse momentum distribution corresponds directly to the ALICE collaboration measurements (see Fig. 2.21). However, this experiment takes into account not only the exclusive production of dielectron, but also inclusive processes, and hence the insignificant contribution of the mechanisms considered in this work to the experimental measurements carried out is visible, despite the similar shape of the distributions.

The dominance of elastic processes in the area of small transverse momenta is also visible, while for $p_{\perp e^+e^-} > 1\,\mathrm{GeV}$ the predominant contribution comes from proton dissociation. Moreover, there are differences in the distributions for individual structure function models, but they concern transverse momenta larger than $3\,\mathrm{GeV}$ for which the

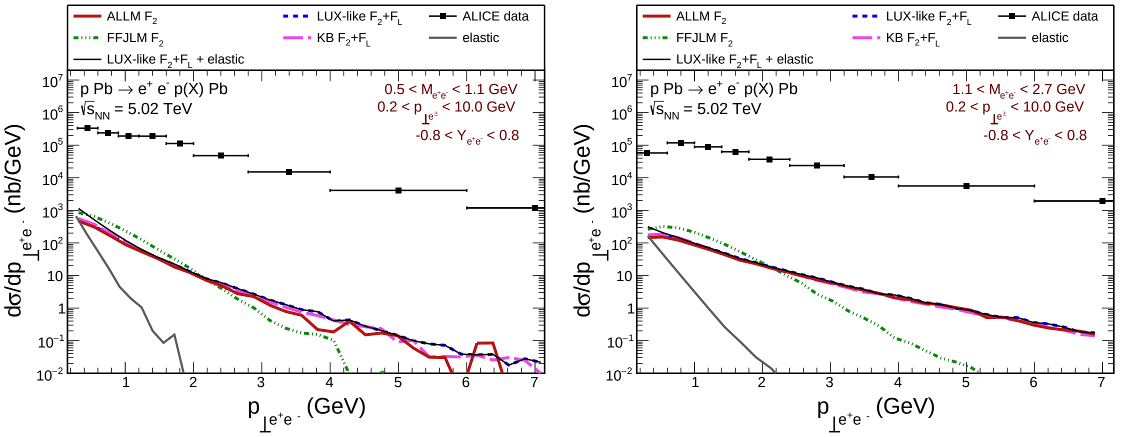

Figure 2.21: Dielectron transverse momentum dependence of the cross-section for LMR (left) and IMR (right).

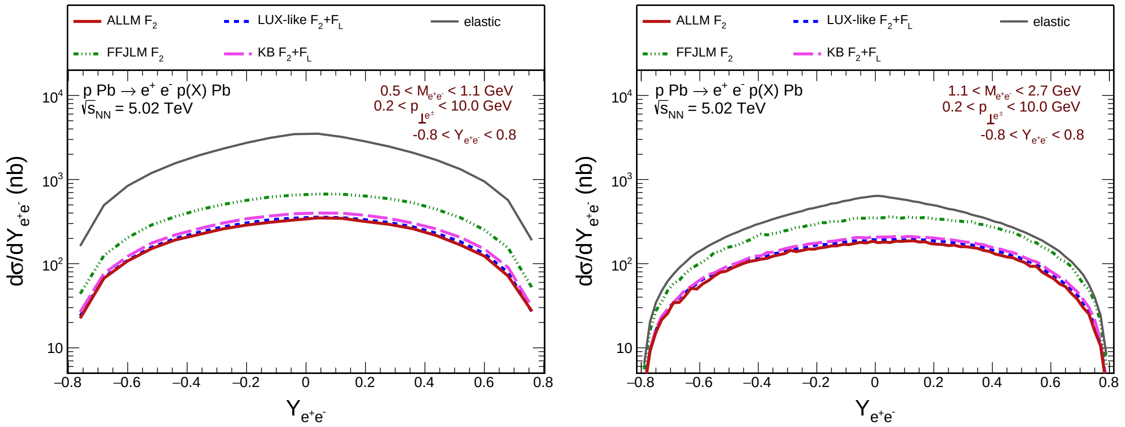

Figure 2.22: Dielectron rapidity dependence of the cross-section for LMR (left) and IMR (right).

value of the cross-sections is rather small. The decrease in the value of the differential cross-section in the considered area of transverse momenta reaches as much as five orders of magnitude.

It is worth paying attention to the distribution as a function of the rapidity of the produced pair from Fig. 2.22. Similarly to Fig. 2.20, the distributions based on FFJLM have slightly larger values than the other three, while maintaining a similar shape. Moreover, a slight decrease in the value of inelastic cross-sections is visible here when taking into account intermediate masses, while the contribution of elastic cases decreases much more, almost equaling the FFJLM distribution. The distributions in this variable are also very similar to the analogous contributions to dilepton production in proton-proton collisions.

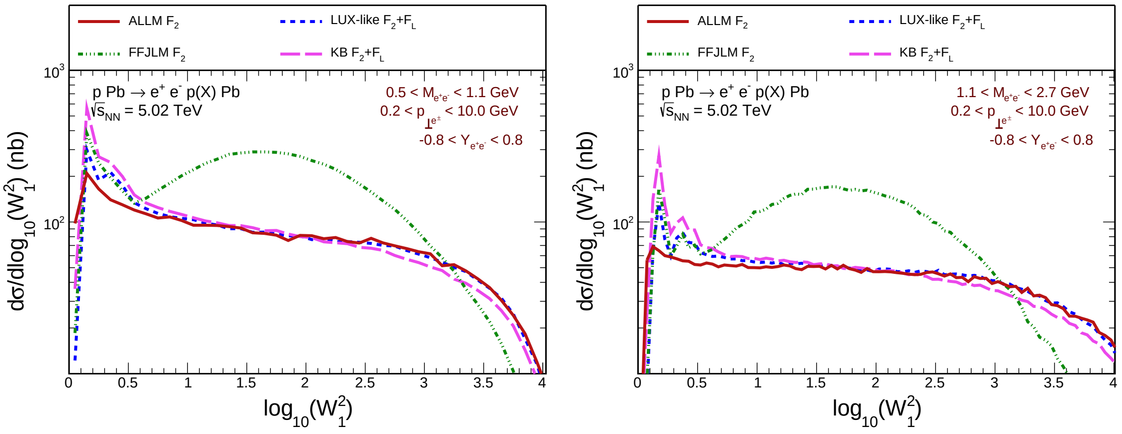

Figure 2.23: Energy of the photon-proton system dependence of the cross-section for LMR (left) and IMR (right).

It is also interesting to analyze the distributions in a rather theoretical variable, which is the energy in the photon-proton system $W_1^2 = \frac{Q_1^2}{x_{Bj\,1}} - Q_1^2 + m_p^2$. Representing the cross-section area in $\log_{10}(W_1^2)$ allows the entire energy region to be included in one figure. As in the previous cases, the biggest differences are in FFJLM, whose shape is now almost completely different from the others for $\log_{10}(W_1^2) > 1.0$.

The results for the remaining parametrizations also differ slightly, especially in the area of small W_1^2, where resonances occur. However, as was seen in the distributions in the invariant mass and dielectron rapidity, their contribution is not crucial for this mechanism.

It is worth understanding how the argument region of the structure function affects two-photon dilepton production also in proton-lead collisions, so Fig. 2.24 shows the distribution in both $\log_{10}(x_{Bj})$ and $\log_{10}(Q^2)$ for LMR, which in terms of the shape of the distributions is analogous to IMR. A large range of Bjorken variable x covered by the considered mechanisms is noticeable. Moreover, a significant part of the cross-section is located in the region of the $Q_1^2 < 1\,\mathrm{GeV}^2$, which is a purely non-perturbative region in which the parton description breaks.

The figure also shows resonances corresponding directly to those appearing in the distributions of individual parametrizations of the structure functions in the considered variables from Fig. 2.4 and the characteristic shape of the FFJLM distribution. Following the assumptions of ALLM parametrization, no resonances are visible. However, as previously shown, it slightly affects the distributions of physical variables.

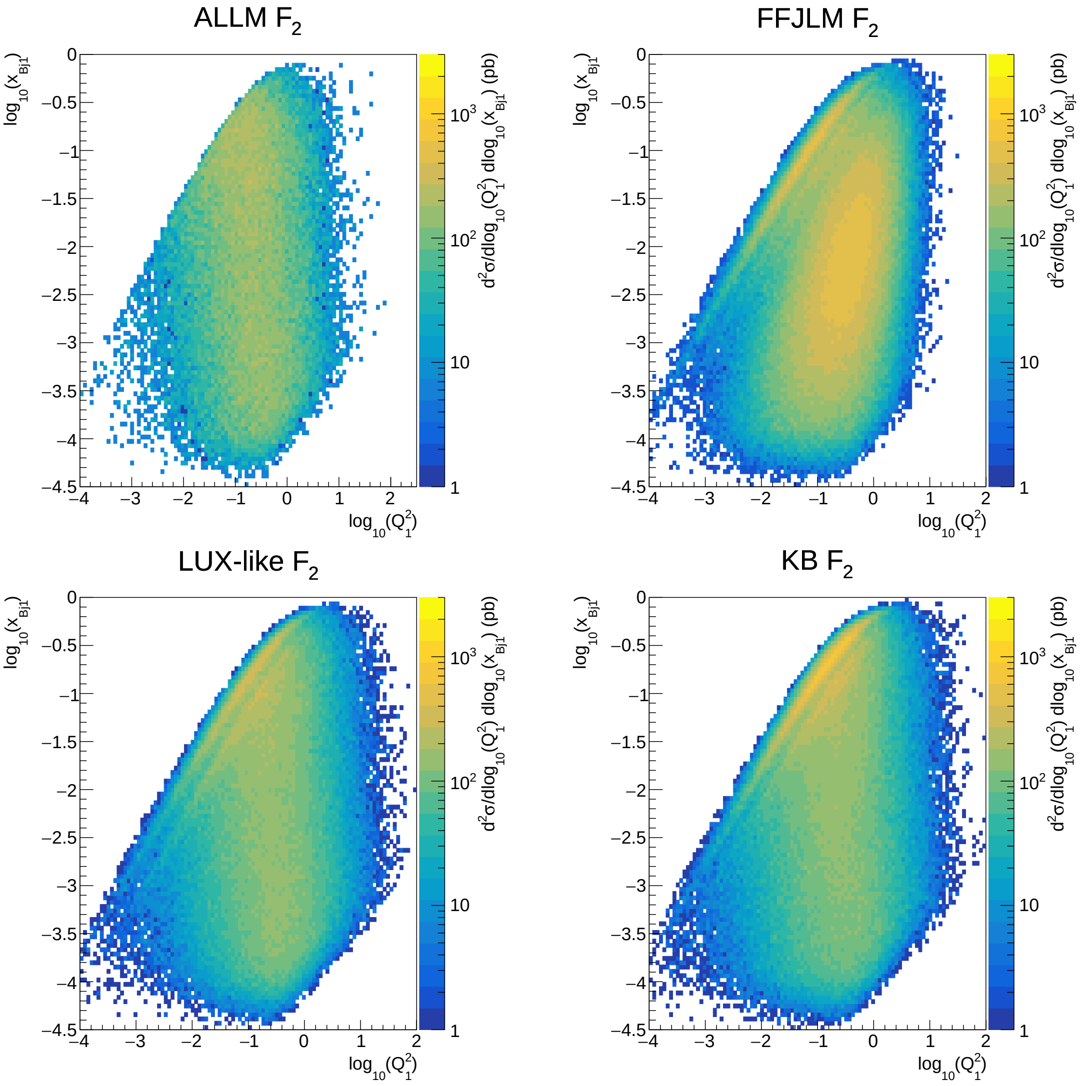

Figure 2.24: Virtuality and Bjorken variable-x dependence of the cross-section for LMR.

2.2.2 Rapidity gaps

As mentioned earlier, measuring the exclusive production of dileptons in the considered collisions is possible by imposing an additional condition on the rapidity gap. However, the calculations performed based of the codes owned by our group are performed in momentum space, where the exact correlation with the destruction of the rapidity gap is not known. Such an analysis is possible and applied for $AA \to AA\, l^+l^-$ in the impact parameter space by imposing geometric conditions (e.g. $\theta(b - R_1 - R_2)$) in a multidimensional integral [65, 66]. This method is also used in the SuperChic generator, which was used to carry out calculations regarding the analyzed processes [56, 67, 68].

Mass region	without soft GSE	with soft GSE	S_G
$0.5 - 5.0\,(\mathrm{GeV})$	755.91 (nb)	718.84 (nb)	0.95
$5.0 - 10.0\,(\mathrm{GeV})$	687.74 (nb)	623.27 (nb)	0.91
$10.0 - 15.0\,(\mathrm{GeV})$	98.68 (nb)	87.01 (nb)	0.88
$15.0 - 20.0\,(\mathrm{GeV})$	28.23 (nb)	24.33 (nb)	0.86

Table 2.5: The total cross-section for different mass regions from 0.0 to 20.0 GeV with corresponding gap survival factor S_G from the SuperChic generator.

This is particularly interesting to which extent the geometrical conditions change the dilepton invariant mass distribution. Therefore, Table 2.5 shows the results for four different invariant mass areas, the first of which includes both areas measured by ALICE and the rapidity gap survival factor which is the ratio of the above cross-sections. This is also the area where the gap survival factor has the highest value, reaching 95%. The value of this factor is quite high also for larger masses, but its significant decrease is visible as their value increases.

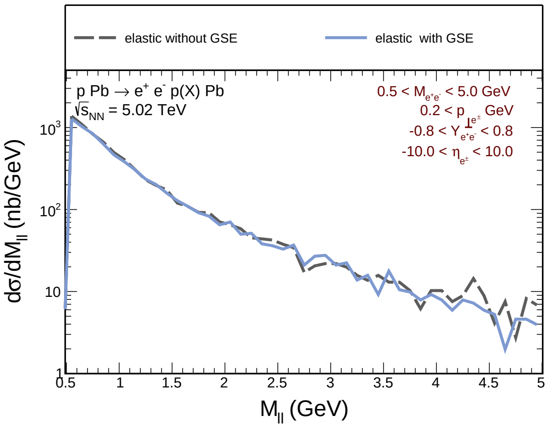

Figure 2.25: Dilepton invariant mass dependence of the cross-sections for the elastic collision for mass window $0.5 < M_{ll} < 5.0\,\mathrm{GeV}$ with (solid lines) and without (dashed lines) rapidity gap survival effects.

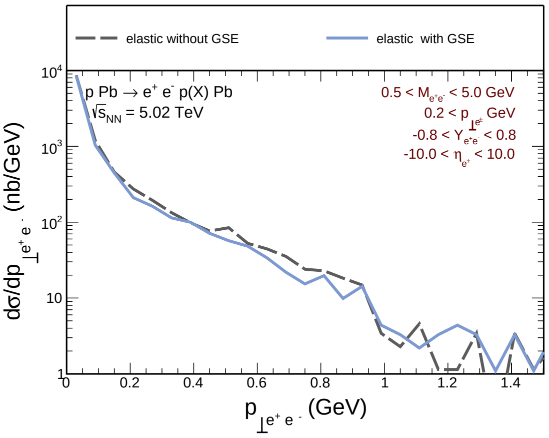

Figure 2.26: Dilepton transverse momenta dependence of the cross-sections for the elastic collision for mass window $0.5 < M_{ll} < 5.0\,\mathrm{GeV}$ with (solid lines) and without (dashed lines) rapidity gap survival effects.

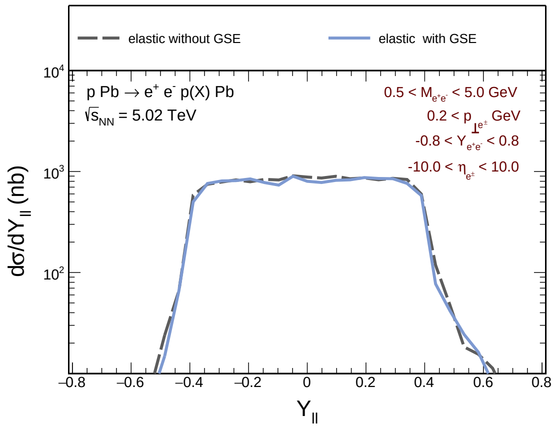

Figure 2.27: Dilepton rapidity dependence of the cross-section for the elastic collision for mass window $0.5 < M_{ll} < 5.0\,\mathrm{GeV}$ with (solid line) and without (dashed line) rapidity gap survival effects.

Chapter 3

Diffractive photoproduction of the charm quark-antiquark pairs production

3.1 Diffractive mechanism

A large amount of information about the structure of hadrons is also provided by the already mentioned diffraction processes with high transverse momentum of a produced system such as the quark-antiquark dijet [69]. An example of this process is the diffractive dissociation of photons or pions in dijet production, whose forward cross-section for large transverse momenta of the jet maps to the unintegrated gluon distributions of the target [70, 71]. Moreover, recently much attention has been paid to Wigner distributions, which are a generalization of unintegrated parton distributions to the five-dimensional quasi-probability phase space distribution [72, 73]. These distributions depend on the transverse momentum $\vec{k}_\perp$ and the impact parameter $\vec{b}_\perp$ of the proton or nucleus, taking into account the azimuthal angular relationship between these vectors. However, after fully transforming the distributions into momentum space, they are equivalent to Generalized Transverse Momentum Distributions - GTMDs (for details see [74, 75, 76]) taking into account the relation between $\vec{k}_\perp$ and $\vec{\Delta}_\perp$, which contributes to the so-called elliptic Wigner functions or elliptic GTMD [77]. See for example Fig. 1.8.

In the region of small-x for diffraction processes, the color dipole approach [78, 79] can be used, in which the dipole amplitude depends on its size $\vec{r}_\perp$ and the impact parameter $\vec{b}_\perp$ and carries information analogous to the Wigner/GTMD functions. Similarly, the dependence on the azimuthal angle is translated into a dependence on the dipole orientation taking into account the color field of the target.

It was advocated that the elliptic gluon distributions could be studied in diffractive processes, such as

- exclusive dijet production in ep collisions [80, 81]. For calculations in the color dipole approach, see [82, 83, 84];
- exclusive dijet photoproduction in pA and AA ultra-peripheral collisions (UPCs) [85];
- exclusive $Q\bar{Q}$ (with $Q = c, b$) photoproduction in pA and AA UPCs [86].

In the production of charm quarks in proton-nucleus collisions considered below, the dominant process is diffractive photoproduction of the $c\bar{c}$ pair on a proton by a Weizsäker-Williams photon emitted by the lead nucleus as in diagrams in Fig. 3.1. In this case, it is assumed that the photon flux scales with the ion charge as Z^2, which would not be the case if the photon were emitted by a proton. The integrated diffractive process on the nucleus will show a dependence $\sigma \propto A^{\alpha}$, with approximately $\alpha \sim 1.4 \div 1.5$ (see e.g. [69, 71]). Therefore, diffractive photoproduction on the nucleus can have a significant effect, and extraction of the process discussed in this analysis is possible if proton measurement [87, 88, 89] is available, due to the very sharp dependence of the electromagnetically scattered transverse momentum proton.

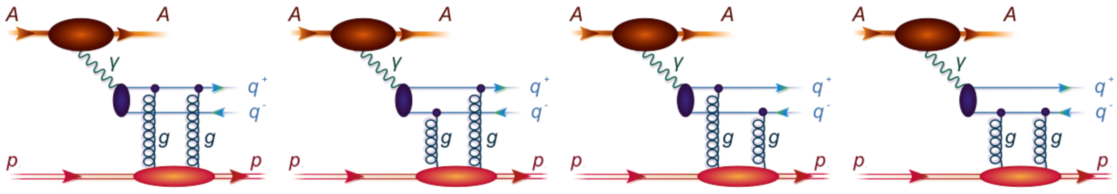

Figure 3.1: Dijet diffractive production mechanism in a proton-lead collision.

Unlike the production of light dijets, for heavy quarks, the quark mass m_Q can act as a hard scale, while intermediate and small values of $\vec{P}_\perp$ are acceptable. Moreover, although the presented results do not refer to experimental data, cases for realistic kinematic conditions at the LHC are considered, including cuts imposed on the relative transverse momentum of the dijet, which is expressed as

$$\vec{P}_\perp = \frac{1}{2}(\vec{p}_{\perp Q} - \vec{p}_{\perp \bar{Q}}), \tag{3.1}$$

and the momentum transfer to the proton corresponding to the transverse momentum of the produced dijet, which for the exclusive case fulfills:

$$\vec{\Delta}_\perp = \vec{p}_{\perp Q} + \vec{p}_{\perp \bar{Q}}, \tag{3.2}$$

while the angle between these vectors, expressed as

$$\cos\phi = \frac{\vec{P}_\perp \cdot \vec{\Delta}_\perp}{P_\perp \Delta_\perp}, \tag{3.3}$$

is the azimuthal angle related to elliptic functions, which gives rise to some subtleties. It is expected that for large $P_\perp$ the correlations in ϕ will be proportional to $\cos(2\phi)$ and uniquely expressed by the elliptic GTMD. However, for smaller $P_\perp$ the azimuthal correlations come rather from the matrix element (or impact factor) at a finite value of $\Delta_\perp$. And although formally these dependencies can be absorbed by the Wigner/GTMD functions, they correspond to the members of the δ function in the latter.

3.1.1 Kinematics

The collision cross-section for the visible in Fig. 3.1 production processes of $c\bar{c}$ pairs in proton-lead collisions is expressed as

$$\frac{d\sigma(pA \to Q\bar{Q}pA; s)}{dx_Q dx_{\bar{Q}} d^2\vec{P}_\perp d^2\vec{\Delta}_\perp} = \frac{1}{x_Q + x_{\bar{Q}}} f_{\gamma/A}(x_Q + x_{\bar{Q}}) \frac{d\sigma\big(\gamma p \to Q\bar{Q}p; (x_Q + x_{\bar{Q}})s\big)}{dz d^2\vec{P}_\perp d^2\vec{\Delta}_\perp}, \tag{3.4}$$

where $z = x_Q/(x_Q + x_{\bar{Q}})$, and $x_Q, x_{\bar{Q}}$ are the nucleus' light-front momentum fractions carried by a heavy quark and antiquark, respectively. The Weizsäcker-Williams photons carry the momentum fraction

$$x_A = x_Q + x_{\bar{Q}}. \tag{3.5}$$

The quasireal photon flux

$$f_{\gamma/A}(x_A) = \frac{dN(x_A)}{dx_A}, \tag{3.6}$$

is given by

$$\frac{dN(x_A)}{dx_A} = \frac{2Z^2\alpha_{\rm em}}{\pi x_A}\left[\xi_{jA}K_0(\xi_{jA})K_1(\xi_{jA}) - \frac{\xi_{jA}^2}{2}\Big(K_1^2(\xi_{jA}) - K_0^2(\xi_{jA})\Big)\right], \tag{3.7}$$

with the atomic number of the projectile particle Z, the fine structure constant α_{em}, $\xi_{jA} = x_A m_p(R_j + R_A)$ including the target and nucleus radius (R_j and R_A) and effectively excluding the overlap of the projectile, the target in the space of impact parameters, and the modified Bessel functions $K_0(\xi_{jA})$ and $K_1(\xi_{jA})$ described for example in Ref. [90].

The cross-section may be also written in terms of the center-of-mass rapidities $y_Q, y_{\bar{Q}}$ of quarks,

$$\frac{d\sigma(pA \to Q\bar{Q}pA; s)}{dy_Q dy_{\bar{Q}} d^2\vec{P}_\perp d^2\vec{\Delta}_\perp} = x_A \frac{dN(x_A)}{dx_A} \left(z(1-z) \frac{d\sigma(\gamma p \to Q\bar{Q}p; x_A s)}{dz d^2\vec{P}_\perp d^2\vec{\Delta}_\perp} \right) \Bigg|_{z=\frac{x_Q}{x_A}}, \tag{3.8}$$

where

$$x_Q = \frac{\sqrt{p_{\perp Q}^2 + m_Q^2}}{s} \exp(y_Q), \qquad x_{\bar{Q}} = \sqrt{\frac{p_{\perp \bar{Q}}^2 + m_Q^2}{s}} \exp(y_{\bar{Q}}) \, . \tag{3.9}$$

Furthermore, the transverse momenta of the produced particles are the following:

$$\vec{p}_{\perp Q} = \vec{P}_\perp + \frac{\vec{\Delta}_\perp}{2}, \qquad \vec{p}_{\perp \bar{Q}} = -\vec{P}_\perp + \frac{\vec{\Delta}_\perp}{2}, \tag{3.10}$$

respectively, while the transverse mass of the $c\bar{c}$ is given by

$$M_\perp^2 = x_A \left(\frac{p_{\perp Q}^2 + m_Q^2}{x_Q} + \frac{p_{\perp \bar{Q}}^2 + m_Q^2}{x_{\bar{Q}}} \right). \tag{3.11}$$

The rapidity of the $q\bar{q}$-system in the center-of-mass frame has then the following form

$$Y_{\text{pair}} = \frac{1}{2} \ln \left(\frac{x_A}{x_B} \right) = \ln \left(\frac{x_A \sqrt{s}}{M_\perp} \right), \qquad x_A x_B s = M_\perp^2, \tag{3.12}$$

while in the laboratory frame rapidities are obtained from the shift

$$y_{Q,\bar{Q}}^{\text{LAB}} = y_{Q,\bar{Q}} + \frac{1}{2} \ln \left(\frac{Z}{A} \right), \quad Y_{\text{pair}}^{\text{LAB}} = Y_{\text{pair}} + \frac{1}{2} \ln \left(\frac{Z}{A} \right), \tag{3.13}$$

where for the ^{208}Pb nucleus, $A = 208$ and $Z = 82$.

3.1.2 Color dipole representation of the diffractive amplitude

In the dipole approach to diffractive processes, the cross-section for the $\gamma p \to Q\bar{Q}$ has the following form (see for example the textbook [91])

$$\begin{aligned}\frac{d\sigma(\gamma p \to Q\bar{Q}p; s_{\gamma p})}{dz d^2\vec{P}_\perp d^2\vec{\Delta}_\perp} &= \sum_{\lambda_\gamma,\lambda,\bar{\lambda}} \Bigg| \int \frac{d^2\vec{b}_\perp d^2\vec{r}_\perp}{(2\pi)^2} e^{-i\vec{\Delta}_\perp\cdot\vec{b}_\perp} e^{-i\vec{P}_\perp\cdot\vec{r}_\perp} \\ &\times \; N(Y,\vec{r}_\perp,\vec{b}_\perp)\, \Psi^{\lambda_\gamma}_{\lambda\bar{\lambda}}(z,\vec{r}_\perp) \Bigg|^2 , \end{aligned} \tag{3.14}$$

with the corresponding light-front wave function for the $\gamma \to Q\bar{Q}$ depending on the light-front helicities of quarks $\lambda/2, \bar{\lambda}/2$, and photon helicity λ_γ, respectively:

$$\Psi^{\lambda_\gamma}_{\lambda\bar{\lambda}}(z,\vec{r}_\perp) = \frac{1}{\sqrt{4\pi z(1-z)}} \int \frac{d^2\vec{l}_\perp}{(2\pi)^2} e^{i\vec{r}_\perp\cdot\vec{l}_\perp} \Psi^{\lambda_\gamma}_{\lambda\bar{\lambda}}(z,\vec{l}_\perp) . \tag{3.15}$$

Its explicit form in transverse momentum space can be found, for example, in Ref. [91].

More interesting is the dipole amplitude $N(Y,\vec{r}_\perp,\vec{b}_\perp)$, the energy of which is related to the "rapidity" Y defined as $Y = \ln(x_0/x_{\mathbb{P}})$. In this dependence $x_0 = 0.01$, while

$$x_{\mathbb{P}} \equiv x_B = \frac{M_\perp^2}{s_{\gamma p}} = \frac{M_\perp^2}{x_A s} , \tag{3.16}$$

where $M_\perp$ is the $Q\bar{Q}$ system transverse mass. This amplitude is related to an off-diagonal generalization of the unintegrated gluon distribution, namely a gluon density matrix as follows

$$\begin{aligned} N(Y,\vec{r}_\perp,\vec{b}_\perp) &= \int d^2\vec{q}_\perp d^2\vec{k}_\perp\, f\Big(Y, \frac{\vec{q}_\perp}{2}+\vec{k}_\perp, \frac{\vec{q}_\perp}{2}-\vec{k}_\perp\Big) \exp[i\vec{q}_\perp\cdot\vec{b}_\perp] \\ &\times \Bigg\{ \exp\Big[i\frac{1}{2}\vec{q}_\perp\cdot\vec{r}_\perp\Big] + \exp\Big[-i\frac{1}{2}\vec{q}_\perp\cdot\vec{r}_\perp\Big] \\ &- \exp\Big[i\vec{k}_\perp\cdot\vec{r}_\perp\Big] - \exp\Big[-i\vec{k}_\perp\cdot\vec{r}_\perp\Big] \Bigg\} . \end{aligned} \tag{3.17}$$

It is also related to the familiar color dipole cross-section (see e.g. Ref. [92]) by the following integration:

$$\sigma(x_{\mathbb{P}},\vec{r}_\perp) = 2\int d^2\vec{b}_\perp\, N(Y,\vec{r}_\perp,\vec{b}_\perp) . \tag{3.18}$$

In this approach, the quark and antiquark move corresponds to the impact parameters, as follows:

$$\vec{b}_{\perp Q} = \vec{b}_\perp + \frac{\vec{r}_\perp}{2} , \qquad \vec{b}_{\perp\bar{Q}} = \vec{b}_\perp - \frac{\vec{r}_\perp}{2} , \tag{3.19}$$

which maps the four space factors in Eq. (3.17) in round brackets, and connects them to the four diagrams in Fig. 3.1. The unintegrated gluon density matrix appearing in this equation can be written as

$$f\Big(Y, \frac{\vec{q}_\perp}{2} + \vec{k}_\perp, \frac{\vec{q}_\perp}{2} - \vec{k}_\perp\Big) = \frac{\alpha_s}{4\pi N_c} \frac{\mathcal{F}\Big(x_{\mathbb{P}}, \frac{\vec{q}_\perp}{2} + \vec{k}_\perp, \frac{\vec{q}_\perp}{2} - \vec{k}_\perp\Big)}{(\frac{\vec{q}_\perp}{2} + \vec{k}_\perp)^2 \Big(\frac{\vec{q}_\perp}{2} - \vec{k}_\perp\Big)^2}\,, \tag{3.20}$$

where $N_c = 3$ number of the colors in QCD, including the strong coupling constant α_s, and gluon propagators.

Therefore, by integrating the gluon density matrix from the Eq. (3.17) by $\vec{b}_\perp$, the well-known representation of the dipole cross-section is obtained [93], and has the following form:

$$\sigma(x_{\mathbb{P}}, \vec{r}_\perp) = \frac{2\pi}{N_c} \int \frac{d^2\vec{k}_\perp}{k_\perp^4} \alpha_s \mathcal{F}(x_{\mathbb{P}}, \vec{k}_\perp, -\vec{k}_\perp) \Big\{ 2 - e^{i\vec{k}_\perp \cdot \vec{r}_\perp} - e^{-i\vec{k}_\perp \cdot \vec{r}_\perp} \Big\}\,, \tag{3.21}$$

which proves, that $\mathcal{F}(x, \vec{k}_{\perp 1}, \vec{k}_{\perp 2})$ is the proper off-forward generalization of the standard unintegrated gluon distribution. Moreover, it is related to its collinear counterpart as

$$xg(x, \mu^2) = \int \frac{d^2\vec{k}_\perp}{\pi k_\perp^2} \, \theta(\mu^2 - k_\perp^2) \, \mathcal{F}(x, \vec{k}_\perp, -\vec{k}_\perp)\,. \tag{3.22}$$

There is also the non-perturbative parameter that has an interpretation of the dipole cross-section for the large dipoles:

$$\sigma_0(x_{\mathbb{P}}) = \frac{4\pi}{N_c} \int \frac{d^2\vec{k}_\perp}{k_\perp^4} \alpha_s \mathcal{F}(x_{\mathbb{P}}, \vec{k}_\perp, -\vec{k}_\perp)\,. \tag{3.23}$$

Incorporating the representation of the dipole amplitude from Eq. (3.17) into Eq. (3.14) allows the diffractive amplitude to be represented in a convolution form (the exact calculation are given in Appendix A)

$$\begin{aligned} \mathcal{A}(Y, \vec{P}_\perp, \vec{\Delta}_\perp) \;&\propto\; \int d^2\vec{k}_\perp \, f\Big(Y, \frac{\vec{\Delta}_\perp}{2} + \vec{k}_\perp, \frac{\vec{\Delta}_\perp}{2} - \vec{k}_\perp\Big) \\ &\times\; \Big\{ \Psi^{\lambda_\gamma}_{\lambda\bar{\lambda}}\Big(z, \vec{P}_\perp + \frac{\vec{\Delta}_\perp}{2}\Big) + \Psi^{\lambda_\gamma}_{\lambda\bar{\lambda}}\Big(z, \vec{P}_\perp - \frac{\vec{\Delta}_\perp}{2}\Big) \\ &-\; \Psi^{\lambda_\gamma}_{\lambda\bar{\lambda}}(z, \vec{P}_\perp + \vec{k}_\perp) - \Psi^{\lambda_\gamma}_{\lambda\bar{\lambda}}(z, \vec{P}_\perp - \vec{k}_\perp) \Big\}\,. \end{aligned} \tag{3.24}$$

In that equation, the t-channel gluons from curly brackets carry the following transverse momenta,

$$\vec{k}_{\perp 1} = \frac{\vec{\Delta}_\perp}{2} + \vec{k}_\perp\,, \quad \vec{k}_{\perp 2} = \frac{\vec{\Delta}_\perp}{2} - \vec{k}_\perp\,, \tag{3.25}$$

while the impact factor vanishes when either of the transverse momenta of the gluons goes to zero, i.e. for $\vec{k}_\perp = \pm\vec{\Delta}_\perp/2$.

Each of the Ψ functions seen in Eq. 3.24 therefore, corresponds to a different case of gluon exchange, as shown in Fig. 3.2.

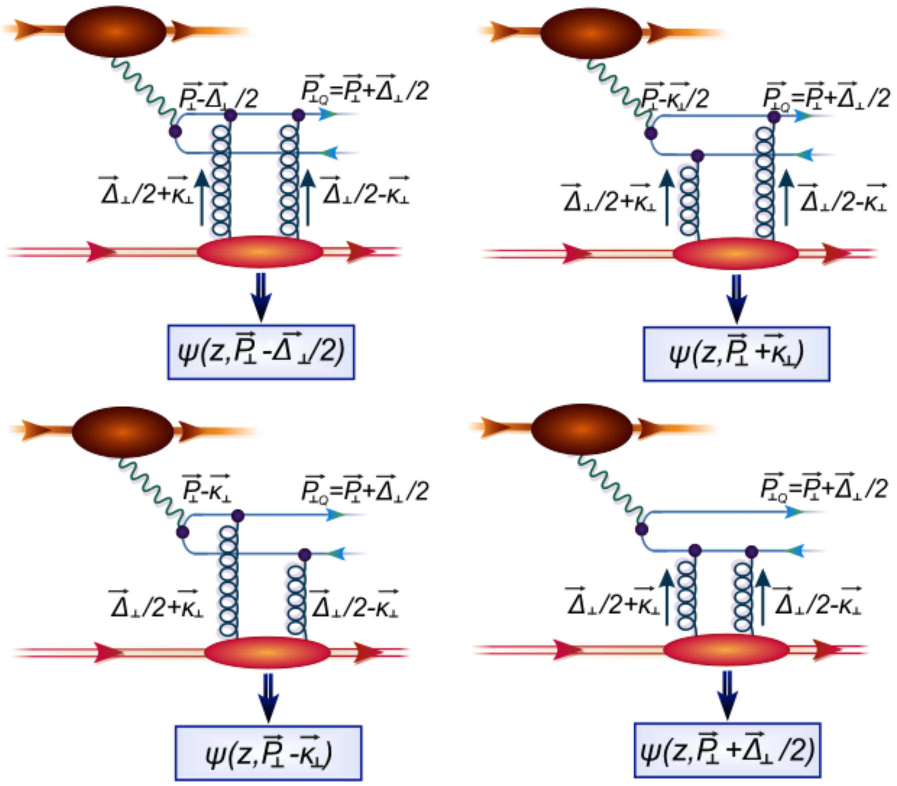

Figure 3.2: Four cases of gluon exchange concerning the carried momenta and the corresponding light-front wave functions.

The above-mentioned light-front wave functions according to Ref. [91] include only the dependence on the transverse momenta:

$$\begin{aligned}\Psi_T^{\gamma^*\to q\bar{q}}(k_\perp,z) &= e\,e_f\sqrt{z(1-z)}\delta_{ij}\\ &\times \frac{(1-\delta_{\sigma\sigma'})\vec{\epsilon}^{\,\lambda}_\perp\cdot\vec{k}_\perp(1-2z-\sigma\lambda)+\delta_{\sigma\sigma'}m_f(1+\sigma\lambda)/\sqrt{2}}{\vec{k}^2_\perp+m_f^2+Q^2z(1-z)}, \qquad (3.26)\end{aligned}$$

where $\sigma/2, \sigma^{'}/2$ corresponds to the appropriate quark helicity, λ corresponds to the photon helicity, e is the elementary charge, while $\epsilon_\perp$ is the photon factorization vector.

Due to the fact, that the considered quasi-real photons do not have a longitudinal polarization, only the transverse term of the wave function is taken into account. However, two cases should be distinguished, first in which the helicities of quarks have opposite values ($S_z = \frac{\sigma}{2} + \frac{\sigma^{'}}{2} = 0$), and second in which $S_z = \frac{\sigma}{2} + \frac{\sigma^{'}}{2} = \pm 1$ and the quark helicities are parallel.

Finally, the diffractive photoproduction cross-section takes the following form:

$$\frac{d\sigma(\gamma p \to Q\bar{Q}p; s_{\gamma p})}{dz d^2\vec{P}_\perp d^2\vec{\Delta}_\perp} = e_f^2 \alpha_{\rm em} 2N_c (2\pi)^2 \Big\{ \big(z^2 + (1-z)^2\big) \big|\vec{\mathcal{M}}_0\big|^2 + m_Q^2 \big|\mathcal{M}_1\big|^2 \Big\}. \tag{3.27}$$

with amplitudes for the sum of the quark helicities equal zero, for $\vec{\mathcal{M}}_0$, and equal one for $\mathcal{M}_1$, respectively. Those amplitudes take the following form (for details see e.g. Refs [91, 94]):

$$\begin{aligned}
\vec{\mathcal{M}}_0(\vec{P}_\perp, \vec{\Delta}_\perp) &= \int \frac{d^2\vec{k}_\perp}{2\pi} f\Big(Y, \frac{\vec{\Delta}_\perp}{2} + \vec{k}_\perp, \frac{\vec{\Delta}_\perp}{2} - \vec{k}_\perp\Big) \\
&\times \left\{ \frac{\vec{P}_\perp - \vec{\Delta}_\perp/2}{(\vec{P}_\perp - \vec{\Delta}_\perp/2)^2 + m_Q^2} + \frac{\vec{P}_\perp + \vec{\Delta}_\perp/2}{(\vec{P}_\perp + \vec{\Delta}_\perp/2)^2 + m_Q^2} \right. \\
&- \left. \frac{\vec{P}_\perp - \vec{k}_\perp}{(\vec{P}_\perp - \vec{k}_\perp)^2 + m_Q^2} - \frac{\vec{P}_\perp + \vec{k}_\perp}{(\vec{P}_\perp + \vec{k}_\perp)^2 + m_Q^2} \right\}, \\
\mathcal{M}_1(\vec{P}_\perp, \vec{\Delta}_\perp) &= \int \frac{d^2\vec{k}_\perp}{2\pi} f\Big(Y, \frac{\vec{\Delta}_\perp}{2} + \vec{k}_\perp, \frac{\vec{\Delta}_\perp}{2} - \vec{k}_\perp\Big) \\
&\times \left\{ \frac{1}{(\vec{P}_\perp - \vec{\Delta}_\perp/2)^2 + m_Q^2} + \frac{1}{(\vec{P}_\perp + \vec{\Delta}_\perp/2)^2 + m_Q^2} \right. \\
&- \left. \frac{1}{(\vec{P}_\perp - \vec{k}_\perp)^2 + m_Q^2} - \frac{1}{(\vec{P}_\perp + \vec{k}_\perp)^2 + m_Q^2} \right\}.
\end{aligned} \tag{3.28}$$

To better understand the origin of the azimuthal correlation, it is worth decomposing the amplitude and writing the matrix elements as

$$\begin{aligned}
\vec{\mathcal{M}}_0(\vec{P}_\perp, \vec{\Delta}_\perp) &= \vec{\mathcal{J}}_0(\vec{P}_\perp, 1/2\vec{\Delta}_\perp)\, C(Y, \vec{\Delta}_\perp) \\
&- \int \frac{d^2\vec{k}_\perp}{2\pi} \vec{\mathcal{J}}_0(\vec{P}_\perp, \vec{k}_\perp)\, f\Big(Y, \frac{\vec{\Delta}_\perp}{2} + \vec{k}_\perp, \frac{\vec{\Delta}_\perp}{2} - \vec{k}_\perp\Big), \\
\mathcal{M}_1(\vec{P}_\perp, \vec{\Delta}_\perp) &= \mathcal{J}_1(\vec{P}_\perp, 1/2\vec{\Delta}_\perp)\, C(Y, \vec{\Delta}_\perp) \\
&- \int \frac{d^2\vec{k}_\perp}{2\pi} \mathcal{J}_1(\vec{P}_\perp, \vec{k}_\perp)\, f\Big(Y, \frac{\vec{\Delta}_\perp}{2} + \vec{k}_\perp, \frac{\vec{\Delta}_\perp}{2} - \vec{k}_\perp\Big).
\end{aligned} \tag{3.29}$$

with

$$\begin{aligned}
\mathcal{J}_0(\vec{P}_\perp, \vec{q}_\perp) &= \frac{\vec{P}_\perp - \vec{q}_\perp}{(\vec{P}_\perp - \vec{q}_\perp)^2 + m_Q^2} + \frac{\vec{P}_\perp + \vec{q}_\perp}{(\vec{P}_\perp + \vec{q}_\perp)^2 + m_Q^2} - \frac{2\vec{P}_\perp}{\vec{P}_\perp^2 + m_Q^2}, \\
\mathcal{J}_1(\vec{P}_\perp, \vec{q}_\perp) &= \frac{1}{(\vec{P}_\perp - \vec{q}_\perp)^2 + m_Q^2} + \frac{1}{(\vec{P}_\perp + \vec{q}_\perp)^2 + m_Q^2} - \frac{2}{\vec{P}_\perp^2 + m_Q^2}. \qquad (3.30)
\end{aligned}$$

and the rapidity-dependent form factor:

$$C(Y, \vec{\Delta}_\perp) = \int \frac{d^2\vec{k}_\perp}{2\pi} f\Big(Y, \frac{\vec{\Delta}_\perp}{2} + \vec{k}_\perp, \frac{\vec{\Delta}_\perp}{2} - \vec{k}_\perp\Big), \qquad (3.31)$$

that is a non-perturbative parameter, as is obvious from its form in the forward limit as an integral, that converges at soft, non-perturbative values of $k_\perp$:

$$C(Y, 0) = \frac{1}{4\pi N_c} \int \frac{d^2\vec{k}_\perp}{2\pi k_\perp^4} \alpha_s \mathcal{F}(x_{\mathbb{P}}, \vec{k}_\perp, -\vec{k}_\perp). \qquad (3.32)$$

It shows that it is directly proportional to the dipole cross-section for the large dipoles $\sigma_0(x_{\mathbb{P}})$ as can be seen in Eq. (3.23).

3.1.3 GTMD representation

Different momentum space representations of the diffractive amplitude are available in the literature, whose are the Fourier transforms of the dipole amplitude (see e.g. Refs [85, 86, 95]). Using the normalization and notation of Ref. [86] it can be expressed as

$$T(Y, \vec{k}_\perp, \vec{\Delta}_\perp) = \int \frac{d^2\vec{b}_\perp}{(2\pi)^2} \frac{d^2\vec{r}_\perp}{(2\pi)^2} e^{-i\vec{\Delta}_\perp \cdot \vec{b}_\perp} e^{-i\vec{k}_\perp \cdot \vec{r}_\perp} N(Y, \vec{r}_\perp, \vec{b}_\perp). \qquad (3.33)$$

This formula is often referred to as the Generalized Transverse Momentum Distribution (GTMD) of gluons in the proton target. However to show the relation between dipole amplitude and gluon density matrix $f\Big(Y, \frac{\vec{q}_\perp}{2} + \vec{k}_\perp, \frac{\vec{q}_\perp}{2} - \vec{k}_\perp\Big)$ which encodes the same information it is necessary to perform the Fourier transform by inserting Eq. (3.17) into Eq. (3.33), which yields

$$\begin{aligned}
T(Y, \vec{k}_\perp, \vec{\Delta}_\perp) &= C(Y, \vec{\Delta}_\perp)\Big(\delta^{(2)}(\vec{k}_\perp - \vec{\Delta}_\perp/2) + \delta^{(2)}(\vec{k}_\perp + \vec{\Delta}_\perp/2)\Big) \\
&- f\Big(Y, \vec{\Delta}_\perp/2 + \vec{k}_\perp, \vec{\Delta}_\perp/2 - \vec{k}_\perp\Big) \\
&- f\Big(Y, \vec{\Delta}_\perp/2 - \vec{k}_\perp, \vec{\Delta}_\perp/2 + \vec{k}_\perp\Big), \qquad (3.34)
\end{aligned}$$

where $C(Y, \vec{\Delta}_\perp)$ of Eq. (3.31) multiplies a combination of δ-functions.

There is a visible agreement between both distributions up to the term containing δ-functions which, however, is not significant when convoluted with the impact factor from Eq. (3.24). Formally, it could then be written:

$$f\Big(Y, \vec{\Delta}_\perp/2 + \vec{k}_\perp, \vec{\Delta}_\perp/2 - \vec{k}_\perp\Big) \to -\frac{1}{2}\, T(Y, \vec{k}_\perp, \vec{\Delta}_\perp)\,. \tag{3.35}$$

The implication of this equation for numerical applications turns out to be problematic because in diffraction interactions the values of $\Delta_\perp$ are limited by the diffraction slope B_D. Therefore, for large values of $k_\perp$ the δ-functions are irrelevant, and the two gluon distributions, f and T, are equal to each other up to a factor of $1/2$. A consequence of this is the sum rule

$$\int d^2\vec{k}_\perp\, T(Y, \vec{k}_\perp, \vec{\Delta}_\perp) = 0\,, \tag{3.36}$$

which shows that $N(Y, \vec{r}_\perp, \vec{b}_\perp) \to 0$ for $r_\perp \to 0$. Therefore, the Fourier transform from the Eq. 3.33 is a non-convergent integral, and does not exist as a function, as evidenced by the presence of δ-function terms in Eq. (3.34). Regularizing the Fourier transform is most often done by inserting a Gaussian cutoff function [85, 86, 95]:

$$T(Y, \vec{k}_\perp, \vec{\Delta}_\perp) = \int \frac{d^2\vec{b}_\perp}{(2\pi)^2} \frac{d^2\vec{r}_\perp}{(2\pi)^2} e^{-i\vec{\Delta}_\perp\cdot\vec{b}_\perp} e^{-i\vec{k}_\perp\cdot\vec{r}_\perp}\, N(Y, \vec{r}_\perp, \vec{b}_\perp)\, e^{-\varepsilon r_\perp^2}\,. \tag{3.37}$$

Inserting this representation into Eq. (3.17) yields a cutoff-dependent T as

$$\begin{aligned} T(Y, \vec{k}_\perp, \vec{\Delta}_\perp) \;&=\; C(Y, \vec{\Delta}_\perp)\Big(\delta^{(2)}_\varepsilon(\vec{k}_\perp - \vec{\Delta}_\perp/2) + \delta^{(2)}_\varepsilon(\vec{k}_\perp + \vec{\Delta}_\perp/2)\Big) \\ &\quad - f_\varepsilon\Big(Y, \vec{\Delta}_\perp/2 + \vec{k}_\perp, \vec{\Delta}_\perp/2 - \vec{k}_\perp\Big) \\ &\quad - f_\varepsilon\Big(Y, \vec{\Delta}_\perp/2 - \vec{k}_\perp, \vec{\Delta}_\perp/2 + \vec{k}_\perp\Big)\,, \end{aligned} \tag{3.38}$$

with a "smeared-out" delta distribution

$$\delta^{(2)}_\varepsilon(\vec{k}_\perp) = \frac{1}{4\pi\varepsilon}\, \exp\Big(-\frac{k_\perp^2}{4\varepsilon}\Big)\,, \tag{3.39}$$

and a "smeared-out" version of the gluon density matrix

$$\begin{aligned} f_\varepsilon\Big(Y, \vec{\Delta}_\perp/2 - \vec{k}_\perp, \vec{\Delta}_\perp/2 + \vec{k}_\perp\Big) \;&=\; \int d^2\vec{\kappa}_\perp\, f\Big(Y, \vec{\Delta}_\perp/2 - \vec{\kappa}_\perp, \vec{\Delta}_\perp/2 + \vec{\kappa}_\perp\Big) \\ &\quad\times\; \delta^{(2)}_\varepsilon(\vec{k}_\perp - \vec{\kappa}_\perp). \end{aligned} \tag{3.40}$$

The regularized T-matrix also fulfills the sum rule from Eq. (3.36).

Finally, the matrix elements $\vec{\mathcal{M}}_0$ and $\mathcal{M}_1$ depending on T are written as follows

$$\begin{aligned}\vec{\mathcal{M}}_0 &= \int \frac{d^2\vec{k}_\perp}{2\pi} T(Y,\vec{k}_\perp,\vec{\Delta}_\perp) \left\{ \frac{\vec{P}_\perp - \vec{k}_\perp}{(\vec{P}_\perp - \vec{k}_\perp)^2 + m_Q^2} - \frac{\vec{P}_\perp}{\vec{P}_\perp^2 + m_Q^2} \right\}, \\ \mathcal{M}_1 &= \int \frac{d^2\vec{k}_\perp}{2\pi} T(Y,\vec{k}_\perp,\vec{\Delta}_\perp) \left\{ \frac{1}{(\vec{P}_\perp - \vec{k}_\perp)^2 + m_Q^2} - \frac{1}{\vec{P}_\perp^2 + m_Q^2} \right\}. \end{aligned} \tag{3.41}$$

Notice, that in effect here the impact factor for forward scattering is used, and all dependence on $\vec{\Delta}_\perp$ has been absorbed into the GTMD $T(Y, \vec{k}_\perp, \vec{\Delta}_\perp)$.

3.1.4 Parametrizations of the GTMDs

As both previously presented approaches are used in the literature, five different models, corresponding to both of them, were used in the analysis. The first two refer to the off-forward gluon density matrix f of Eq. (3.20), which can be also written as (see Refs [96], [97]):

$$f\Big(Y, \frac{\vec{\Delta}_\perp}{2} + \vec{k}_\perp, \frac{\vec{\Delta}_\perp}{2} - \vec{k}_\perp\Big) = \frac{\alpha_s}{4\pi N_c} \frac{\mathcal{F}(x_{\mathbb{P}}, \vec{k}_\perp, -\vec{k}_\perp)}{k_\perp^4} \exp\Big[-\frac{1}{2} B\vec{\Delta}^2 \Big], \tag{3.42}$$

used diffractive slope $B = 4\,\mathrm{GeV}^{-2}$. The diagonal unintegrated gluon distribution $\mathcal{F}$ was taken from two different approaches: the Golec-Biernat–Wüsthoff (GBW) model [98], and the Moriggi-Peccini-Machado (MPM) parametrization [99].

The other three models are based on the regularized Fourier transform of the dipole amplitudes, as in the Eq. (3.37). The first one is based on the numerical solution of the Balitsky-Kovchegov equation for the dipole matrix S with the impact parameter dependence [100, 101], and is described in Refs [95]. Such solutions were also obtained, among others, in Ref. [102, 103, 104]. However, in this work it was decided to use the normalization from Ref. [95], which is based on the use of symmetry first observed in [105]. This model is hereinafter referred to as HHU.

The second model is based on the original effective McLerran-Venugopalan parametrization from Ref. [106] and has been generalized for the proton target and extended to take into account heterogeneities in the gluon distribution in the transverse plane in Ref. [107]. It has been applied to the exclusive photoproduction of diffractive light and heavy quarks in Refs. [85] and [86], respectively. In this analysis, it will be called the MV-IR model. The parametrization used in this case, unlike the HHU model, is independent of $x_{\mathbb{P}}$ (see Ref. [107]). Therefore, to obtain semi-realistic results, an additional modification

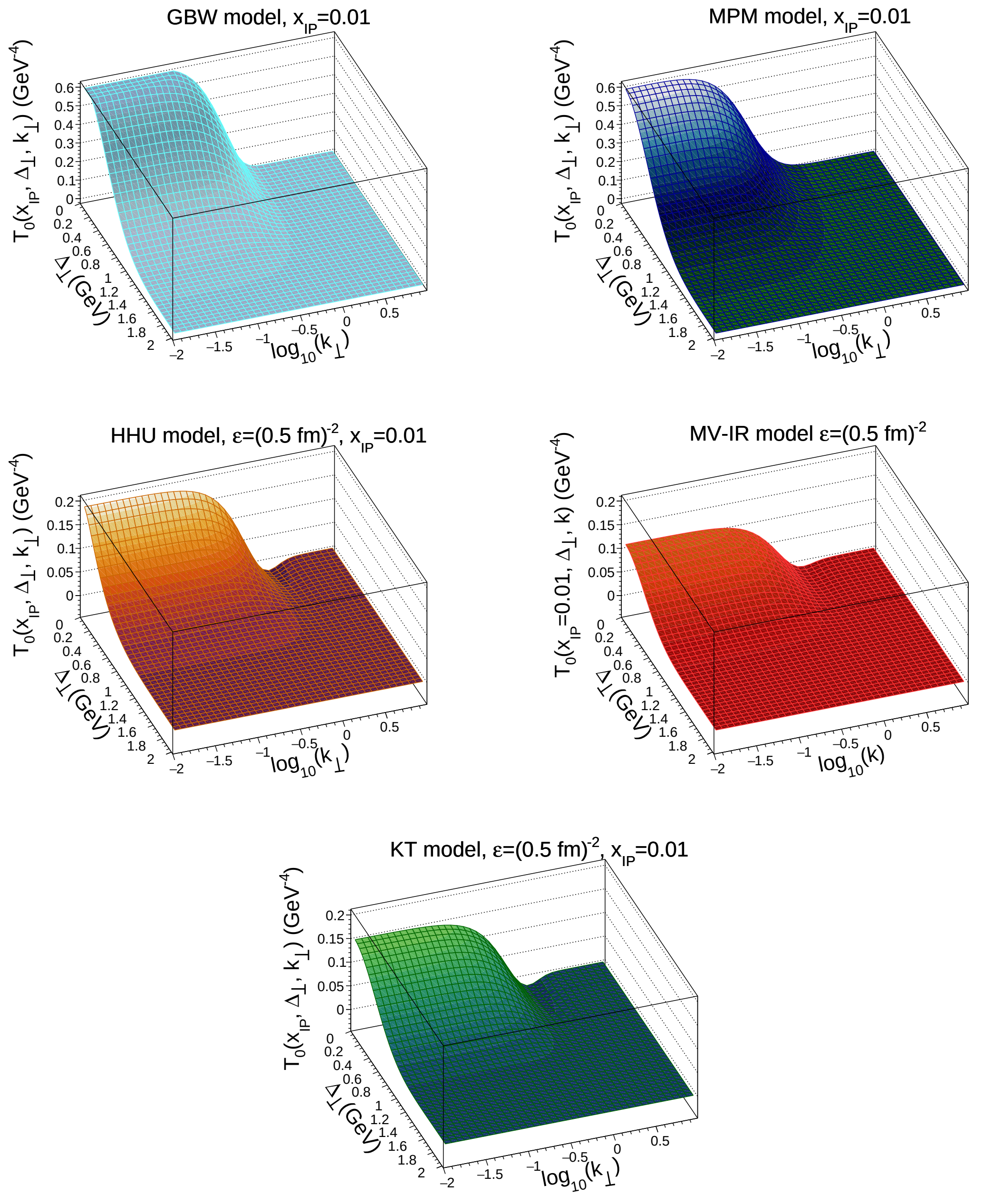

GBW model, x_{IP}=0.01

MPM model, x_{IP}=0.01

HHU model, ε=(0.5 fm)$^{-2}$, x_{IP}=0.01

MV-IR model ε=(0.5 fm)$^{-2}$

KT model, ε=(0.5 fm)$^{-2}$, x_{IP}=0.01

Figure 3.3: Different parametrizations of the GTMD depending on the $\Delta_\perp$ and $\log_{10}(k_\perp)$.

was used, that also took into account the $\lambda = 0.277$ parameter:

$$T^{\rm mod}_{\rm MV-IR}(Y, \vec{k}_\perp, \vec{\Delta}_\perp) = T_{\rm MV-IR}(\vec{k}_\perp, \vec{\Delta}_\perp)\, e^{\lambda Y}, \qquad Y = \ln\left(\frac{0.01}{x_{\mathbb{P}}}\right) . \tag{3.43}$$

It should be mentioned, however, that there are more realistic versions of the model proposed by L. McLerran and R. Venugopalan, such as the one in Ref. [108].

The last parametrization considered is the so-called Kowalski and Teaney's bSat model [109]. It has been adapted to the given proton structure functions and therefore gives a relatively realistic dipole amplitude but it does not take into account the effects of dipole orientation, unlike the HHU and MV-IR models. However, the last two are rather toy models in the context of data description. For the distribution of gluons in this model, hereinafter referred to as KT, the parameters from Table I fit 3 from Ref. [109] are used.

The dependence on the dipole orientation characteristic of the HHU and MV-IR models is quantified by the elliptical part N_ϵ of the dipole amplitude in the Fourier expansion,

$$N(Y,\vec{r}_\perp,\vec{b}_\perp) = N_0(Y,r_\perp,b_\perp) + 2\,\cos(2\phi_{br})\,N_\epsilon(Y,r_\perp,b_\perp) + \dots\,. \tag{3.44}$$

therefore, the isotropic and elliptical parts of the dipole amplitude to GTMD are translated using the appropriate Fourier-Bessel transforms of both amplitude terms [80, 85, 86]:

$$\begin{aligned} T_0(Y,k_\perp,\Delta_\perp) &= \frac{1}{4\pi^2}\int_0^\infty b_\perp db_\perp J_0(\Delta_\perp b_\perp)\int_0^\infty r_\perp dr_\perp J_0(k_\perp r_\perp) \\ &\times\ N_0(Y,r_\perp,b_\perp)e^{-\varepsilon r_\perp^2}, \\ T_\epsilon(Y,k_\perp,\Delta_\perp) &= \frac{1}{4\pi^2}\int_0^\infty b_\perp db_\perp J_2(\Delta_\perp b_\perp)\int_0^\infty r_\perp dr_\perp J_2(k_\perp r_\perp) \\ &\times\ N_\epsilon(Y,r_\perp,b_\perp)e^{-\varepsilon r_\perp^2}\,. \end{aligned} \tag{3.45}$$

The exact form of the elliptical glue matrix element for any quark mass m_Q is available in Ref. [86], and its abbreviated derivation is provided in Appendix B.

It is also interesting to note that gluon density matrices, constructed as prescribed by equation (3.42), also lead to dipole amplitudes that depend on dipole orientation. This dependence is made particularly apparent by plugging the expression of equation (3.42) into equation (3.17), the results of which are:

$$\begin{aligned} N(Y,\vec{r}_\perp,\vec{b}_\perp) &= \frac{1}{4}\Big\{t_N\Big(\vec{b}_\perp + \frac{\vec{r}_\perp}{2}\Big) + t_N\Big(\vec{b}_\perp - \frac{\vec{r}_\perp}{2}\Big) - 2t_N(\vec{b}_\perp)\Big\}\sigma_0(x_{\mathbb{P}}) \\ &+\frac{1}{2}t_N(\vec{b}_\perp)\sigma(x_{\mathbb{P}},\vec{r}_\perp)\,, \end{aligned} \tag{3.46}$$

with

$$t_N(\vec{b}_\perp) = \int \frac{d^2\vec{q}_\perp}{(2\pi)^2}\,\exp(-i\vec{q}_\perp\cdot\vec{b}_\perp)\exp\Big[-\frac{1}{2}Bq_\perp^2\Big]\,. \tag{3.47}$$

Again, it can be seen that the dipole orientation dependence appears together with the non-perturbative parameter σ_0 – the dipole cross-section for large dipoles.

It is important to emphasize that although there is a correlation between $\vec{r}_\perp$ and $\vec{b}_\perp$, the Eq. (3.42) does not contain any correlation between $\vec{k}_\perp$ and $\vec{\Delta}_\perp$. This correlation is related to simple geometric relations. It distinguishes the share of diagrams in which only a quark or an antiquark interacts and probes the density of matter with appropriate collision parameters. However, there is no obvious way to construct a of-forward glue, that would lead to a completely isotropic dipole amplitude. The only way is to keep the dipole sizes small enough so that the density of matter is constant at distances $\sim r_\perp$. In such a situation, the shifts in the brackets do not matter, and only the last term in the Eq. (3.46) has a real impact. One can, of course, expect that the Eq. (3.20) will have non-trivial azimuthal correlations between $\vec{k}_\perp$ and $\vec{\Delta}_\perp$, and the dipole amplitude will have a truly dynamic elliptical element, that can also contribute into large transverse momenta $\vec{P}_\perp$.

The distributions of the above GTMD models in the $\Delta_\perp$ and $\log_{10}(k_\perp)$ functions are shown in Fig. 3.3. It is worth noting that due to the large differences in the achieved values of the dipole-nucleon amplitude $T_0(Y, \vec{k}_\perp, \vec{\Delta}_\perp)$, there are different scales on the vertical axis. Also visible in this figure is that GTMD models based on the Fourier Transform of Eq. (3.45) go into negative values at small $\Delta_\perp$ and $log_{10}(k_\perp) \sim 0.0$. These GTMDs were also presented as a function of $k_\perp$ with $\Delta_\perp = 0.01\,\mathrm{GeV}$ and two different values of $x_{\mathbb{P}}$ in Fig. 3.4. These figures clearly show that with the tested values of $\Delta_\perp$, the GBW models and MPM dominates in the region of small $k_\perp$ for $x_{\mathbb{P}} = 0.01$, while the distributions of the other three models are characterized by similar in shape but much smaller values of the amplitudes $T_0(k_\perp)$. The situation is reversed for small $x_{\mathbb{P}}$, where not only a significant decrease in the importance of the GBW and MPM models, but also very large differences in the values of the HHU, MV-IR, and KT models can be observed. In both $x_{\mathbb{P}}$ ranges, it is also clearly visible that with k close to $1.2\,\mathrm{GeV}$, the values of these models go below zero.

The parameter of the Gaussian cutoff function ε used in Eq. (3.45) is also a very interesting and important aspect. As mentioned above, similarly to the literature (see e.g. [81, 86]), it was decided to choose $\varepsilon = \ (0.5\,\mathrm{fm})^{-2}$. However, due to the lack of reference of these models to experimental data, there is no certainty as to the correctness of the selected value of this parameter. This value, however, has a huge impact on the final form of the GTMD, which is shown in Fig. 3.5. This figure shows the distributions of the MV-IR model in a form independent of $x_{\mathbb{P}}$ for several selected values of ε, for both the isotropic and elliptical contributions, which illustrates an almost linear increase in the

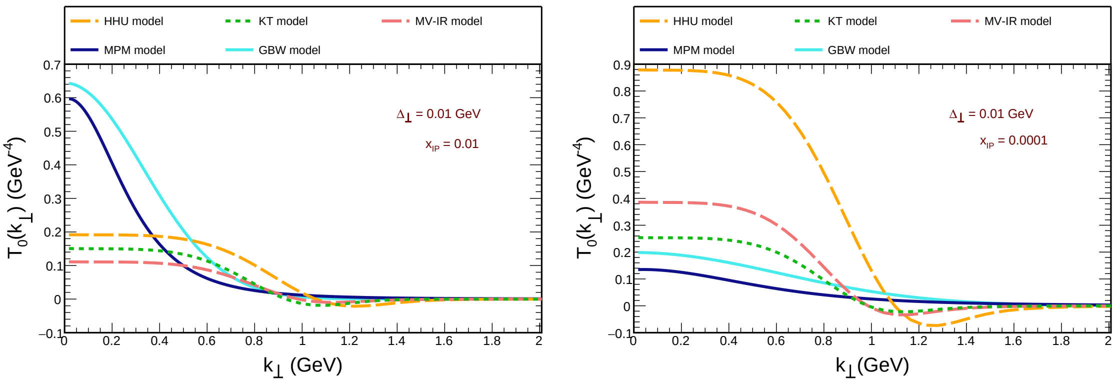

Figure 3.4: Different parametrizations of GTMD for $\Delta_\perp = 0.01$ GeV and $x_{\mathbb{P}} = 0.01$ (left) and $x_{\mathbb{P}} = 0.0001$ (right). The regularization parameter $\varepsilon = (0.5\,\text{fm})^{-2}$ was chosen for the HHU, MV-IR, and KT models.

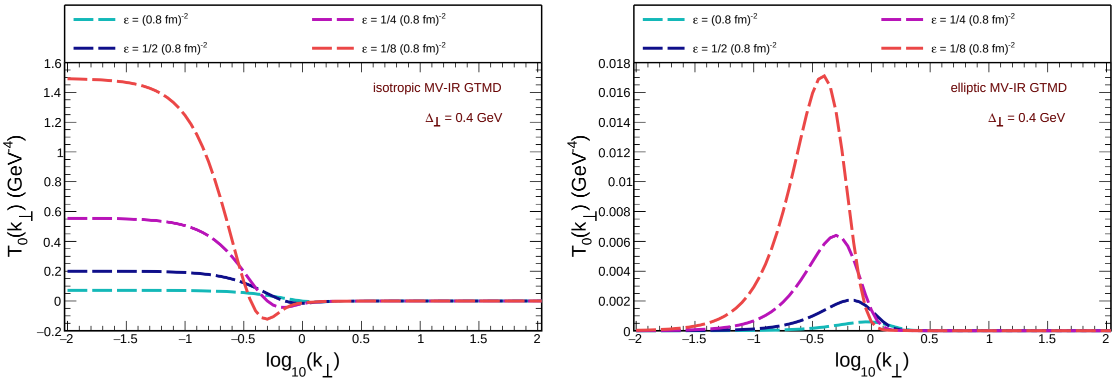

Figure 3.5: MV-IR GTMD depending on the $\log_{10}(k_\perp)$ for different value of the ε.

value of the function with an increase in ε. Moreover, in the case of the elliptical model, a shift of the amplitude peak relative to $\log_{10}(k_\perp)$ is also visible.

3.1.5 Numerical results

The influence of ε values on the amplitudes of individual GTMD models is also visible in the total cross-sections, which are presented in Table 3.1 where the results for $\varepsilon = (0.5\,\text{fm})^{-2}$ and $\varepsilon = 1/2(0.5\,\text{fm})^{-2}$ and an increase in total cross-sections is visible with a decrease in the value of this parameter for all cases considered. In addition, the charm quark mass $m_c = 1.5\,\text{GeV}$ was used in the calculations, and the kinematic domain was divided into two regions corresponding to $0.01 < P_\perp < 10.0\,\text{GeV}$ and $5.0 < P_\perp < 10.0\,\text{GeV}$, while the cross-section was also integrated over $\Delta_\perp < 3\,\text{GeV}$ due

	$x_{\mathbb{P}} < 1.0$		$x_{\mathbb{P}} < 0.05$	
GTMD approaches	σ (μb)	$\sigma_{P_\perp > 5.0\,\mathrm{GeV}}$ (μb)	σ (μb)	$\sigma_{P_\perp > 5.0\,\mathrm{GeV}}$ (μb)
GBW	335.199	0.051	330.046	0.046
MPM	321.141	0.201	293.300	0.173
$\varepsilon = (0.5\,\mathrm{fm})^{-2}$				
HHU	520.691	4.573	520.691	4.573
KT	66.699	0.111	65.023	0.110
MV-IR	136.675	0.606	129.883	0.526
$\varepsilon = \frac{1}{2}(0.5\,\mathrm{fm})^{-2}$				
HHU	743.411	4.348	743.411	4.348
KT	85.487	0.106	83.039	0.105
MV-IR	169.561	0.587	161.360	0.510

Table 3.1: Integrated cross-section for $0.01 < P_\perp < 10.0$ GeV and for $5.0 < P_\perp < 10.0$ GeV and different approaches of the GTMD.

to GTMD zeroing outside this area. As this approach works well for small values of $x_{\mathbb{P}}$, for comparison, not only are presented the results corresponding to a wide range of this value but also the cases where $x_{\mathbb{P}} < 0.05$, which is the conventional limit of the applicability of the used GTMDs. However, there is a very slight decrease in the value of the integrated cross-section after limiting the kinematic area to small $x_{\mathbb{P}}$ for all the models considered, therefore further analysis does not take this cut into account. However, there are significant differences between the values of total cross-sections for individual models. The GBW and MPM models give relatively similar results but they do not overlap with the KT, HHU, and MV-IR, the values of which differ several times.

The reason for the drastic drop in the value of the total cross-section after assuming an additional cut on $P_\perp$ is visible in Fig. 3.6, within the considered $10\,\mathrm{GeV}$ there is a visible decrease in the value of the differential cross-section by five orders of magnitude. Although differences between individual models are visible even at small relative transverse momenta, they become much more significant in the tails of the distributions. The softest behavior occurs in the GBW model, which is related to its glue and is consistent with predictions. There is also a noticeable different impact of the ε cut on individual models. In particular, the KT model is in the area of small $P_\perp$, where a significant part of the cross-section is concentrated. This affects much lower values of the obtained results

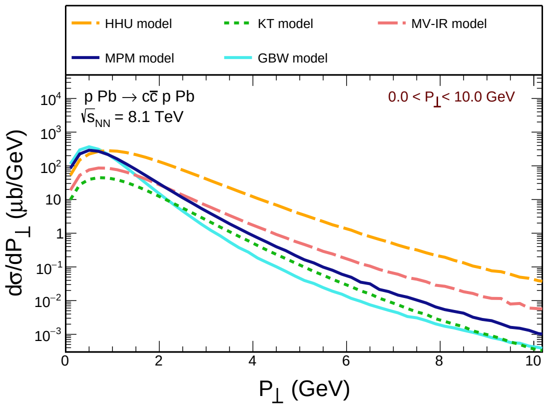

Figure 3.6: $P_\perp$ dependence of the cross-section for the diffractive mechanism.

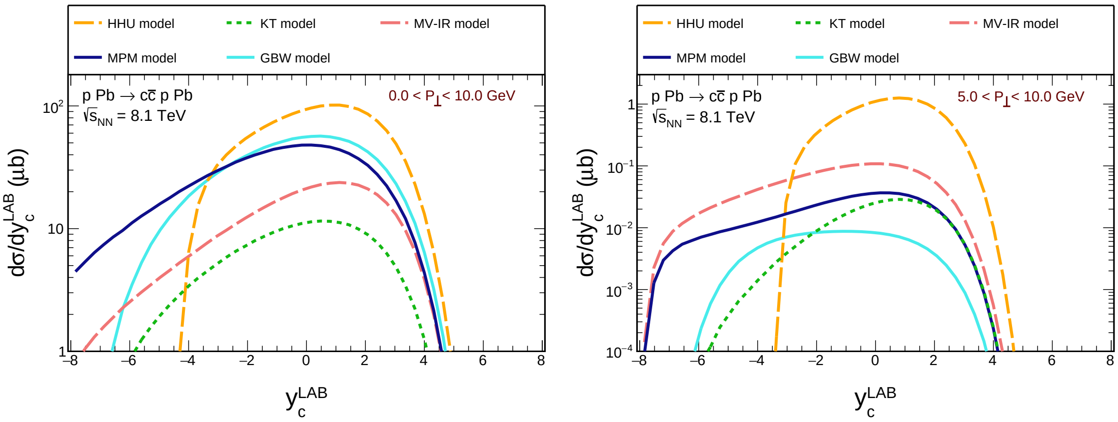

Figure 3.7: Quark rapidity in the laboratory frame dependence of the cross-section for the diffractive mechanism for wide $P_\perp$ region (left) and $5.0 < P_\perp < 10.0\,\mathrm{GeV}$ (right).

compared to other approaches and thus confirms the need to adapt this parameter to the experimental data.

The differences between individual models are even more pronounced in the lab-frame distribution of the rapidity of the produced charm quarks in Fig. 3.7. In this figure, the incoming nucleus has high positive rapidity values while the proton has negative rapidity, and the range of distributions for the high value of this variable is closely related to the photon flux. In particular, the HHU model gives a much larger cross-section peak than the other GTMDs and only reaches up to $y_c^{LAB} \sim -4$, which is due to the fact, that it only supports small $x_{\mathbb{P}}$ <0.01. The GBW distribution, on the other hand, gives results consistent with previous cases available in the literature, such as the work of Gonçalves et al. from Ref. [110].

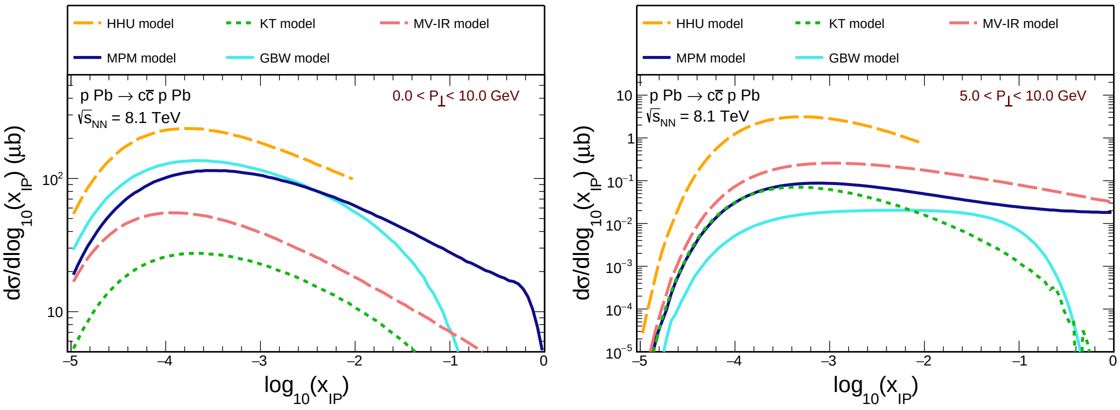

Figure 3.8: Pomeron-x dependence of the cross-section for the diffractive mechanism for wide $P_\perp$ region (left) and $5.0 < P_\perp < 10.0\,\mathrm{GeV}$ (right).

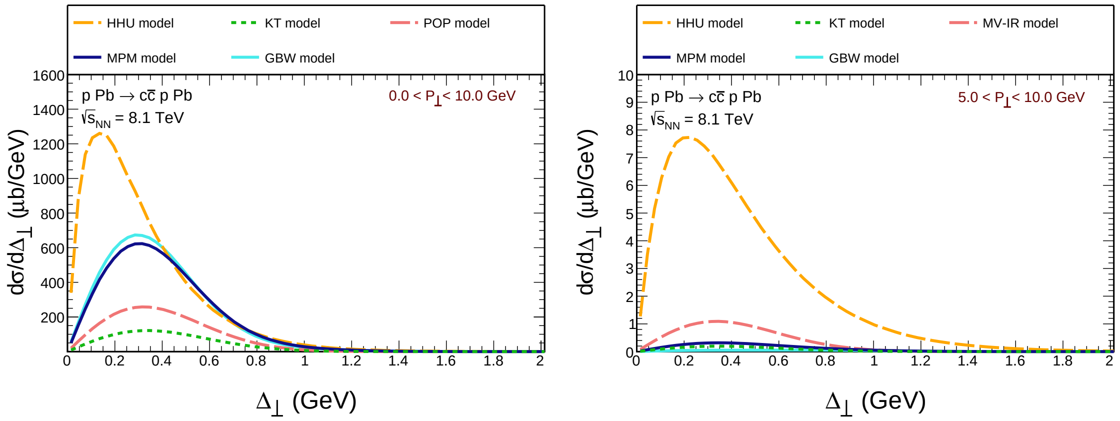

Figure 3.9: Transverse momentum of the produced quark pair dependence of the cross-section for the diffractive mechanism for wide $P_\perp$ region (left) and $5.0 < P_\perp < 10.0\,\mathrm{GeV}$ (right).

Also worth attention are the distributions in $x_{\mathbb{P}}$ presented in Fig. 3.8, which include even $x_{\mathbb{P}}$ down to 10^{-5}. Please note that the HHU model only, as applicable $x_{\mathbb{P}}$ smaller than 0.01. The experimental significance of this distribution is related to the fact that the diffractionally scattered proton will carry a fraction $\xi \approx 1 - x_{\mathbb{P}}$ of the beam momentum, and the difference in the rapidity gap between the photon dissociation products increases for small $x_{\mathbb{P}}$, as evidenced by $\propto \log(1/(1-\xi)) \sim \log(1/x_{\mathbb{P}})$. Therefore, an experiment with tagged protons carrying part of the momentum of the beam will provide an upper bound on $x_{\mathbb{P}}$. A detailed discussion of the relevant forward detectors at the LHC can be found in the Refs [87, 88, 89]. This issue is related to the applicability of the dipole amplitudes in experimental conditions, which, as mentioned, requires a large rapidity gap. Furthermore, when using this approach there will not be a sharp limit on $x_{\mathbb{P}}$ at which it breaks down, but rather it will require $x_{\mathbb{P}} \ll 0.1$ with a conservative upper limit of $x_{\mathbb{P}} < 0.05$.

Due to the lack of experimental conditions, this analysis covers the entire phase space, up to $x_{\mathbb{P}}^{\max} = 1$, assuming that the effect of the large $x_{\mathbb{P}}$ on the integrals will be generally small. The exception to this assumption is the rapidity distributions involving the large negative values of rapidity, which are located close to the proton beam and therefore are associated with small gaps, see Section 3.1.6.

Overall, the distribution in the transverse momenta of the produced system is shown in Fig. 3.9. As expected the cross-section is largest at values of $\Delta_\perp \sim 1/\sqrt{B}$, where B is the diffraction slope, as it should be for diffractive scattering. Only the HHU model produces a peak in the $\Delta_\perp$ distribution, which is shifted to a softer value than in the case of other GTMD models. This is the result of the gluon dynamics encoded in the BK equation. These distributions can also probably be made more realistic by introducing a cutoff function in the impact parameter variable $b_\perp$ in the Eq. (3.45) similarly to the dipole size $r_\perp$. However, this would involve the introduction of an additional parameter, so this procedure was omitted in this study.

Fig. 3.10 shows the distribution in the Mandelstam-t, defined in this case as

$$t = -\frac{\Delta_\perp^2 + x_{\mathbb{P}}^2 m_p^2}{1 - x_{\mathbb{P}}}, \tag{3.48}$$

at the proton side. This distribution has a characteristic diffraction peak corresponding to the integrated $P_\perp$. Once again, the HHU approach differs from the other models, in this case by a slightly different shape of the distribution curve and a very sharp peak at small t. In the case of larger relative transverse momenta, the distribution in this Mandelstam

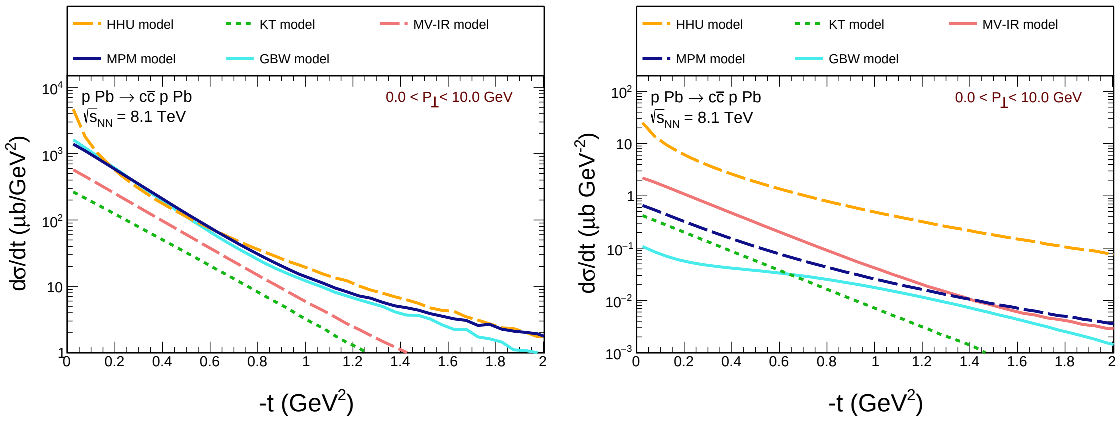

Figure 3.10: Mandelstam t dependence of the cross-section for the diffractive mechanism for wide $P_\perp$ region (left) and $5.0 < P_\perp < 10.0\,\mathrm{GeV}$ (right).

variable t flattens out significantly in all the considered models. It is worth mentioning that this case corresponds to a rather large diffractive mass and therefore to a significant longitudinal momentum transfer.

The last important aspect of diffraction production of $c\bar{c}$ pairs in proton-lead collisions are the distributions in the azimuthal angle ϕ between $\vec{P}_\perp$ and $\vec{\Delta}_\perp$, which are normalized to the cross-section and can be seen in Fig. 3.11. Firstly, in the case of GBW and MPM GTMDs, these correlations are of "geometric" origin such that in momentum space they are entirely generated by the matrix element. The fluctuations obtained in this way are of the order of 10% for a wide area $P_\perp$, while at larger relative momenta their values drop quickly, which is accompanied by a change in the shape of their distribution. This is due to the fact, that both models take into account all possible harmonics, not just $\cos 2\phi$ as in HHU and MV-IR models. However, correlations resulting from the elliptical contribution of gluons (see Eq. (3.37)), only modifications including of $\cos 2\phi$ are taken into account, which turns out to be approximately $1 - 5\%$.

Due to the parton level of the discussed distributions, it is not possible to measure them directly, and in the case of dijets, it is expected that soft gluon corrections will rather have an impact (see e.g. Ref. [111]). However, in the exclusive (or inclusive) diffraction pairs of heavy-flavor mesons, such as D mesons, hadronization corrections should be taken into account, which is beyond the scope of this analysis. There are LHCb collaboration studies on the measurement of inclusive dijet $c\bar{c}$ [112] (see also [113]). Therefore, the question arises whether such a measurement would also be possible in the discussed kinematics. As different models show different behavior in azimuthal angles, the distributions for 5.0

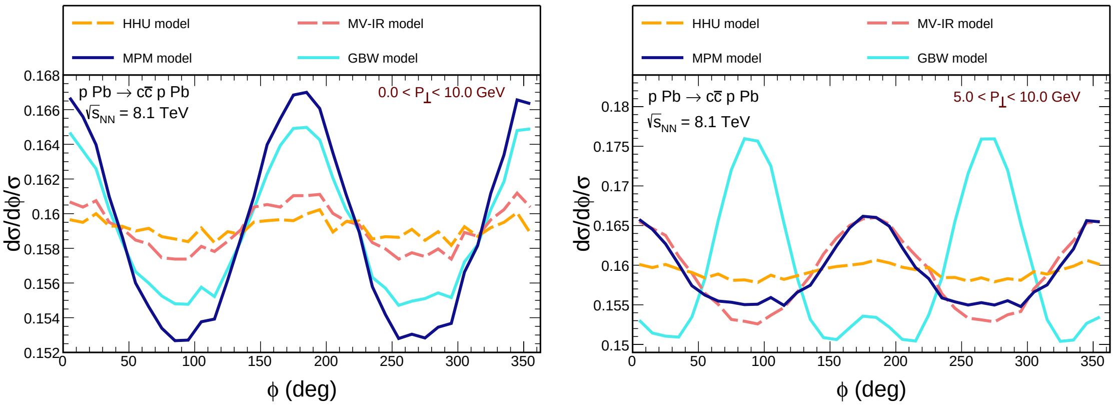

Figure 3.11: Azimuthal angle dependence of the cross-section normalized to the total cross-section for the diffractive mechanism for wide $P_\perp$ region (left) and $5.0 < P_\perp < 10.0\,\mathrm{GeV}$ (right). Notice the normalization.

$< P_\perp < 10.0\,\mathrm{GeV}$ are particularly interesting, in which the location of the maxima for some models is reversed.

3.1.6 Cutoff in $x_{\mathbb{P}}$ or MPM model distributions

The only thing that requires clarification now is the issue of the cutoff in $x_{\mathbb{P}}$, for discussion of which the distributions of the MPM model in the quark rapidity, the transverse momentum of the pair $c\bar{c}$ and the azimuthal angle after introducing the upper border $x_{\mathbb{P}}^{\max}$ into integration. In the case of the dependence of the cross-section on y_c^{LAB} from Fig. 3.12, the expected effect of the cut-off is visible at large negative rapidities reaching above $y_c^{\mathrm{LAB}} \sim -4$, where the cross-section quickly decreases and this effect is more pronounced for larger $P_\perp$. The changes resulting from imposing an additional cut on $x_{\mathbb{P}}$ are insignificant in the case of the distribution in $\Delta_\perp$ from Fig. 3.13 and for the region including small $P_\perp$ only affect the peak height. The differences between both cases are slightly more visible in the high $P_\perp$ domain where the reduction in the cross-section value evenly covers $\Delta_\perp > 0.3\,\mathrm{GeV}$. Finally, the azimuthal angle ϕ distribution shown in Fig. 3.14 remains practically unchanged for both considered regions of the $P_\perp$.

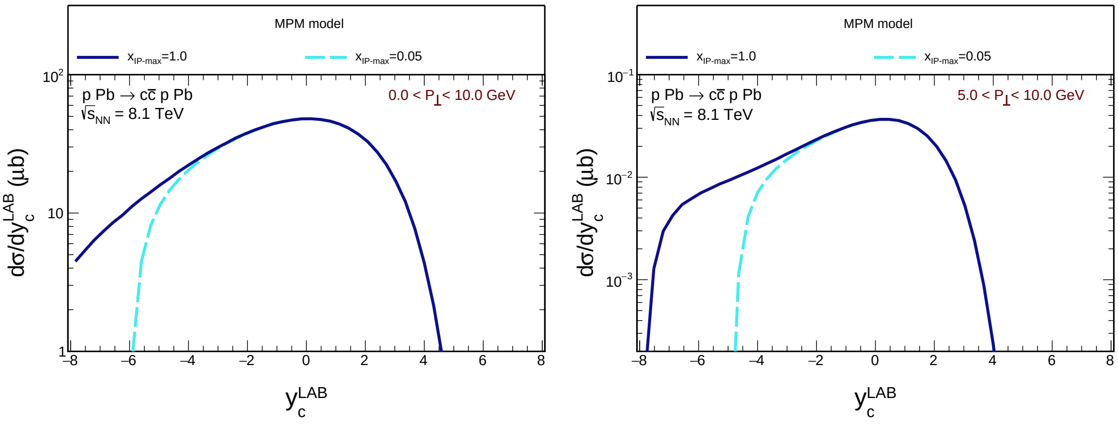

Figure 3.12: Quark rapidity in the laboratory frame dependence of the MPM model cross-section for the diffractive mechanism for wide $P_\perp$ region (left) and $5.0 < P_\perp < 10.0\,\mathrm{GeV}$ (right) for two different $x_{\mathbb{P}}$ regions.

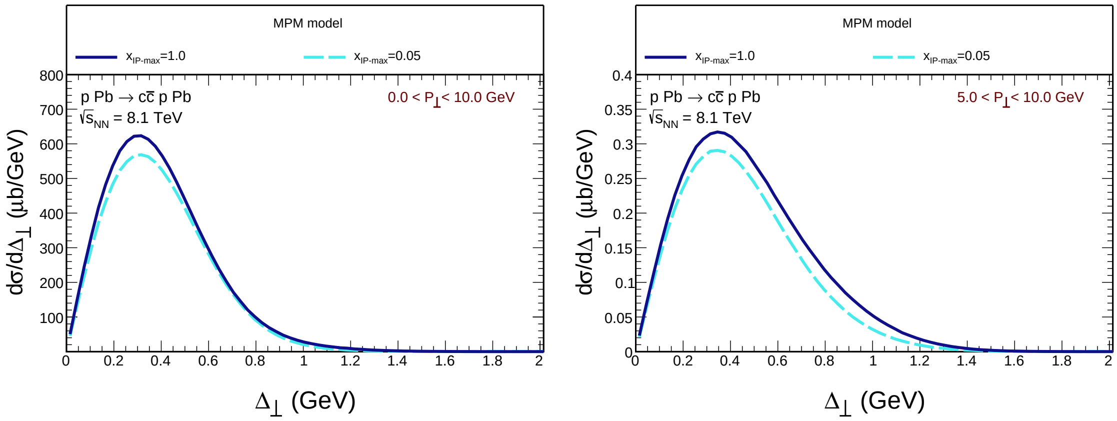

Figure 3.13: Transverse momentum of the $c\bar{c}$-system dependence of the MPM model cross-section for the diffractive mechanism for wide $P_\perp$ region (left) and $5.0 < P_\perp < 10.0\,\mathrm{GeV}$ (right) for two different $x_{\mathbb{P}}$ regions.

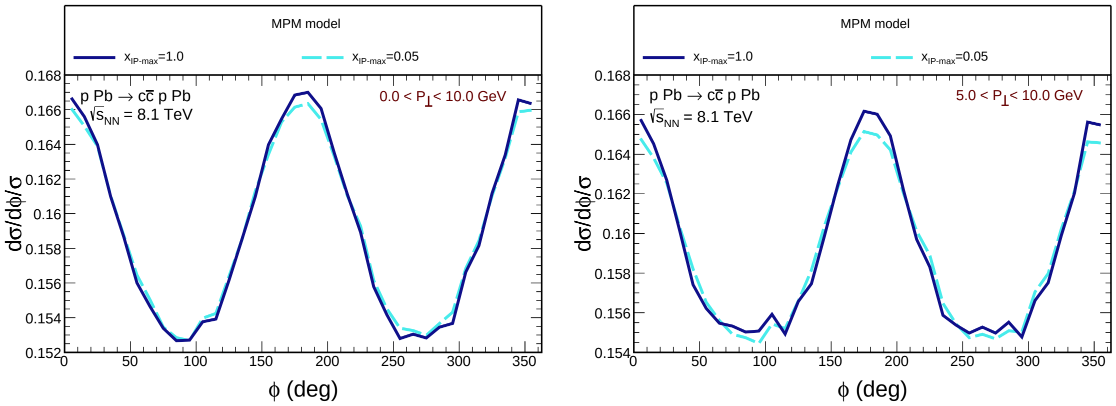

Figure 3.14: Azimuthal angle dependence of the MPM model cross-section for the diffractive mechanism for wide $P_\perp$ region (left) and $5.0 < P_\perp < 10.0\,\mathrm{GeV}$ (right) for two different $x_{\mathbb{P}}$ regions.

3.2 $\gamma\gamma$ mechanism

Although the contribution of processes initiated by the exchange of two photons is considered rather small, $c\bar{c}$ pairs may also be formed in this type of process. Similarly to the pairs of e^+e^-, $\mu^+\mu^-$ or $t\bar{t}$ [59] and W^+W^- [60]. These mechanisms are analogous in all the cases mentioned, and Feynman's diagrams for the production of $c\bar{c}$ are presented in Fig. 3.15. The theoretical basis for the description of this type of process is almost identical to the previously considered lepton productions but requires taking into account their parameters, i.e. different mass, charge of quarks, and colors available for them:

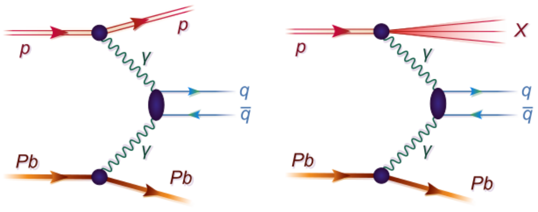

Figure 3.15: Different mechanisms of the $c\bar{c}$ pair production in proton-nucleus collisions.

$$\begin{aligned}\sigma \;&=\; S^2 e_f^2 N_c \int dx_p dx_{Pb} \frac{d^2\vec{q}_T}{\pi}\left[\frac{d\gamma_{el}^p(x_p,Q^2)}{dQ^2} + \frac{d\gamma_{ine}^p(x_p,Q^2)}{dQ^2}\right]\gamma_{el}^{Pb}(x_{Pb}) \\ &\times\; \sigma_{\gamma^*\gamma\to l^+l^-}(x_p, x_{Pb}, \vec{q}_T), \qquad (3.49)\end{aligned}$$

for the process considered, which is the production of $c\bar{c}$ pair, $e_f = \frac{2}{3}$ and $N_c = 3$.

Depending on the value of the cut mentioned, the total cross-section on $pA \to c\bar{c}p(X)A$ is presented in Table 3.2.

$\gamma\gamma$ mechanism			
	$5.0\,\mathrm{GeV} < \mathrm{P}_\perp < 10.0\,\mathrm{GeV}$		
	$\Delta_\perp > 0.0\,\mathrm{GeV}$	$\Delta_\perp > 0.5\,\mathrm{GeV}$	$\Delta_\perp > 1.0\,\mathrm{GeV}$
elastic	13.151	0.815	0.0744
ALLM	16.079	14.420	12.300
FFJLM	14.933	12.204	7.497
LUX-like	18.032	16.342	13.855
KB	18.452	16.342	12.980
	$10.0\,\mathrm{GeV} < \mathrm{P}_\perp < 20.0\,\mathrm{GeV}$		
elastic	1.900	0.139	0.012
ALLM	2.621	2.384	2.082
FFJLM	2.070	1.682	1.031
LUX-like	3.021	2.762	2.403
KB	2.969	2.609	2.146

Table 3.2: Integrated cross-section for $\gamma\gamma$ production of the $c\bar{c}$ in nb for $5.0 < P_\perp < 10.0$ GeV and $10.0 < P_\perp < 20.0$ GeV.

As in the previous case, both elastic and inelastic collisions were taken into account, for which contributions corresponding to four structure function models were calculated. In a situation where the condition on $P_\perp$ almost does not limit the kinematic area, the cross-section considered is comparable to the production of electron-positron pairs. Moreover, elastic collisions then have the largest contribution, comparable to FFJLM, while the smallest cross-section corresponds to ALLM. This situation changes when the area is reduced to $P_\perp > 5.0\,\mathrm{GeV}$ where the elastic contribution is the smallest, similar to FFJLM. LUX-like and KB parametrizations again give very similar results, with the cross-section for ALLM being slightly smaller. It should be noted that imposing this condition equates to a twenty-fold decrease in the total cross-section.

The differences visible in the values of the total cross-section are perfectly illustrated in Fig. 3.16, where there is a noticeable similarity in the distributions taken into account and a much higher value of the elastic component and the FFJLM model than the other models for $P_\perp < 2.0\,\mathrm{GeV}$. Moreover, the differential cross-section decreases with the

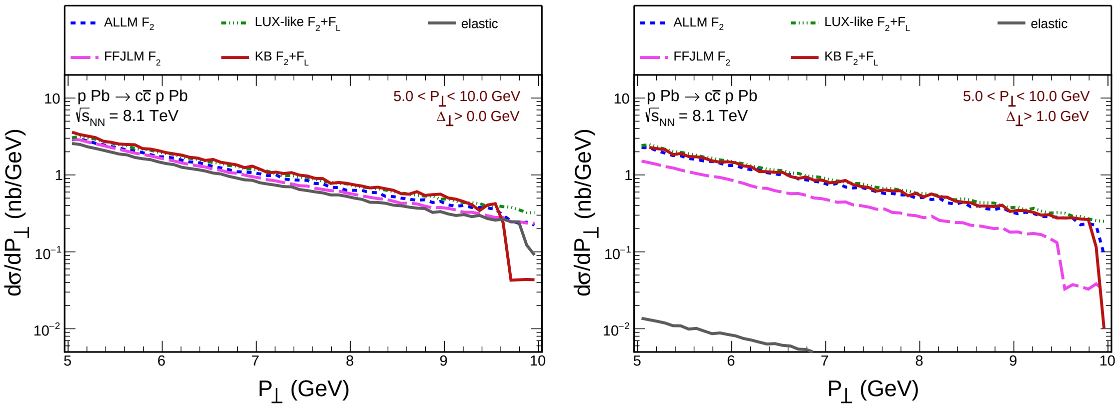

Figure 3.16: $P_\perp$ dependence of the cross-section for the $\gamma\gamma$ mechanism for wide $\Delta_\perp$ region (left) and high $\Delta_\perp$ region (right).

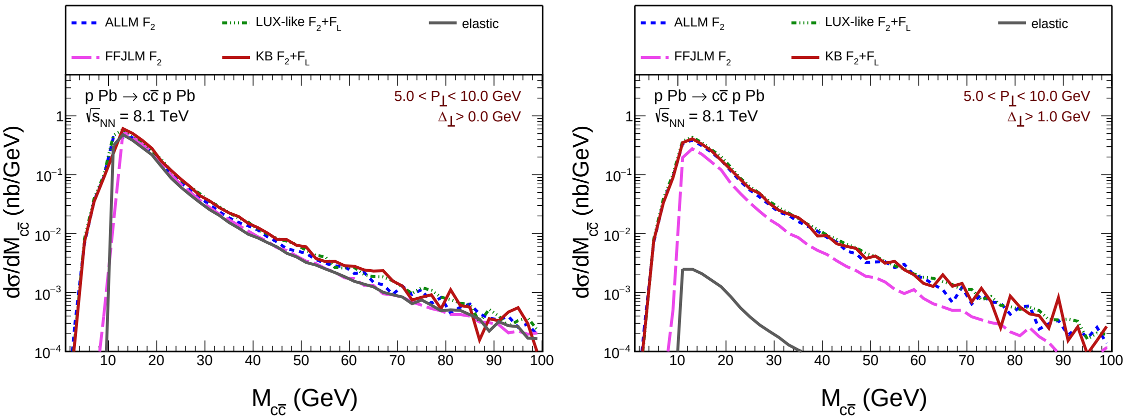

Figure 3.17: $c\bar{c}$ pair invariant mass dependence of the cross-section for the $\gamma\gamma$ mechanism for wide $\Delta_\perp$ region (left) and high $\Delta_\perp$ region (right).

increase of $P_\perp$ by as much as two orders of magnitude over $10\,\mathrm{GeV}$, which reflects the decrease in the total cross-section for large $P_\perp$.

Similarly, a significant decrease in the differential cross-section is seen as a function of the invariant mass of the produced quark pair, amounting to five orders of magnitude for a wide kinematic region. Both distributions visible in Fig. 3.17 show quite similar contributions from all the models considered. Only a slightly higher value of the elastic collision distribution for small masses is visible here. Moreover, similarly to the production of leptons, only particles with slightly larger masses are produced, which is again related to the occurrence of small virtualities of photons in the elastic and inelastic case

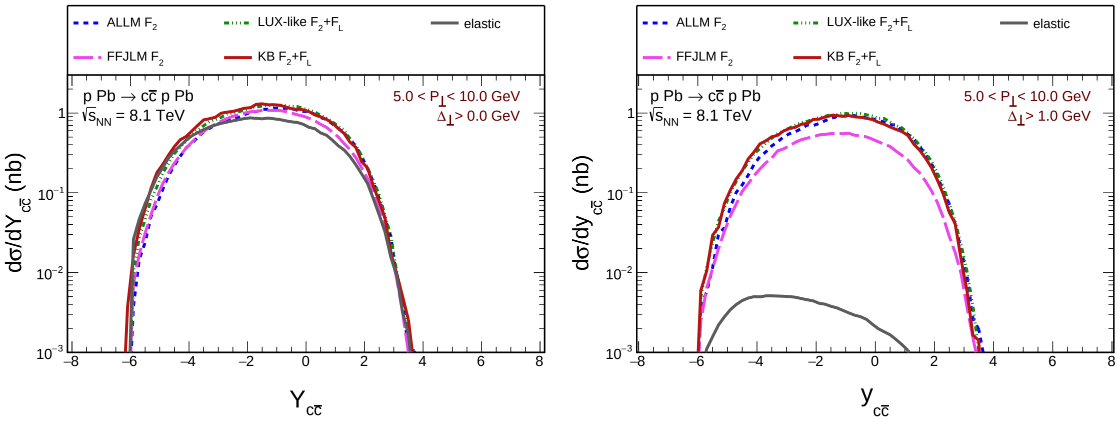

Figure 3.18: $c\bar{c}$ pair rapidity dependence of the cross-section for the $\gamma\gamma$ mechanism for wide $\Delta_\perp$ region (left) and high $\Delta_\perp$ region (right).

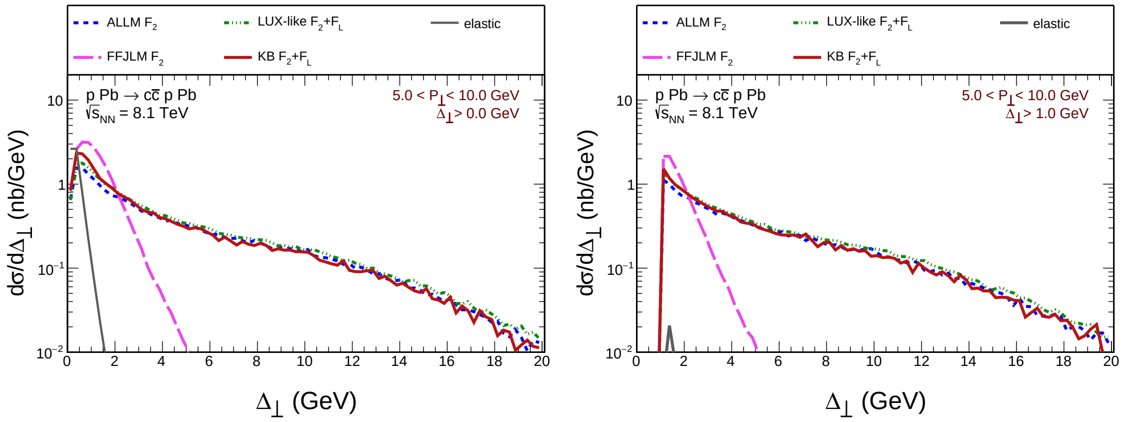

Figure 3.19: $c\bar{c}$ pair transverse momentum dependence of the cross-section for the $\gamma\gamma$ mechanism for wide $\Delta_\perp$ region (left) and high $\Delta_\perp$ region (right).

based on the FFJLM model, and the accompanying conditions imposed on the momenta of the produced pairs.

The differences between the individual distributions are slightly more visible for the $c\bar{c}$-system rapidity (see Fig. 3.18). The positive part of the kinematic region is almost identical in each case, which corresponds to the contribution from the nuclear side, while the results related to the inelastic proton contribution come from the negative rapidity region. However, the subtle differences are visible primarily at the top of the distribution, with Y_{ll} close to zero.

As expected, the elastic contribution to the differential distribution of the cross-section in the transverse momentum of the produced pair dominates for very small transverse mo-

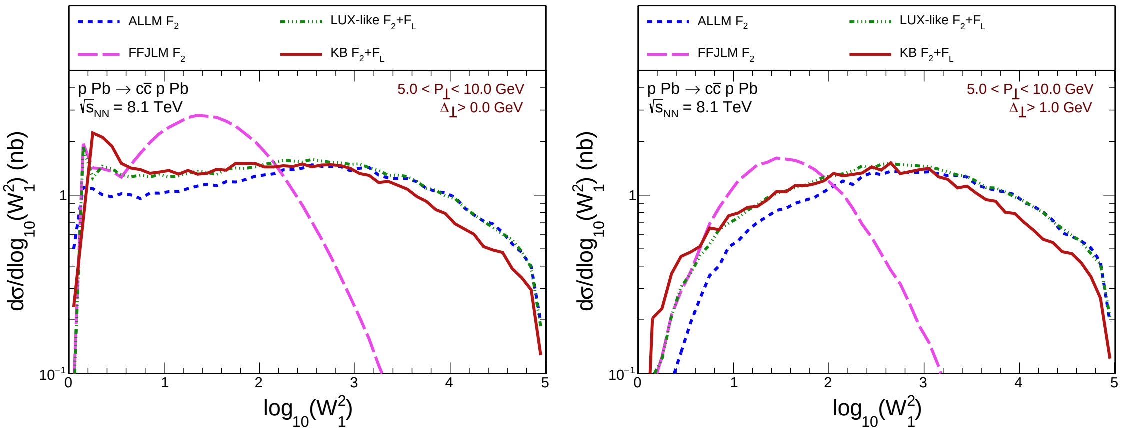

Figure 3.20: Energy of the photon-proton system dependence of the cross-section for the $\gamma\gamma$ mechanism for wide $\Delta_\perp$ region (left) and high $\Delta_\perp$ region (right).

menta but decreases very quickly. However, quite similar results are given by the FFJLM model, which also significantly outperforms the other contributions for small momenta, but does not overlap with any other model and gives negligible values for $P_\perp$ above $3\,\mathrm{GeV}$. The remaining distributions visible in Fig. 3.19 are very similar, and again the decrease in their values with an increase in a given observable is much smaller after taking into account cuts on $\Delta_\perp$.

It is also worth paying attention to the distribution of individual inelastic contributions as a function of the energy of the photon-proton system from Fig.3.20, where the largest differences correspond to the area of occurrence of resonances at small W_1, their absence in the ALLM model is clearly visible. Also noticeable is the significantly different shape of the FFJLM curve at intermediate photon-proton energies and its decrease for large W_1, which is almost absent in the case of other parametrizations.

Finally, the distributions in the structure function variables can be seen in Fig. 3.21 and 3.22. The distributions in x_{Bj} for a wide range of transverse momentum seem to be quite similar for all models considered, while at larger $\Delta_\perp$ the drop in the cross-section value at smaller Bjorken-x is much more significant. The differences between this model and the remaining ones are even more visible in the photon virtuality distributions, where the peak at $Q^2 < 10.0\,\mathrm{GeV}^2$ is visible. Furthermore, the virtuality area smaller than $1.0\,\mathrm{GeV}^2$ is not available when the condition on $\Delta_\perp > 1.0\,\mathrm{GeV}$ is imposed. However, this is an area where, taking into account small $\Delta_\perp$, differences between the ALLM, LUX-like, and KB models are visible.

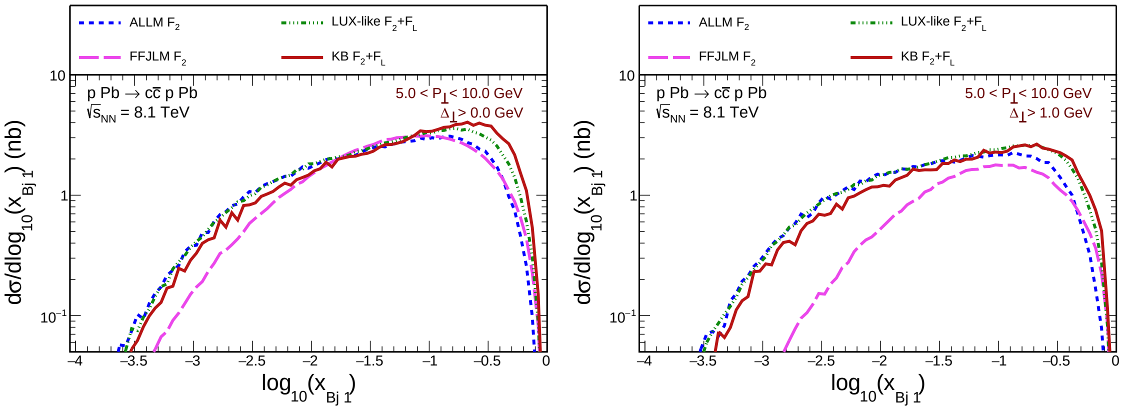

Figure 3.21: Bjorken variable-x dependence of the cross-section for the $\gamma\gamma$ mechanism for wide $\Delta_\perp$ region (left) and high $\Delta_\perp$ region (right).

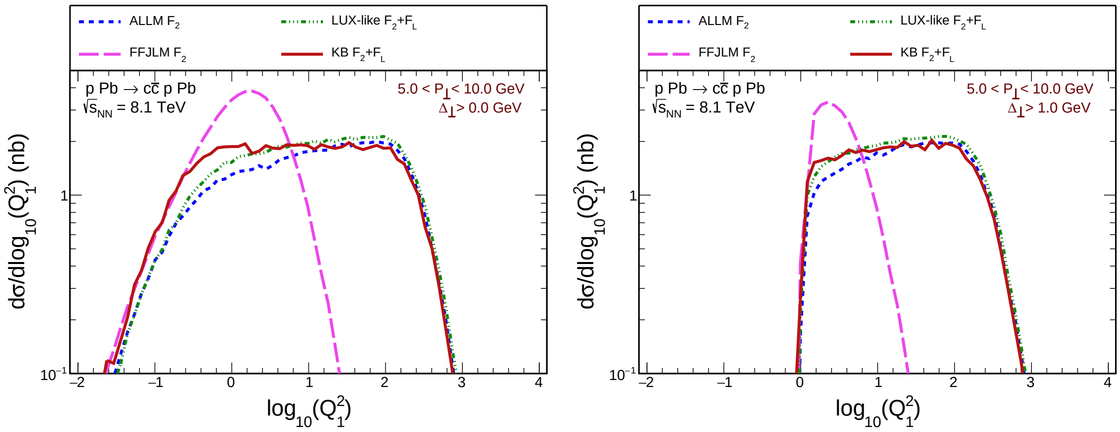

Figure 3.22: Virtuality dependence of the cross-section for the $\gamma\gamma$ mechanism for wide $\Delta_\perp$ region (left) and high $\Delta_\perp$ region (right).

3.3 Comparison of diffractive and $\gamma\gamma$ mechanisms

As mentioned already, the production of particles in the $\gamma\gamma$ mechanism is considered less significant compared to the diffraction mechanism therefore, it was decided to compare both mechanisms tested to eliminate any related doubts. The kinematic region considered further coincides with that used for the exchange of two photons. The integrated cross-sections for the production of dijets in both of these processes are presented in Table 3.3. It contains only one example of a structure function model due to the similarities in the considered approaches and the LUX-like model was chosen. Additionally, to better illustrate the situation, it also includes a cross-section of elastic processes, the contribution of which is small compared to the inelastic one, omitting the case of small relative transverse momenta and lack of cuts on $\Delta_\perp$, in which range a significant dominance of the diffraction mechanism is visible. Due to the lack of reference to the dipole approach used in the experimental data in the case of diffraction production, it was decided to include all five GTMD models. Although the region $5.0\,\mathrm{GeV} < \mathrm{P}_\perp < 10.0\,\mathrm{GeV}$ and $\Delta_\perp > 0.0\,\mathrm{GeV}$ is clearly dominated by diffraction processes, this dominance decreases as additional cuts are imposed on $\Delta_\perp$ and with its value greater than $1\,\mathrm{GeV}$ the cross-section for two-photon processes is already twice as high as most GTMD models. This situation worsens even more after taking into account $P_\perp > 10.0\,\mathrm{GeV}$, which area is already clearly dominated by the exchange of two photons, due to the drastic decrease in the cross-section for the diffraction mechanism.

The rapid decrease in the cross-sections on recent processes is related to the dependence of GTMD on its variables, in particular $\Delta_\perp$, in which at approximately $2.0\,\mathrm{GeV}$ the amplitudes $T_0(\Delta_\perp, k)$ are already close to zero as seen in Fig. 3.3. The distribution of the cross-section in this variable is presented in Fig. 3.23, which clearly shows higher cross-sections based on GTMD over $\gamma\gamma$ processes for very small $\Delta_\perp$ and their strong decrease contributing to the area above $1.5\,\mathrm{GeV}$ which is dominated by LUX-like results, in which case the value remains consistently around $1.0\,\mathrm{nb}/\mathrm{GeV}$. Only the cross-sections corresponding to the HHU model are above the black dotted line, but even in this case, the significance decreases at the very end of the tail. Although imposing cuts on the transverse momentum of a pair of particles is experimentally difficult, the presented relations prove that when measuring such processes, $c\bar{c}$ pair with larger momenta come from production initiated by two photons.

	$5.0\,\mathrm{GeV} < \mathrm{P}_\perp < 10.0\,\mathrm{GeV}$		
	$\Delta_\perp > 0.0\,\mathrm{GeV}$	$\Delta_\perp > 0.5\,\mathrm{GeV}$	$\Delta_\perp > 1.0\,\mathrm{GeV}$
$\gamma\gamma$ mechanism			
elastic	13.151	0.815	0.0744
LUX-like	18.032	16.342	13.855
diffractive mechanism			
GBW	40.567	25.933	5.776
MPM	159.63	66.599	7.475
KT	86.925	30.383	1.329
MV-IR	500.16	164.761	5.774
HHU	3791.65	1271.449	230.672

	$10.0\,\mathrm{GeV} < \mathrm{P}_\perp < 20.0\,\mathrm{GeV}$		
$\gamma\gamma$ mechanism			
elastic	1.900	0.139	0.012
LUX-like	3.021	2.762	2.403
diffractive mechanism			
GBW	0.773	0.651	0.164
MPM	1.829	1.105	0.218
KT	0.487	0.170	0.007
MV-IR	10.705	3.607	0.131
HHU	62.340	23.743	4.733

Table 3.3: Integrated cross-section for two different mechanisms of the $c\bar{c}$ production in nb for $5.0 < P_\perp < 10.0$ GeV and $10.0 < P_\perp < 20.0$ GeV.

The second GTMD variable is the relative transverse momentum, which also shows a faster decline in diffraction processes than in two-photon mechanisms. However, further analysis only covers the area of smaller transverse momenta from Table 3.3. Fig. 3.24 shows that all GTMD models are significantly higher than LUX-like, but their decline is much greater, so that at the upper limit of the considered range the GBW and KT models almost coincide with the $\gamma\gamma$ mechanism. Taking into account the cut at $\Delta_\perp > 1.0\,\mathrm{GeV}$ causes such a significant drop in the diffraction contribution that even with small relative

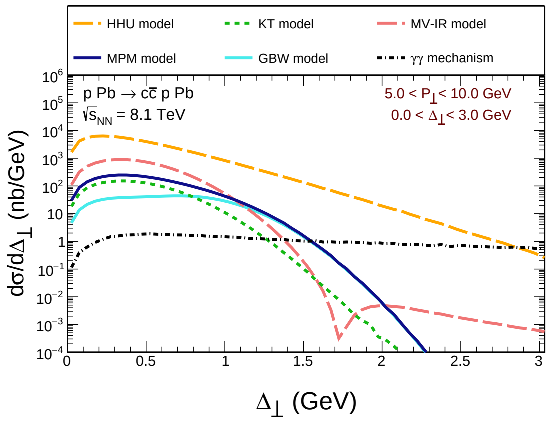

Figure 3.23: $c\bar{c}$ pair transverse momentum dependence of the cross-section for the both mechanisms.

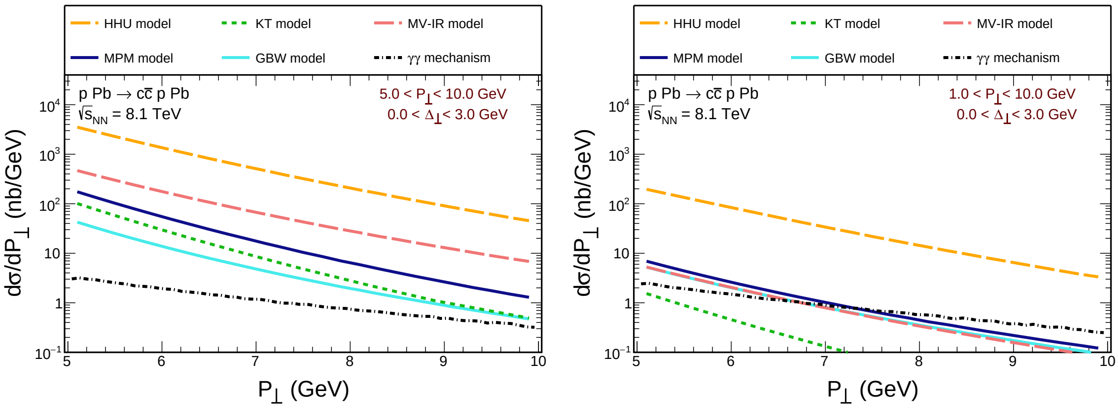

Figure 3.24: $P_\perp$ dependence of the cross-section for the diffractive mechanism for wide $\Delta_\perp$ region (left) and high $\Delta_\perp$ region (right).

transverse momenta all considered cases except HHU are comparable, and above $8.0\,\mathrm{GeV}$ significantly reverses the contributions of both types of reactions.

The differences between the contributions of the two mechanisms become more difficult to distinguish in the invariant mass and rapidity of the $c\bar{c}$ pair produced. Particles with small invariant masses are created only in $\gamma\gamma$ processes, which in this case, is also related to the kinematic conditions. However, larger tail distributions are similar to each other, so that already in a wider $\Delta_\perp$ region, the LUX-like results for large masses coincide with those of KT GTMD, while for larger transverse momenta the contribution of photon-photon processes is almost identical to diffraction MPM, GBW and MV-IR approaches.

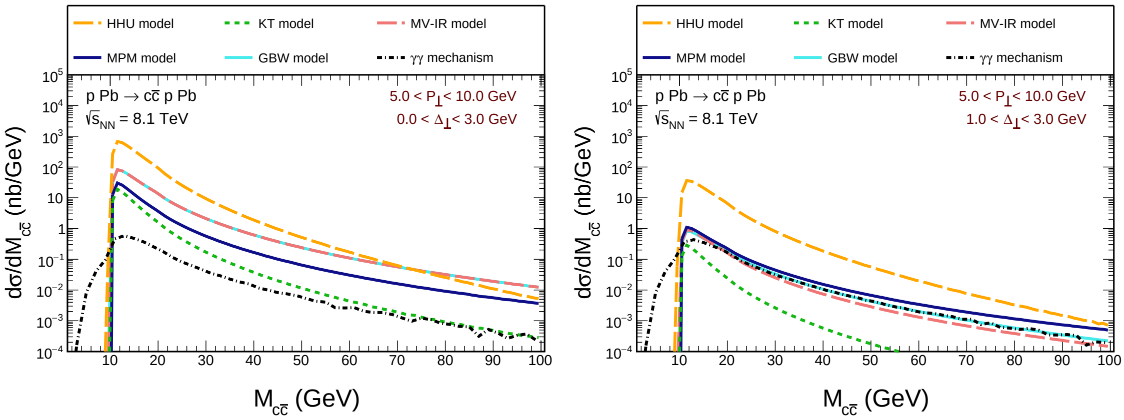

Figure 3.25: Invariant mass of the produced quarks dependence of the cross-section for the diffractive mechanism for wide $\Delta_\perp$ region (left) and high $\Delta_\perp$ region (right).

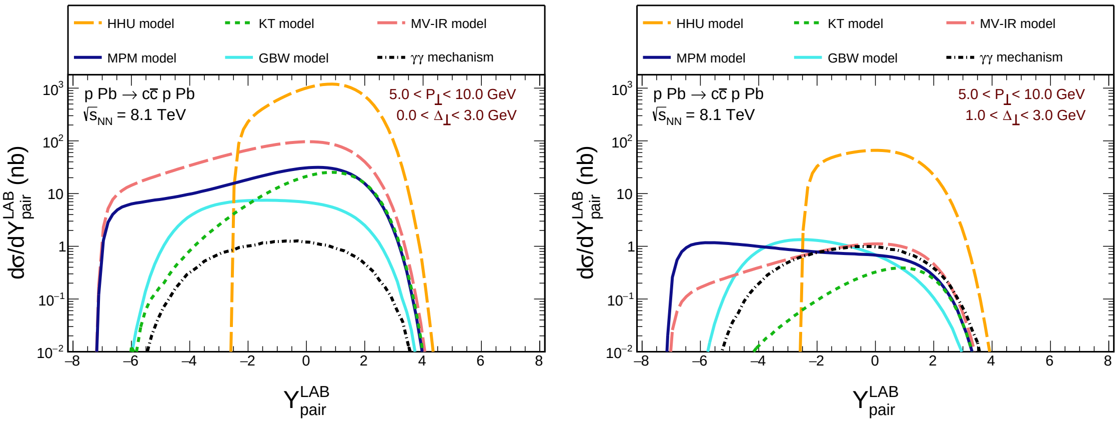

Figure 3.26: Rapidity of the produced quarks dependence of the cross-section for the diffractive mechanism for wide $\Delta_\perp$ region (left) and high $\Delta_\perp$ region (right).

Although in the cross-section distributions in the rapidity from Fig. 3.26 the degree of the contribution of two-photon processes is similar to the functions in the other variables, in this case, there are significant differences in the shapes of the individual contributions including the LUX-like.

Chapter 4

Diffractive dijet production in electron-proton collisions

4.1 Deep inelastic diffractive dijet production at HERA

The diversity of results obtained using individual GTMD models makes it impossible to determine which results are the most reliable hence the need to adjust them to experimental data. The ideal tool to achieve this goal is the scattering of ep at the Hadron-Electron Ring Accelerator - HERA, as proven in Ref. [114]. A particularly valuable final state for studying the distribution of gluons in the proton in the region of small x_{Bj} or a small fraction of the gluon momentum is the production of dijet. Due to this, it was decided to focus on dijet production in the reaction $ep \to e\,jj\,p$, with a proton in the final state. These processes have been measured at HERA thanks to the collaboration of H1 [115] and ZEUS [116]. The four pomeron QCD diagrams contributing to the exclusive diffractive production of dijets are presented in Fig. 4.1.

Experimentally, this requirement of exclusivity is very demanding because usually semi-exclusive processes $ep \to \;\; jj\,xp$ or even $ep \to jj\,xp^*$ are measured, where x denotes additional hadronic activity in the diffraction system in addition to dijet, while p^* corresponds to the possibility of exciting a proton to produce particles in its fragmentation region. However, this requirement is fulfilled by diffraction processes, which provide an ideal environment for testing Pomeron QCD models. These processes are conveniently described in the color dipole approach because the leading order process for diffractive masses $M^2 \sim Q^2$ is the diffractive excitation of the $q\bar{q}$ state of the virtual photon [79].

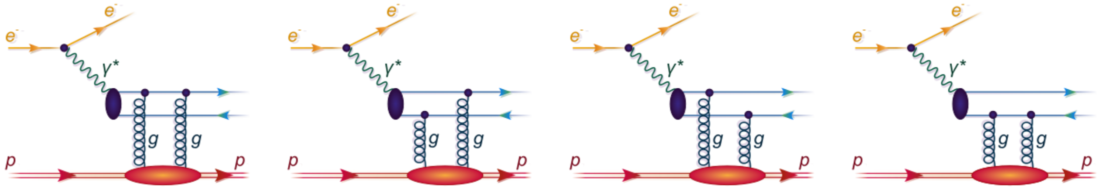

Figure 4.1: Four mechanisms of the diffractive production of the dijets in the electron-proton collisions.

These processes have already been considered in the color dipole approach in several related parameterizations e.g. in Refs [69, 81, 82, 84, 85, 86, 95, 108, 117, 118, 119, 120]. In contrast, the photoproduction limit applicable to ultraperipheral heavy-ion collisions in this context is found in Ref. [121]. There is also an analysis opting for the parton structure of the pomeron in the collinear factorization approach, including diffractive parton distributions. This approach only applies to inclusive diffraction, but the calculations include high orders (next-to-next-to leading orders) in the perturbative expansion [122].

The following considerations are also based on the color dipole approach, but in momentum space, and the information contained in the dipole amplitude is transferred, similarly to the production of $c\bar{c}$ in proton-nucleus collisions, to off-forward transverse momentum dependent gluon distributions. This approach is commonly referred to as GTMDs in the literature (see Refs [76, 123]), and at large jet momentum the forward diffraction amplitude directly probes the distribution of the unintegrated gluon, see Refs [70, 71]. The above approach is only appropriate for the low x_{Bj} or high energy limit and only considers transverse momentum transfer. The same formalism was used in Ref. [119], which uses the parametrization of the dipole amplitude [98] of Golec-Biernat-Wüsthoff. For the appropriate gluon distribution, the results and conclusions found there are consistent with this analysis.

In addition to the five GTMD models mentioned so far, in this case, it was also decided to include the analogous model proposed by D. Boer and C. Setyadi (see Refs [81, 120]). This model differs from the MV-IR parametrization by an additional dependence following Ref. [81]:

$$N_0(r_\perp, b_\perp) = -\frac{1}{4} r_\perp^2 \chi Q_s^2(b_\perp) \ln\left[\frac{1}{r_\perp^2 \lambda_N^2} + e\right], \tag{4.1}$$

where $\lambda_N = 0.24\,\mathrm{Gev}$, and

$$Q_s^2(b_\perp) = \frac{4\pi\alpha_s C_F}{N_c} Q_{0s}^2 \exp\left[\frac{-b_\perp^2}{2R_p^2}\right]. \tag{4.2}$$

The strong coupling constant was assumed $\alpha = 0.3$, $Q_0^2 - 1.0\,\mathrm{GeV}^2$ as in Ref. [81], while $C_F = 4/3$ and $N_c = 3$. However, as in the case of the MV-IR model, there is no dependence on $x_{\mathbb{P}}$. The amplitude distribution of the model proposed by D. Boer and C. Setyadi in $\Delta_\perp$ and $\log_{10}(k_\perp)$ is visible in Fig. 4.2, and from now on it will be called the MV-BS 2021 parametrization. The second model proposed by the same authors in Ref. [120], hereinafter referred to as MV-BS 2023, was also used and is presented in Fig. 4.2. This model depends on x_{Bj} by replacing the χ factor:

$$\chi(x_{Bj}) = \bar{\chi}\Big(\frac{x_0}{x_{Bj}}\Big)^{\lambda_\chi}, \tag{4.3}$$

where $\bar{\chi} = 1.5$, $x_0 = 0.0001$ and $\lambda_\chi = 0.29$.

The figure below shows the case where, in addition to the parameter $\varepsilon = (0.5\,\mathrm{fm})^{-2}$, there is also $\chi = 1.25$, the value of which is consistent with Ref. [81]. In principle, this parameter (or $\bar{\chi}$ for the MV-BS 2023 model) can be treated as a parameter adapted to the experimental data because it also significantly affects the results of the calculations.

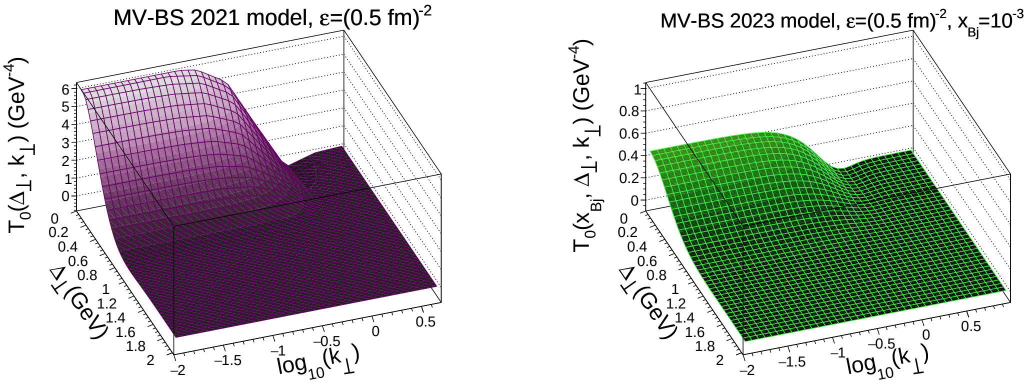

Figure 4.2: MV-BS 2021 (left) and MV-BS 2023 (right) models of the GTMD depending on the $\Delta_\perp$ and $\log_{10}(k_\perp)$. This model takes into account the $\varepsilon = (0.5\,\mathrm{fm})^{-2}$ parameter.

4.1.1 Formalism of the cross-section calculation

The basic kinematic quantities are calculated, in the case of the considered processes, analogously to $pA \to c\bar{c}pA$. However, the cross-section is calculated slightly differently, because in this case it is assumed that the transverse and longitudinal photon contributions are taken into account separately, according to the relation

$$\frac{d\sigma^{ep}}{dydQ^2d\xi} \;=\; \frac{\alpha_{em}}{\pi y Q^2}\Big[\Big(1-y+\frac{y^2}{2}\Big)\frac{d\sigma_T^{\gamma^*p}}{d\xi}+(1-y)\frac{d\sigma_L^{\gamma^*p}}{d\xi}\Big], \tag{4.4}$$

with $d\xi = dzd^2\vec{P}_\perp d^2\vec{\Delta}_\perp$. Therefore it is necessary to use not only the light-front wave function for transverse contribution from Eq. 3.26 but also the longitudinal one:

$$\Psi_L^{\gamma^*\to q\bar{q}}(\vec{k}_\perp, z) = \frac{eZ_f[z(1-z)]^{3/2}\delta_{ij}2Q(1-\delta_{\sigma\sigma'})}{\vec{k}_\perp^2+m_f^2+Q^2z(1-z)}. \tag{4.5}$$

Moreover, due to the averaging of the angle between the electron scattering plane and the hadron plane, it is possible to neglect interference between photon polarizations. In such a situation this interference disappears, and the cross-section on $\gamma^* p \to q\bar{q}p$ discussed in general form in more detail in the Appendix A is expressed for transverse:

$$\begin{aligned}\frac{d\sigma_T^{\gamma^*p}}{dzd^2\vec{P}_\perp d^2\vec{\Delta}_\perp} &= 2N_c\alpha_{em}\sum_f e_f^2\int d^2\vec{k}_\perp\int d^2\vec{k}_\perp^{\,\prime}\\ \times\;& T\big(Y,\vec{k}_\perp,\vec{\Delta}_\perp\big)T\big(Y,\vec{k}_\perp^{\,\prime},\vec{\Delta}_\perp\big)\Bigg\{\Big(z^2+(1-z)^2\Big)\\ \times\;& \left[\frac{(\vec{P}_\perp-\vec{k}_\perp)}{(\vec{P}_\perp-\vec{k}_\perp)^2+\epsilon^2}-\frac{\vec{P}_\perp}{P_\perp^2+\epsilon^2}\right]\cdot\left[\frac{(\vec{P}_\perp-\vec{k}_\perp^{\,\prime})}{(\vec{P}_\perp-\vec{k}_\perp^{\,\prime})^2+\epsilon^2}-\frac{\vec{P}_\perp}{P_\perp^2+\epsilon^2}\right]\\ +\;& m_f^2\left[\frac{1}{(\vec{P}_\perp-\vec{k}_\perp)^2+\epsilon^2}-\frac{1}{P_\perp^2+\epsilon^2}\right]\cdot\left[\frac{1}{(\vec{P}_\perp-\vec{k}_\perp^{\,\prime})^2+\epsilon^2}-\frac{1}{P_\perp^2+\epsilon^2}\right]\Bigg\},\end{aligned} \tag{4.6}$$

and for the longitudinal part

$$\begin{aligned}\frac{d\sigma_L^{\gamma^*p}}{dzd^2\vec{P}_\perp d^2\vec{\Delta}_\perp} &= 2N_c\alpha_{em}4Q^2z^2(1-z)^2\times\sum_f e_f^2\int d^2\vec{k}_\perp\int d^2\vec{k}_\perp^{\,\prime}\\ \times\;& T\big(Y,\vec{k}_\perp,\vec{\Delta}_\perp\big)T\big(Y,\vec{k}_\perp^{\,\prime},\vec{\Delta}_\perp\big)\\ \times\;& \left[\frac{1}{(\vec{P}_\perp-\vec{k}_\perp)^2+\epsilon^2}-\frac{1}{P_\perp^2+\epsilon^2}\right]\cdot\left[\frac{1}{(\vec{P}_\perp-\vec{k}_\perp^{\,\prime})^2+\epsilon^2}-\frac{1}{P_\perp^2+\epsilon^2}\right],\end{aligned} \tag{4.7}$$

where

$$\epsilon^2 = z(1-z)Q^2+m_f^2, \quad m_f = 0.3. \tag{4.8}$$

This approach to calculating matrix elements assumes taking into account the transverse momentum $\vec{\Delta}_\perp$ only through GTMD and the so-called impact factor describing the transition $\gamma^* \to q\bar{q}$. The coupling of quarks with gluons is then taken in the forward direction, as e.g. in Ref. [81]. The subtleties related to the described approximation are not considered this time, as was the case in the previous chapter. However, the formulas from Eq. (4.4) and (4.7) differ e.g. from those in Ref. [81], because they take into account quark masses important for $c\bar{c}$ pair, the production of which is also taken into account in this analysis.

4.1.2 Numerical results

This analysis considers two different kinematic areas corresponding to H1 Ref. [115] and ZEUS [116] collaboration conditions. The experimental cuts imposed by both groups were summarized in Table 4.1.

H1 cuts	ZEUS cuts
$4 < Q^2 < 110\,\mathrm{GeV}^2$	$Q^2 > 25\,\mathrm{GeV}^2$
$x_{\mathbb{P}} < 0.1$	$x_{\mathbb{P}} < 0.01$
$0.05 < y < 0.7$	$0.1 < y < 0.64$
$-1 < \eta_{1,2} < 2.5$	$\eta_{1,2} < 2$
$p_{\perp 1} > 5\,\mathrm{GeV}$	$p_{\perp 1,2} > 2\,\mathrm{GeV}$
$p_{\perp 2} > 4\,\mathrm{GeV}$	$M_{jj} > 5\,\mathrm{GeV}$
$\|t\| < 1\,\mathrm{GeV}^2$	$90 < W_{\gamma p} < 250\,\mathrm{GeV}$

Table 4.1: Cuts used by the H1 and ZEUS collaborations.

The values of the integrated cross-sections for the processes $ep \to dijet\,ep$ in the kinematic mentioned areas are presented in Table 4.2. Moreover, cases in which cuts for the transverse momentum of the jet, and cross-sections for the production of heavier jets $c\bar{c}$ are omitted. The first observation that comes to mind is, that the results obtained from the five models of GTMD considered give completely different results. The MV-BS 2021 parametrization stands out the most and gives much higher values. But for each of the models, the share of $c\bar{c}$ is from 50 to 70% of the dijet cross-section of a light quark. This in most cases still gives a cross-section lower than the experimental values. The exceptions are the MV-IR and MV-BS 2023 GTMD models, which significantly exceed the experiment. Furthermore, the cases taken into account without cuts on $p_{\perp\,jet}$ show a several-fold increase in the total cross-sections.

GTMD approach	H1, light $q\bar{q}$	H1, $ep \to c\bar{c}$	H1 no $p_{\perp 1,2}$ cuts
GBW	26.35	19.91	10900.86
MPM	147.94	108.26	10151.00
MV-BS 2021	404.06	269.75	10999.73
MV-BS 2023	288.34	189.74	6685.82
KT	21.29	15.20	5957.65
MV-IR	243.20	155.21	11784.75
DATA	254		-

GTMD approach	ZEUS, light $q\bar{q}$	ZEUS, $ep \to c\bar{c}$	ZEUS, no $p_{\perp 1,2}$ cuts
GBW	13.57	6.67	337.11
MPM	43.61	20.47	313.17
MV-BS 2021	1346.11	624.55	3117.95
MV-BS 2023	732.15	348.40	1510.33
KT	12.57	5.67	52.60
MV-IR	37.83	17.62	91.18
DATA	72		-

Table 4.2: Total cross-section for the dijets production in electron-proton collision in pb for H1 and ZEUS conditions and different model approaches.

Thanks to a thorough analysis of the H1 and ZEUS collaboration, several cross-section distributions in various kinematic variables are related to experimental data. The first is the distribution in photon virtuality shown in Fig. 4.3, the shape of which generally agrees with the distribution of data from H1. There are however significant differences in the normalization of individual models, also visible in the case of ZEUS kinematics, which corresponds to the results from Table 4.2. The largest contribution comes from the MV-BS models but it turns out to overestimate the measured cross-sections over almost the entire Q^2 range for the MV-BS 2021 model, while the MV-BS 2023 parametrization describes the data very well. In the case of cuts analogous to ZEUS, this model gives results that exceed other GTMDs by two orders of magnitude, which are taking place at all of the considered distributions in that kinematic.

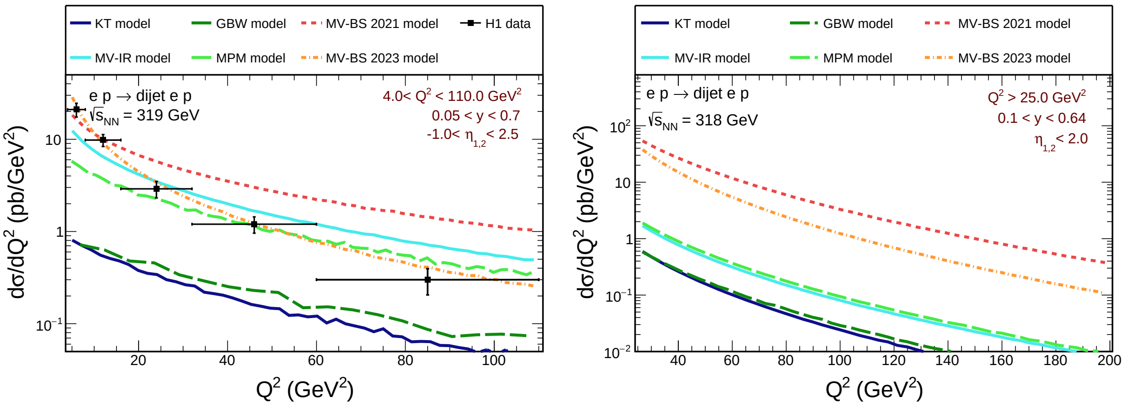

Figure 4.3: Photon virtuality dependence of the cross-section for the diffractive light dijet production for H1(left) and ZEUS (right) kinematic for different GTMDs.

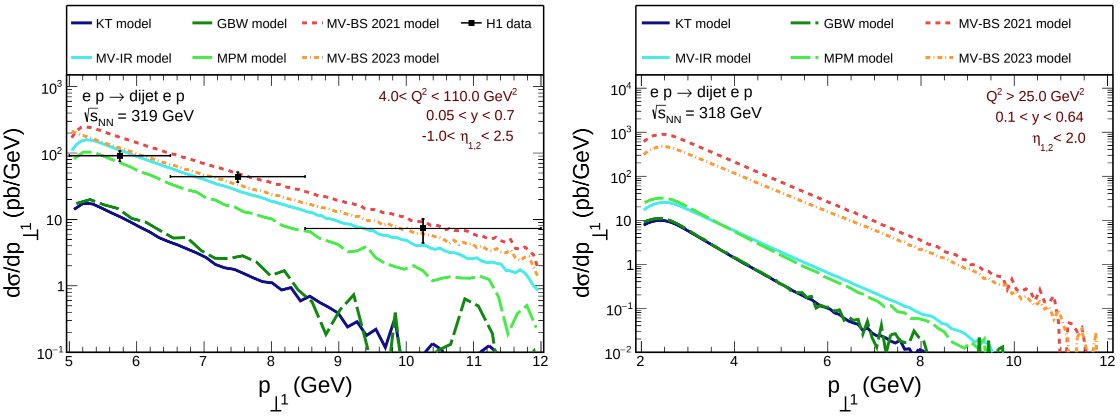

Figure 4.4: Jet transverse momentum dependence of the cross-section for the diffractive light dijet production for H1(left) and ZEUS (right) kinematic for different GTMDs.

A similar consistency in the shape of the curves is visible in the distribution of the transverse momenta of the jet. In this case, however, the MV-BS models do not exceed the values corresponding to the experimental data. Similarly to the previous distribution, the results obtained from GBW and KT GTMDs give similar values, much lower than MPM and MV-IR GTMDs, which also show great similarity with each other, this tendency persists for all the considered distributions.

The t Mandelstam distribution from Fig. 4.5, shows the first differences between the shape of the MV-BS distributions and the other GTMDs, which in this case refers to the slope of the line. But again it seems that those models describe the data well, as well as the distributions that overlap with them corresponding to the MPM and MV-IR models.

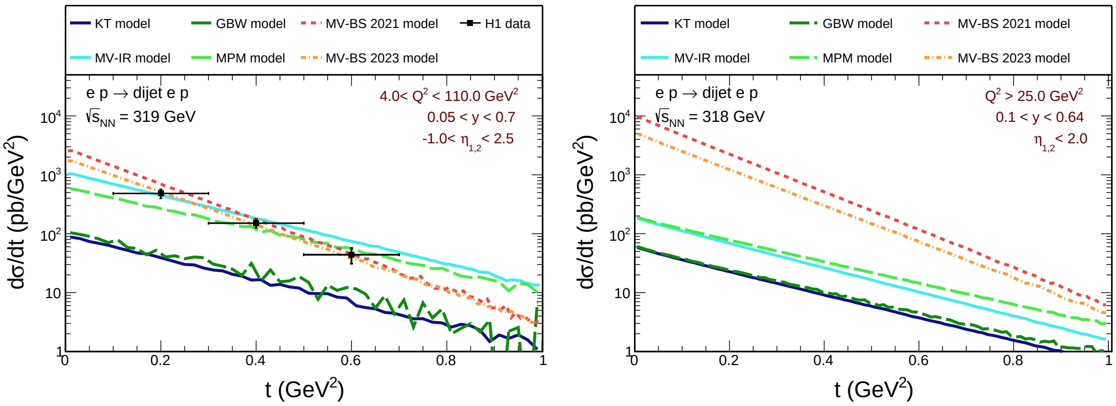

Figure 4.5: Mandelstam t dependence of the cross-section for the diffractive light dijet production for H1(left) and ZEUS (right) kinematic for different GTMDs.

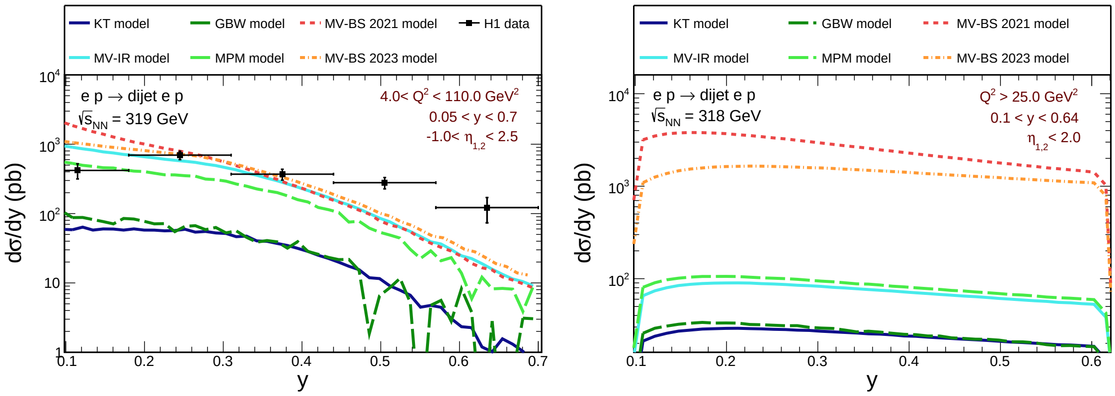

Figure 4.6: Inelasticity dependence of the cross-section for the diffractive light dijet production for H1(left) and ZEUS (right) kinematic for different GTMDs.

The dependence on inelasticity shown in Fig. 4.6 is not fully reproduced correctly by the tested models. Although the overall shape of all distributions is similar, there is a slightly too large drop in the tail of large y, and the results corresponding to the MV-IR and MV-BS models slightly overestimate those for small inelasticity.

This positive impression regarding the description of data is disturbed in Fig. 4.7, where the distribution in $\log_{10} x_{\mathbb{P}}$ is presented. Note that $\Delta Y \equiv \ln(1/x_{\mathbb{P}})$ essentially corresponds to the rapidity difference between the proton, and the diffraction system. In this case both MV-BS models, the MV-IR and MPM model significantly outperform the results of the H1 experiment, contradicting the data. It is also worth mentioning that the kinematics of H1 covers quite large $x_{\mathbb{P}} > 0.01$, so we should not expect the dominance

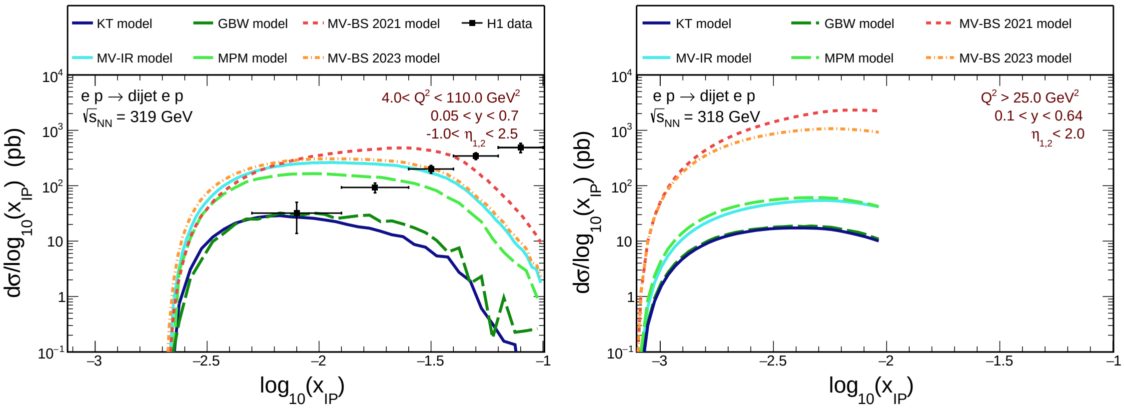

Figure 4.7: $x_{\mathbb{P}}$ dependence of the cross-section for the diffractive light dijet production for H1(left) and ZEUS (right) kinematic for different GTMDs.

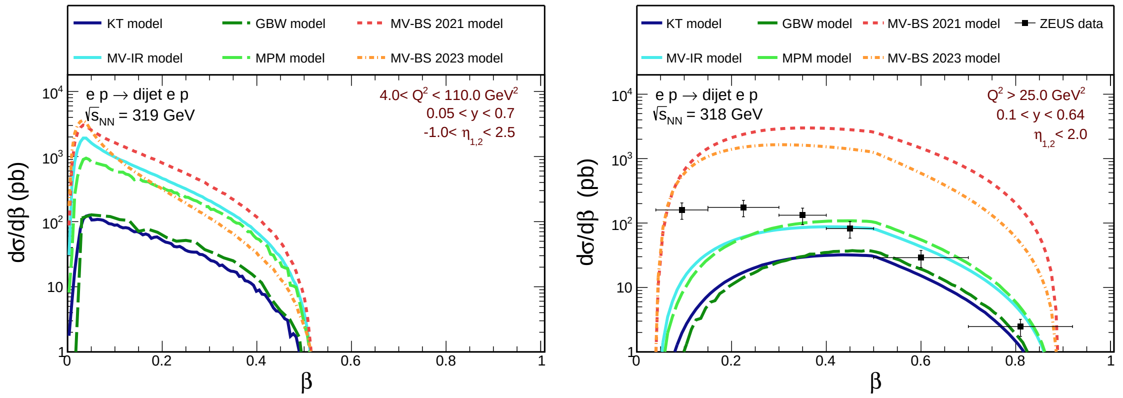

Figure 4.8: β dependence of the cross-section for the diffractive light dijet production for H1(left) and ZEUS (right) kinematic for different GTMDs.

of pomeron exchange and the correct description of all experimental data using the dipole approach, but rather the contribution of $q\bar{q}$ described by secondary Reggeons, as e.g. in Ref. [124]. The dipole approach should rather correctly describe the ZEUS data where the kinematic region covers only small $x_{\mathbb{P}} < 0.01$ and there the contribution of pomeron or gluon GTMD should be appropriate.

Reference to the data from ZEUS is visible in Fig. 4.8, which maps the distributions in

$$\beta = \frac{Q^2}{Q^2 + M_{jj}^2}\,, \tag{4.9}$$

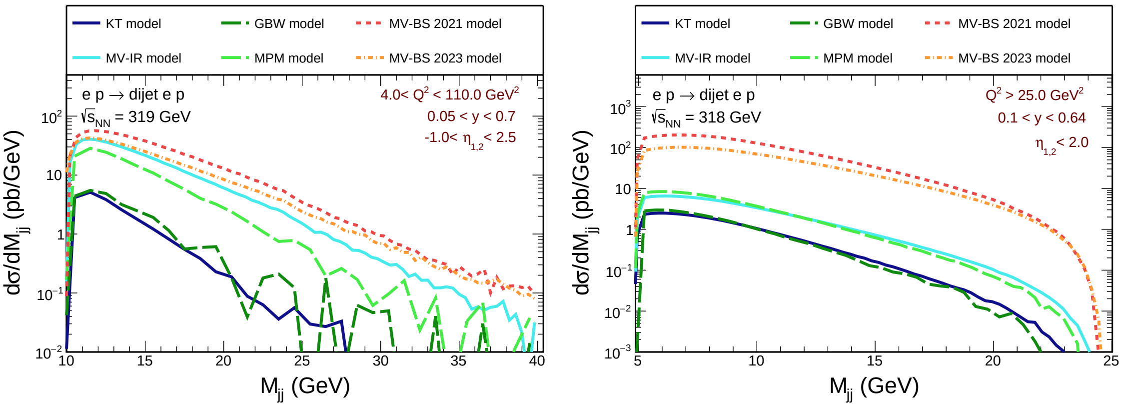

Figure 4.9: Dijet invariant mass dependence of the cross-section for the diffractive light dijet production for H1(left) and ZEUS (right) kinematic for different GTMDs.

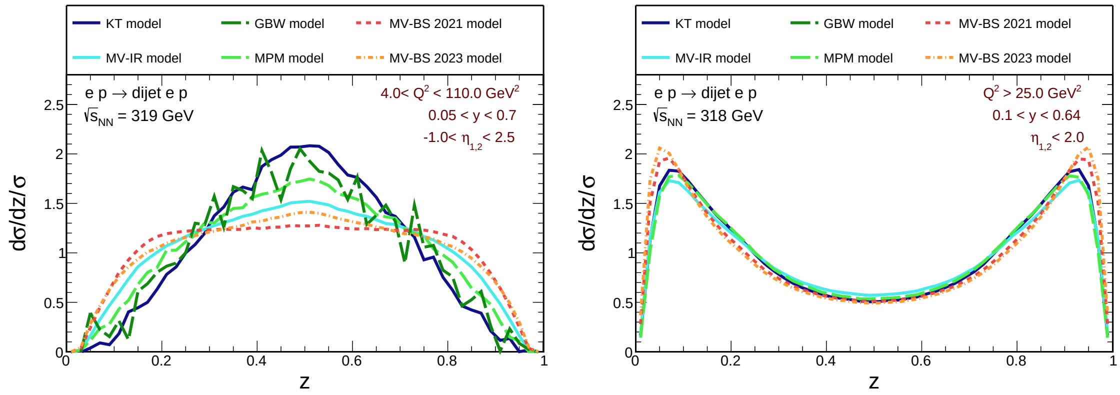

Figure 4.10: z dependence of the cross-section for the diffractive light dijet production for H1(left) and ZEUS (right) kinematic for different GTMDs. Note the normalization

where in this case

$$M_{jj}^2 = \frac{p_{\perp 1}^2 + m_q^2}{z} + \frac{p_{\perp 2}^2 + m_q^2}{1-z} - \Delta_\perp^2. \tag{4.10}$$

Just as the results corresponding to the H1 kinematics are quite similar to each other, the tendency of much higher cross-section values of the MV-BS models with the other approaches is also maintained in the case of these distributions.This effect translates into drastically exaggerated results of those models concerning the experiment. As with the distribution in $x_{\mathbb{P}}$, this situation leads to the conclusion that the MV-BS 2021 and 2023 GTMD parametrizations are artificially inflated to describe the H1 data, in which gluons are probably not dominant. Note that even for ZEUS data, it would probably be inappro-

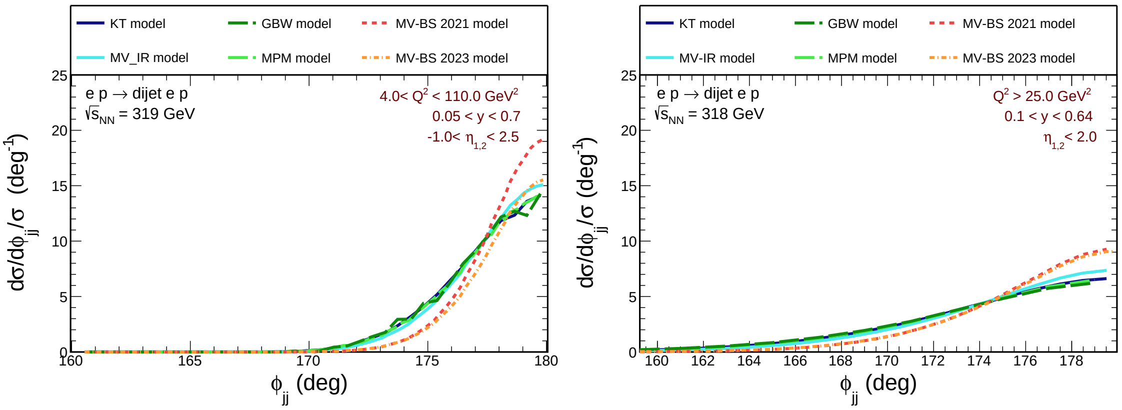

Figure 4.11: Azimuthal angle between produced jets dependence of the cross-section for the diffractive light dijet production for H1(left) and ZEUS (right) kinematic for different GTMDs. Notice the normalization.

priate to fit GTMD to the data using this approach. The reason for this is the significant three-part contribution $q\bar{q}g$ in the region of small β (see e.g. Ref. [125]). Therefore, it seems that the KT and GBW models are the most realistic.

The shapes of the distributions in M_{jj} calculated according to Eq. 4.10, shown in Fig. 4.9, are consistent with the trends visible in the previous relations for both kinematic ranges. Despite imposing cuts on $M_{jj} > 5.0\,\mathrm{GeV}$ in the ZEUS kinematics, these masses are smaller than those available in H1, where additional cutting is not required due to the influence of the remaining kinematic conditions. Also, the upper limit of the obtained masses dijet is in this case twice as high.

A completely different behavior of individual distributions is visible in the z variable from Fig. 4.10, where for H1 kinematics the maximum appears at $z = 0.5$ for all GTMDs models used, except for MV-BS models whose distributions are almost flat in the range of $0.1 - 0.9$. The value of the peak corresponding to the remaining approaches differs significantly between parametrizations. This contrasts with the ZEUS kinematics, where at $z = 0.5$ the minimum of the distributions of all models is visible, and the peaks appears at the boundaries of the considered area. In this case, moreover, the differences between used GTMDs parametrizations are small, which is related to the normalization of the visible distributions to the cross-section.

For completeness, angular distributions were also considered. The first is the distribution in the ϕ_{jj} angle (see Fig. 4.11), where a high peak at $\phi_{jj} = 180\ \mathrm{deg}$ is visible in the azimuthal angle distribution between the jets produced for H1 kinematics, indicating

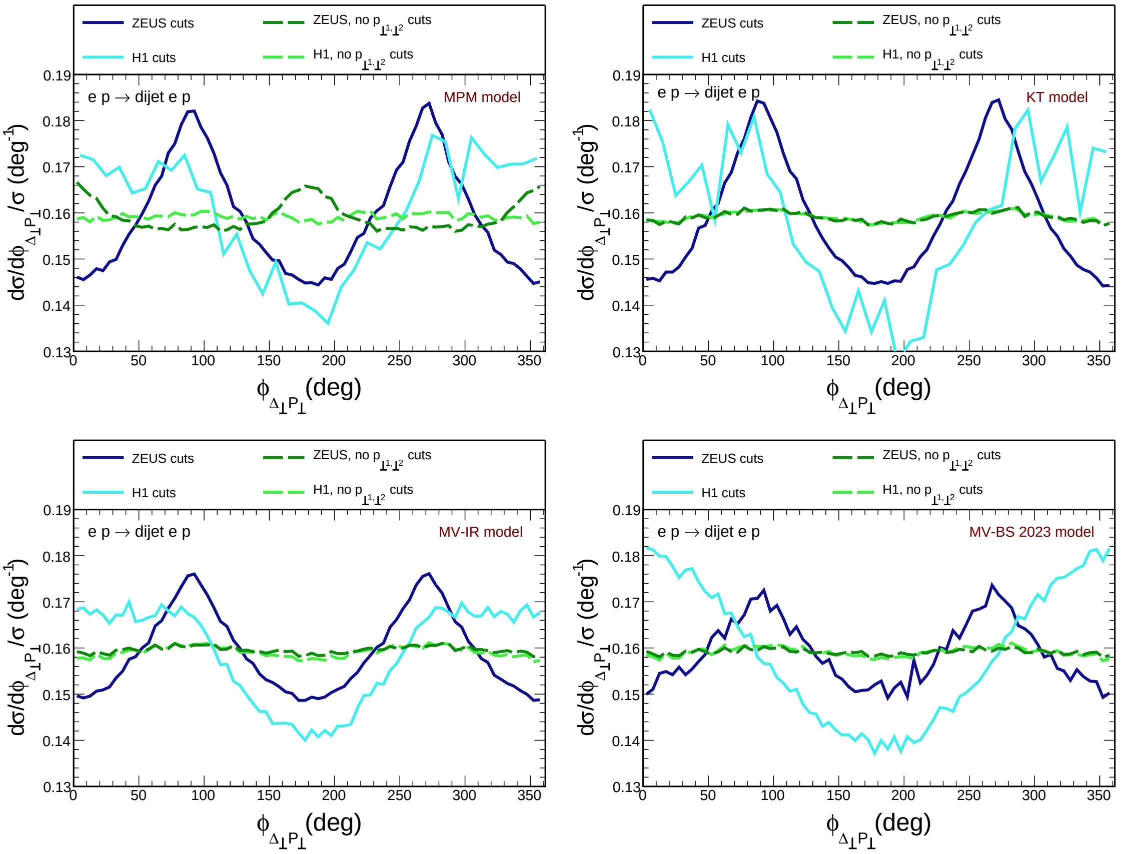

Figure 4.12: Energy of the photon-proton system Azimuthal angle ϕ between $\vec{P}_\perp$ and $\vec{\Delta}_\perp$ dependence of the cross-section for the diffractive light dijet production for H1 and ZEUS kinematic for different GTMDs. Notice the normalization.

their opposite orientation, relative to each other. This effect is much smaller in the case of ZEUS kinematics. This again may be a sign of the contribution of $q\bar{q}g$ final states.

The second angular distribution concerns the azimuthal angle between the sum and the difference of the transverse momentum of the produced pair and is shown in Fig. 4.12. This is a distribution analogous to the angular correlations presented in the previous chapter for the production of $c\bar{c}$ in collisions pA (from Fig. 3.11). Interestingly, despite the lack of elliptical contributions, azimuthal correlations are predicted for the jets observed at HERA. In addition to the distributions resulting from the kinematics of the H1 and ZEUS collaboration, which show the existence of such a relation, there are also distributions, that do not take into account cuts to the transverse momentum of the jet. Visible correlation proves that the observed oscillations originate mainly from the used cuts. However, it does not exclude the occurrence of additional correlations after taking into account elliptic contributions, which makes this effect easily misinterpreted.

To obtain a complete picture, the transverse and longitudinal components were also presented separately in the example of MPM and KT GTMDs. The photon virtuality distributions visible in Fig. 4.13 are consistent with the predictions for H1 kinematics, while in the case of ZEUS, the entire considered area is dominated by the transverse component. This surprising result, however, is related to the distributions of these components as a function of z presented in Fig. 4.14. For the H1 case, both components of the reflected models are at a similar level, but after changing the kinematics, a significant dominance of the transverse components is visible. It is also worth noting that the maxima appearing in the distribution of cross-sections as a function of z for the ZEUS kinematics reflect the distributions in Fig. 4.10 very well, while the high peaks around $z = 0.5$ for the H1 kinematics presented in this figure result from a normalization of this distribution. This conclusion is related to the fact, that without the normalization, the peak strengthening is much less pronounced, which is the case in Fig. 4.14.

An additional aspect is the overestimation of the distributions predicted by the MV-BS model in some variables, which is why it was also decided to consider different values of the parameter χ from Eq. 4.1. The examples of dependence on the variables z and t are collected in Fig. 4.15 in the case of the MV-BS 2021 model. Taking into account four different values of this factor showed, that its value only affects the normalization of the cross-section, without changing the shape of the curves. Choosing a suitably small value of $\chi = 0.25$ allowed for the correct mapping of data from ZEUS, but also in this case it would be necessary to test the correctness of the selected value. As can be seen on the right

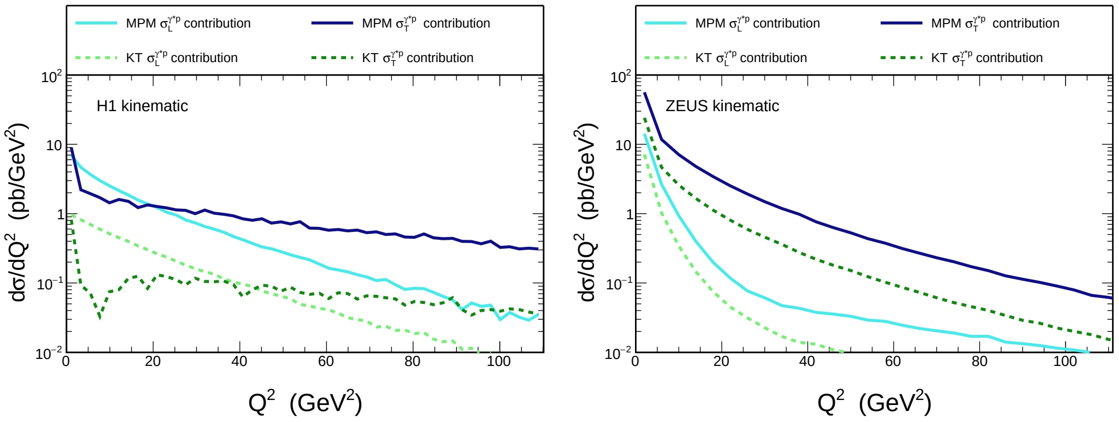

Figure 4.13: Photon virtuality dependence of the cross-section for the diffractive light dijet production for H1(left) and ZEUS (right) kinematic for the transverse and longitudinal parts for MPM and KT GTMDs.

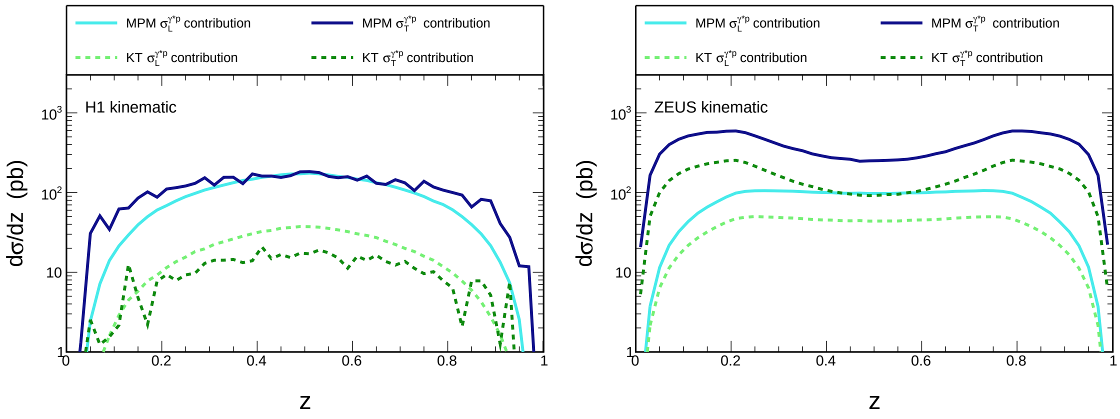

Figure 4.14: z dependence of the cross-section for the diffractive light dijet production for H1 (left) and ZEUS (right) kinematic for the transverse and longitudinal parts for MPM and KT GTMDs.

side of Fig. 4.15, the slope of this distribution still deviates from the other GTMDs, which suggests that other changes may be necessary to enable its correctly predict experiments.

So far, the production of only light jets has been considered, as in the analysis from Ref. [81]. The contribution from the $c\bar{c}$ pairs is presented in the cross-section distributions in the β and Q^2 variables in Figs 4.16 and 4.17, respectively. These distributions show that considering the production of these additional quarks may result in the increase of the cross-section by as much as 50% for the ZEUS kinematics and 70% for the H1 kinematics. When applying the KT approach to GTMD, which was considered probably

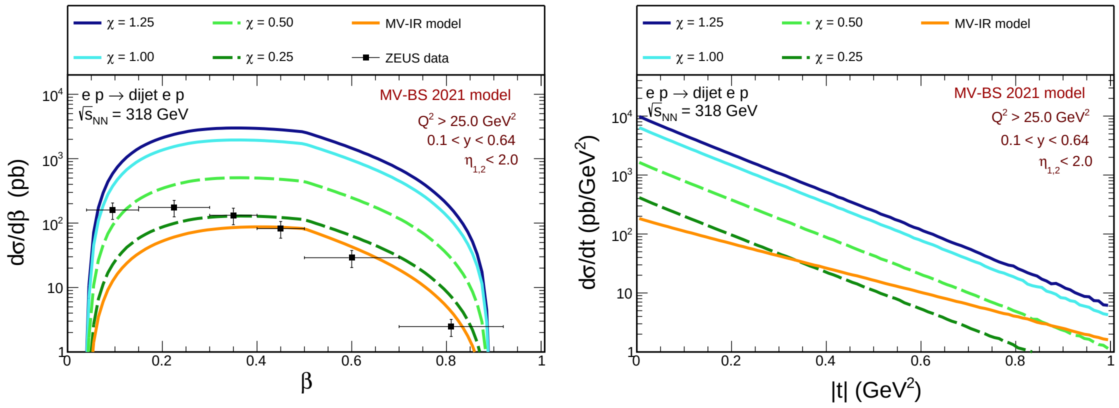

Figure 4.15: β and t dependence of the cross-section for the diffractive light dijet production for the ZEUS kinematic for the MV-BS GTMD with different χ values.

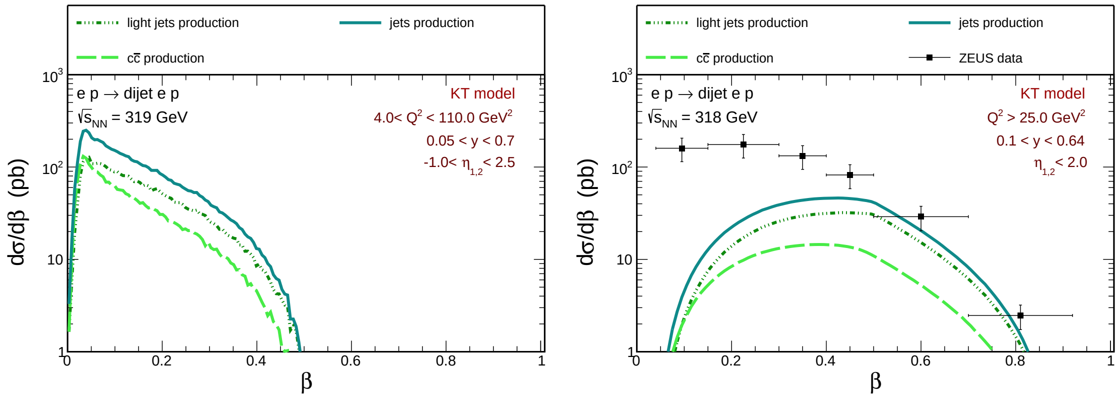

Figure 4.16: β dependence of the cross-section for the diffractive light+charm dijets production for H1(left) and ZEUS (right) kinematic for the KT GTMD.

correct during the analysis, such an increase in the cross-section value does not result in exceeding the experimental data, and in fact, there is still a place to take into account other mechanisms. However, a thorough analysis of this type of production is beyond the scope of this thesis, similar to the consideration of Sudakov effects (see e.g. [126]), and hadronization which also requires further research.

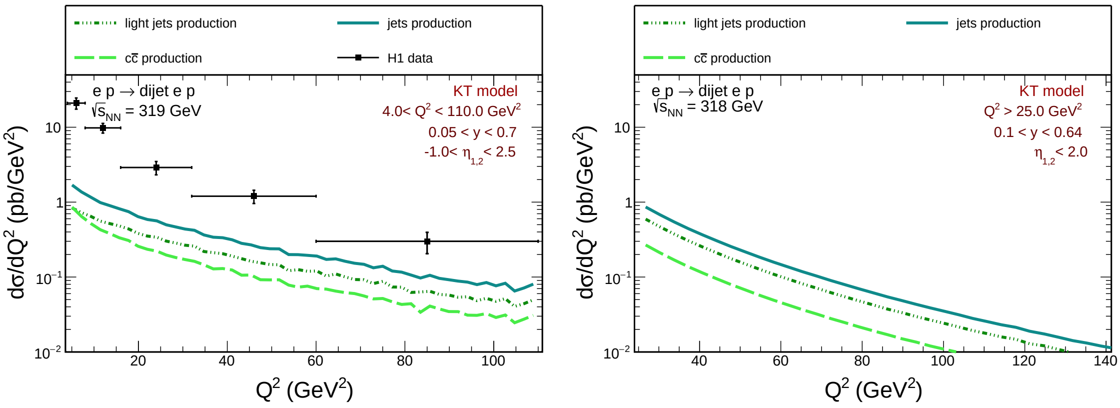

Figure 4.17: Photon virtuality dependence of the cross-section for the diffractive light+charm dijets production for H1(left) and ZEUS (right) kinematic for the KT GTMD.

4.2 EIC predictions

Previous comparison of GTMD models and reference to experimental results allowed determine their probable correctness. Further information about them may be provided by experiments that will be performed in the Electron-Ion Collider, which is currently under construction. Due to the fact, that the construction is not yet completed, the exact parameters of the detectors are not yet fully known. Nevertheless, the essence is to create theoretical predictions enabling, among other things, determining the feasibility of performing individual experiments. That is why in the literature different approaches to this problem by imposing different cuts are taken (see e.g. Refs [127, 128]).

According to the guidelines in Ref. [129, 130], the diffractive production of dijets in electron-proton collisions analogous to those in Fig. 4.1 on this accelerator includes the following conditions:

- the collision energy equals $\sqrt{s} = 141\,\mathrm{GeV}$: electron energy - $18.8\,\mathrm{GeV}$, proton energy - $275\,\mathrm{GeV}$;
- the jet transverse momentum $p_{\perp\,1,2} > 5.0\,\mathrm{GeV}$;
- inelasticity range: $0.01 < y < 0.95$;
- pseudorapidity range: $-3.5 < \eta < 3.5$;
- photon virtuality range is: $5.0 < Q^2 < 500.0\,\mathrm{GeV}^2$ (the assumption).

These calculations were performed for the five different GTMD models presented earlier. It was decided to abandon the use of the x_{Bj}-independent MV-BS 2021 model and use only the MV-BS 2023 model from Ref. [120]. The calculation results are summarized in Table 4.3 taking into account the total cross-sections for the mentioned diffractive dijet production.

As in the case of HERA kinematics, the smallest cross-sections are obtained using KT and GBW models of the GTMD. However, it turns out that in this case, the MV-BS 2023 model gives a smaller cross-section than the MV-IR, although the result is still more than twice as large as in the case of the KT. The differences resulting from Table 4.3 are confirmed in all the drawings below of differential cross-sections in individual kinematic variables.

GTMD model	$\sigma\ (pb)$
MPM	77.89
GBW	10.93
KT	6.53
MV-BS 2023	136.49
MV-IR	144.15

Table 4.3: Total cross-section for EIC kinematics and different model approaches.

The first one is visible in Fig. 4.18 and shows the distributions in the jet transverse momentum, where some minor statistical problems, especially with the GBW, KT, and MPM models, can be noted. They are associated with a very steep decrease in the cross-section value with an increase of $p_{\perp 1}$ reaching up to six orders of magnitude. Therefore, it may be meaningful to measure in the range of transverse momenta smaller than $12\,\mathrm{GeV}$, where the decrease is more visible.

In Fig. 4.19 which presents the distribution in the diquark transverse momenta it is noticeable, that the area of the transverse momentum of the produced pair covers only values smaller than $\Delta_\perp \sim 1.0\,\mathrm{GeV}$, also for models giving much higher values of differential cross-sections. It may suggest that, as in the case of proton-nucleus collisions, two-photon processes may also have a significant impact. However, this is beyond the scope of this analysis and should be examined in future research.

Fig. 4.20 shows the distributions in the photon virtuality. Although a very wide range of photon virtualities was taken into account, as in $p_{\perp 1}$, a decrease in the differential

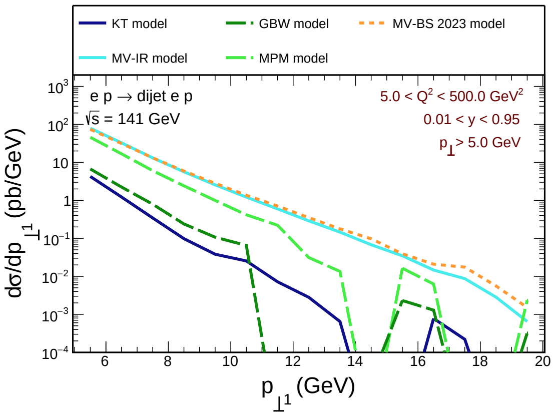

Figure 4.18: Jet transverse momentum dependence of the cross-section for diffractive light dijet production for EIC and kinematic for different GTMDs.

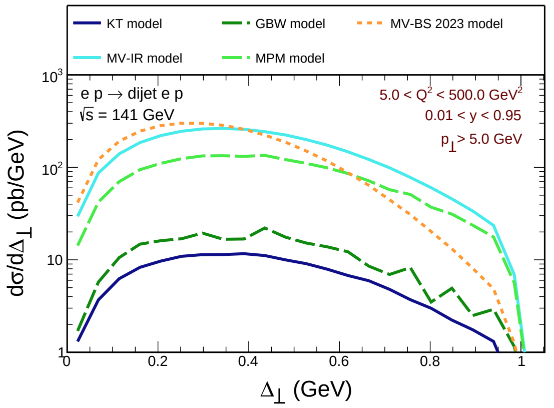

Figure 4.19: Diquark transverse momentum dependence of the cross-section for diffractive light dijet production for EIC and kinematic for different GTMDs.

cross-section values by several orders of magnitude is noticeable, and is similar to the HERA kinematics including its conditions. It may suggest that it would be worth limiting this range during an experiment. Fig. 4.21 shows the dependencies of the differential cross-sections as functions of the Mandelstam variable t. Its behavior is analogous to the difference in the slope of the lines from H1 kinematics, and the slope of the MV-BS 2023 model results are different from the other models.

In all three functions described above, all models except MV-BS 2023 have almost identical shapes and differ only in normalization. However, similarly to the previous calculations, the GBW and KT models give similar results, which are an order of magnitude lower than those of the GTMD MPM and MV-IR models comparable to MV-BS 2023.

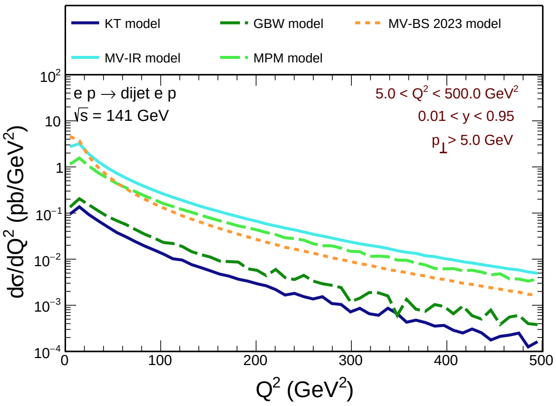

Figure 4.20: Photon virtuality dependence of the cross-section for diffractive light dijet production for EIC and kinematic for different GTMDs.

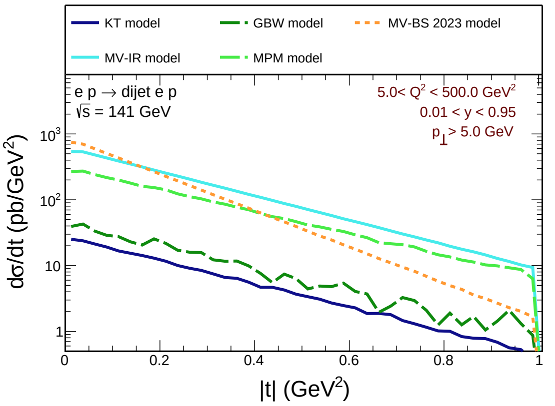

Figure 4.21: Mandelstam t dependence of the cross-section for diffractive light dijet production for EIC and kinematic for different GTMDs.

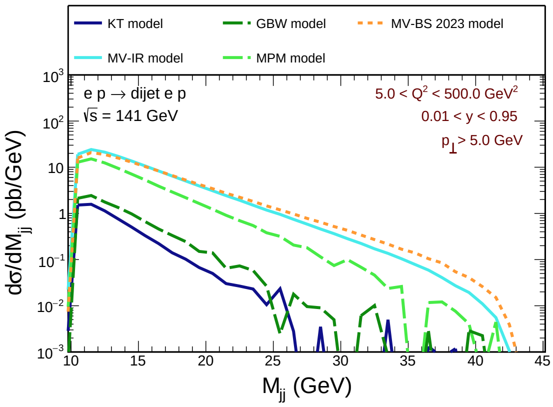

Figure 4.22: Invariant mass of dijets dependence of the cross-section for diffractive light dijet production for EIC and kinematic for different GTMDs.

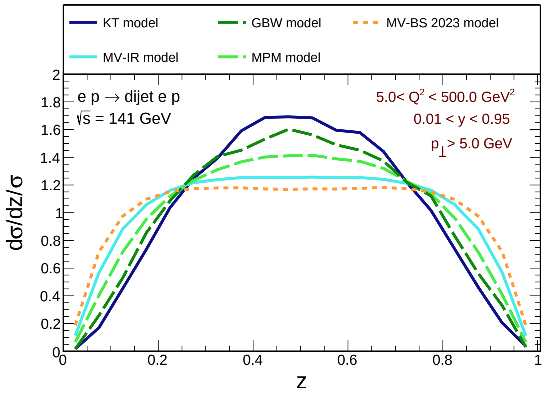

Figure 4.23: z dependence of the cross-section for diffractive light dijet production for EIC and kinematic for different GTMDs. Notice the normalization.

The distribution in the invariant mass of the produced pair from Fig.4.22 covers the area from $10\,\mathrm{GeV}$ to $45\,\mathrm{GeV}$ which, like the distribution in z, again is similar to that from H1 kinematics. Moreover, in the M_{ll} function, the statistical fluctuations are more visible in the KT and GBW GTMD models. It should be mentioned that the fluctuations visible from this variable also appear in the calculations corresponding to the H1 kinematics. Their elimination was unsuccessful despite the increase in measurement statistics, most likely due to the decrease in the cross-section, and use of wider ranges of other variables. The shape of the curves from the distributions in Fig. 4.23 refers to the behavior of transverse and longitudinal inputs in this variable, and the photon virtuality, as demonstrated in the previous section.

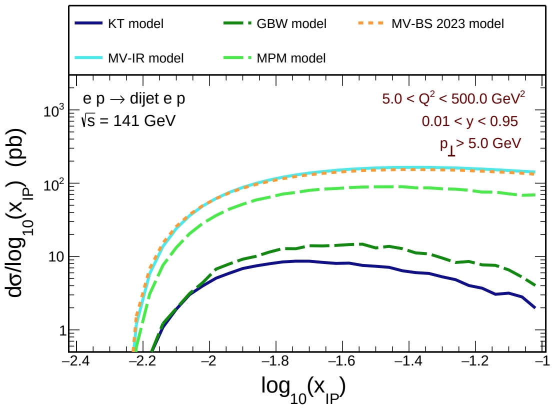

Figure 4.24: Pomeron-x dependence of the cross-section for diffractive light dijet production for EIC and kinematic for different GTMDs.

The last distribution is the $x_{\mathbb{P}}$ dependent one seen in Fig. 4.24. This distribution reveals a much smaller contribution from small $x_{\mathbb{P}}$, which is related to the dominance of the $q\bar{q}$ exchanges described by the secondary Reggeons at the larger x_{IP}.

In general, the results for EIC are therefore analogous to the quite similar kinematics used by the H1 collaboration (hence not all distributions are presented) however, the cross-section values and, consequently, the contribution of diffractive dijet production processes in electron-proton collisions at the EIC accelerator is significantly smaller. However, the greater luminosity of this accelerator may allow for a more accurate description of GTMD, also based on the study of the color dipole approach.

Chapter 5

Summary and outlook

This work covers a wide range of studies on the properties of hadrons (especially protons), including processes initiated by the exchange of one or two photons.

The first issues discussed were lepton production processes in proton-proton and proton-nucleus collisions studied in the kinematics of the LHC. For their analysis based on the transverse factorization approach, four different models of three-dimensional proton structure functions were used in relation to the latest experiments taking into account the measurement of the proton after the collision. The results of proton-proton collisions performed by the ATLAS collaboration, despite not superimposing all the cuts they used, are explained, and potentially interesting cases that should be investigated experimentally are predicted.
In the case of proton-nucleus collisions, reference was made to the analyses carried out by the ALICE collaboration, where it is suggested to impose cuts in subsequent experiments allowing the study of exclusive processes for the production of electron-positron pairs due to their small contribution but interesting results in the production of electron-positron pairs. These studies also allowed for a comparison of individual models and the identification of problems present in particular in FFJLM resulting from the inadequacy of this model to such wide kinematics.

In the case of two-photon processes, an analogous analysis was also carried out using the SuperChic generator used by the experimentators, which allows for the determination of the gap survival factor, and thus a proposal was presented to eliminate additional processes accompanying the collision, which should be taken into account when describing the data.

The next step in the research was to describe processes involving photon-pomeron "fusion" At this stage, diffractive processes of dijet production in proton-nucleus collisions in the color dipole approach were taken into account.
One of the goals in this case was to compare the GBW, MPM, and KT models popular in the literature with the new MV-IR and HHU models not previously compared to experimental data. The first important aspect, in this case, is the need to use the Gaussian cutoff function, which assumes the presence of the ε_r parameter, the value of which has a significant impact on the final calculation results and has not yet been confirmed experimentally. Moreover, this analysis does not take into account the analogous cutoff function in relation to the Fourier transform from the impact parameter space to the transverse momenta, because its importance is much smaller. However, in the case of thorough analyses, the differences resulting from its application could be significant. Therefore, using cutoff functions for the Fourier transform from the impact parameter should also be analyzed.

However, the main goal of this project was to demonstrate the angular correlations resulting from taking into account the second harmonics of the Fourier series expansion of the dipole amplitude. The contribution of this function is much smaller than that of the isotropic part, but it was possible to demonstrate the existence of a trigonometric relationship in the azimuthal angle. Moreover, the GBW model also allowed for the observation of additional oscillations resulting from the inclusion of a larger number of harmonics of the dipole amplitude development.

Furthermore, an analysis of dijet production in these collisions was performed, taking into account the $\gamma\gamma$ exchange mechanism, which showed a much smaller decrease in the contribution of these processes and, consequently, similar cross-section values in the areas of larger transverse momenta and their dominance at $\Delta_\perp > 1.5\,\mathrm{GeV}$. Seeing the results of experiments allows for verifying the correctness of the analysis and confirms the results obtained.

The last stage of this thesis was to relate the results obtained based on available GTMD models in the color dipole approach to experimental data corresponding to the kinematics of the H1 and ZEUS collaboration and to analyze the hypothetical experiment carried out at EIC.

The former aspect made it possible to highlight problems with the data description by the MV-IR, MV-BS 2021, MV-BS 2023, and MPM models in this kinematic area. This analysis did involve the contribution of elliptical elements, although oscillations in the azimuthal angle were observed, indicating that they resulted from geometric correlations.

However, this does not exclude the occurrence of additional oscillations resulting from the inclusion of this harmonic.

It should be mentioned that the MV-BS models take into account additional parameters, affecting primarily the height of the differential distributions in individual variables, therefore it is probable that these models will be adapted to experimental data. However, this would also require a thorough analysis of the production of $q\bar{q}$ described by secondary Reggeons, which dominates for large $x_{\mathbb{P}}$, and $q\bar{q}g$ contribution which is important for small values of β.

Due to the fact, that the parameters of the experiments that will be conducted at the EIC are not yet known, quite wide cuts have been imposed on such a hypothetical experiment, which contributed to a slight deterioration of the obtained results related to the statistics of the calculations. However, the region corresponding to the EIC turned out to be quite close to the H1 kinematics but the much larger luminosity will contribute to a more thorough examination of the GTMD models based on larger amounts of experimental data available in the future.

Appendix A

Total cross-section for the γp-collision for all four types of photon-pomeron exchange

This appendix is an extension to Chapters 3 and 4.

To get the convolution form of the cross-section for the diffractive $\gamma p \to Q\bar{Q}$ it is useful to introduce the amplitude related to the gluon density matrix from Eq. 3.17 to the general form of the cross-section for the $\gamma p \to Q\bar{Q}$ diffractive processes in the color dipole approach from Eq. 3.14, which results:

$$\begin{aligned}
\frac{d\sigma(\gamma^*_{\lambda_\gamma} p \to Q\bar{Q}p; s_{\gamma p})}{dz d^2\vec{P}_\perp d^2\vec{\Delta}_\perp} &= \overline{\sum_{\lambda_\gamma,\lambda,\bar{\lambda}}} \Big| \int \frac{d^2\vec{b}_\perp d^2\vec{r}_\perp}{(2\pi)^2} e^{-i\vec{\Delta}_\perp\cdot\vec{b}_\perp} e^{-i\vec{P}_\perp\cdot\vec{r}_\perp} \int d^2\vec{q}_\perp d^2\vec{k}_\perp \\
&\times\ f\Big(Y, \frac{\vec{q}_\perp}{2} + \vec{k}_\perp, \frac{\vec{q}_\perp}{2} - \vec{k}_\perp\Big) e^{i\vec{q}_\perp\cdot\vec{b}_\perp} \\
&\times\ \Big\{ e^{i\frac{\vec{q}_\perp}{2}\cdot\vec{r}_\perp} + e^{-i\frac{\vec{q}_\perp}{2}\cdot\vec{r}_\perp} - e^{i\vec{k}_\perp\cdot\vec{r}_\perp} - e^{-i\vec{k}_\perp\cdot\vec{r}_\perp} \Big\} \\
&\times\ \Psi^{\lambda_\gamma}_{\lambda\bar{\lambda}}(z, \vec{r}_\perp) \Big|^2 .
\end{aligned} \tag{A.1}$$

This equation can be then rewritten

$$\begin{aligned}\frac{d\sigma(\gamma^*_{\lambda_\gamma}p \to Q\bar{Q}p; s_{\gamma p})}{dz d^2\vec{P}_\perp d^2\vec{\Delta}_\perp} &= \overline{\sum_{\lambda_\gamma,\lambda,\bar{\lambda}}}\Bigg| \int \frac{d^2\vec{b}_\perp}{(2\pi)^2} e^{i(\vec{q}-\vec{\Delta}_\perp)\vec{b}} e^{-i\vec{q}\vec{b}_\perp} \int d^2\vec{q}_\perp d^2\vec{k}_\perp \frac{d^2\vec{l}}{(2\pi)^2} \\ &\times\ f\Big(Y, \frac{\vec{q}_\perp}{2} + \vec{k}_\perp, \frac{\vec{q}_\perp}{2} - \vec{k}_\perp\Big) \Psi^{\lambda_\gamma}_{\lambda\bar{\lambda}}(z, \vec{l}\,) \\ &\times\ \Bigg\{ e^{i(\frac{\vec{q}}{2} - \vec{P}_\perp + \vec{l}\,)\cdot \vec{r_\perp}} + e^{i(\frac{\vec{q}}{2} + \vec{P}_\perp - \vec{l}\,)\cdot \vec{r_\perp}} \\ &-\ e^{-i(\vec{k} - \vec{P_\perp} + \vec{l}\,)\cdot \vec{r_\perp}} - e^{-i(\vec{k} - \vec{P_\perp} - \vec{l}\,)\cdot \vec{r_\perp}} \Bigg\} \Bigg|^2, \end{aligned} \tag{A.2}$$

and including dependence

$$\int \frac{d^2\vec{b_\perp}}{(2\pi)^2} e^{i(\vec{q} - \vec{\Delta_\perp})\vec{b}_\perp} = \delta^{(2)}(\vec{q} - \vec{\Delta_\perp}). \tag{A.3}$$

It can be simplified to

$$\begin{aligned}\frac{d\sigma(\gamma^*_{\lambda_\gamma}p \to Q\bar{Q}p; s_{\gamma p})}{dz d^2\vec{P}_\perp d^2\vec{\Delta}_\perp} &= \overline{\sum_{\lambda_\gamma,\lambda,\bar{\lambda}}}\Bigg| \int d^2\vec{q}_\perp d^2\vec{k}_\perp \frac{d^2\vec{l}}{(2\pi)^2} \\ &\times\ f\Big(Y, \frac{\vec{\Delta}_\perp}{2} + \vec{k}_\perp, \frac{\vec{q}_\perp}{2} - \vec{k}_\perp\Big) \Psi^{\lambda_\gamma}_{\lambda\bar{\lambda}}(z, \vec{l}\,) \\ &\times\ (2\pi)^2 \cdot \Bigg\{ \delta^{(2)}\Big(\frac{\vec{\Delta}}{2} - \vec{P} + \vec{l}\,\Big) + \delta^{(2)}\Big(\frac{\vec{\Delta}}{2} + \vec{P} - \vec{l}\,\Big) \\ &-\ \delta^{(2)}\Big(\frac{\vec{k}_\perp}{2} - \vec{P} + \vec{l}\,\Big) - \delta^{(2)}\Big(\frac{\vec{k}_\perp}{2} + \vec{P} - \vec{l}\,\Big) \Bigg\} \Bigg|^2. \end{aligned} \tag{A.4}$$

After integrating over $\vec{q_\perp}$there is

$$\begin{aligned}\frac{d\sigma(\gamma^*_{\lambda_\gamma}p \to Q\bar{Q}p; s_{\gamma p})}{dz d^2\vec{P}_\perp d^2\vec{\Delta}_\perp} &= \overline{\sum_{\lambda_\gamma,\lambda,\bar{\lambda}}}\Bigg| \int d^2\vec{k}_\perp d^2\vec{l} \\ &\times\ f\Big(Y, \frac{\vec{\Delta}_\perp}{2} + \vec{k}_\perp, \frac{\vec{\Delta}_\perp}{2} - \vec{k}_\perp\Big) \Psi^{\lambda_\gamma}_{\lambda\bar{\lambda}}(z, \vec{l}\,) \\ &\times\ \Bigg\{ \delta^{(2)}\Big(\frac{\vec{\Delta}}{2} - \vec{P} + \vec{l}\,\Big) + \delta^{(2)}\Big(\frac{\vec{\Delta}}{2} + \vec{P} - \vec{l}\,\Big) \\ &-\ \delta^{(2)}\Big(\frac{\vec{k}_\perp}{2} - \vec{P} + \vec{l}\,\Big) - \delta^{(2)}\Big(\frac{\vec{k}_\perp}{2} + \vec{P} - \vec{l}\,\Big) \Bigg\} \Bigg|^2. \end{aligned} \tag{A.5}$$

From the Dirac δ property it follows that:
$\vec{l} = \vec{P}_\perp \pm (\vec{\Delta}_\perp)/2$ for the exchange of both gluons with the same quark
$\vec{l} = \vec{P}_\perp \pm (\vec{k}_\perp)/2$ for the exchange of each gluon with that other quark.
That finally leads to

$$\begin{aligned}\frac{d\sigma(\gamma^*_{\lambda_\gamma} p \to Q\bar{Q}p; s_{\gamma p})}{dz d^2\vec{P}_\perp d^2\vec{\Delta}_\perp} &= \overline{\sum_{\lambda_\gamma, \lambda, \bar{\lambda}}} \Bigg| \int d^2\vec{k}_\perp f\Big(Y, \frac{\vec{\Delta}_\perp}{2} + \vec{k}_\perp, \frac{\vec{\Delta}_\perp}{2} - \vec{k}_\perp\Big) \\ &\times \Big\{ \Psi^{\lambda_\gamma}_{\lambda\bar{\lambda}}(z, \vec{P}_\perp + \vec{\Delta}_\perp) + \Psi^{\lambda_\gamma}_{\lambda\bar{\lambda}}(z, \vec{P}_\perp + \vec{\Delta}_\perp) \\ &- \Psi^{\lambda_\gamma}_{\lambda\bar{\lambda}}(z, \vec{P}_\perp + \vec{k}_\perp) - \Psi^{\lambda_\gamma}_{\lambda\bar{\lambda}}(z, \vec{P}_\perp - \vec{k}_\perp) \Big\} \Bigg|^2 . \end{aligned} \tag{A.6}$$

Moreover, the light-front wave function from the above equation is expressed by longitudinal and transverse terms according to Ref. [91], which are as follows:

$$\Psi_L^{\gamma^* \to q\bar{q}}(\vec{k}_\perp, z) = \frac{eZ_f [z(1-z)]^{3/2} \delta_{ij} 2Q (1 - \delta_{\sigma\sigma'})}{\vec{k}^2_\perp + m_f^2 + Q^2 z(1-z)} . \tag{A.7}$$

and

$$\Psi^{\lambda_\gamma}_{\lambda\bar{\lambda}}(z, \vec{r}_\perp) = \frac{1}{\sqrt{4\pi z(1-z)}} \int \frac{d^2\vec{l}_\perp}{(2\pi)^2} e^{i\vec{r}_\perp \cdot \vec{l}_\perp} \, \Psi^{\lambda_\gamma}_{\lambda\bar{\lambda}}(z, \vec{l}_\perp) \, . \tag{A.8}$$

Appendix B

The azimuthal integration in the convolution of the hard amplitude

This appendix is an extension to Chapter 3.

Several steps necessary to analytically perform the azimuthal integration in the convolution of the hard amplitude with the azimuthally asymmetric part of the gluon GTMD are summarized here. The gluon GTMD is expanded as

$$\begin{aligned}
T(Y,\vec{k}_\perp,\vec{\Delta}_\perp) &= T_0(Y,k_\perp,\Delta_\perp) + 2\,\cos 2(\phi_k-\phi_\Delta)\,T_\epsilon(Y,k_\perp,\Delta_\perp) \\
&= T_0(Y,k_\perp,\Delta_\perp) + 2\,\frac{2(\vec{k}_\perp\cdot\vec{\Delta}_\perp)^2 - k_\perp^2\Delta_\perp^2}{k_\perp^2\Delta_\perp^2}\,T_\epsilon(Y,k_\perp,\Delta_\perp)\,, \qquad \text{(B.1)}
\end{aligned}$$

while the parts of the amplitudes that are interesting for this calculation are

$$\begin{aligned}
\delta\vec{\mathcal{M}}_0(\vec{P}_\perp,\vec{\Delta}_\perp) &= 2\int\frac{d^2\vec{k}_\perp}{2\pi}\,\frac{\vec{P}_\perp-\vec{k}_\perp}{(\vec{P}_\perp-\vec{k}_\perp)^2+m_Q^2}\,\frac{2(\vec{k}_\perp\cdot\vec{\Delta}_\perp)^2-k_\perp^2\Delta_\perp^2}{k_\perp^2\Delta_\perp^2}\,T_\epsilon(Y,k_\perp,\Delta_\perp) \\
&= 2\left(2\frac{\Delta_\perp^i\Delta_\perp^j}{\Delta_\perp^2}-\delta_{ij}\right)\int\frac{d^2\vec{k}_\perp}{2\pi}\,\frac{\vec{P}_\perp-\vec{k}_\perp}{(\vec{P}_\perp-\vec{k}_\perp)^2+m_Q^2} \\
&\times\ \frac{k_\perp^i k_\perp^j}{k_\perp^2}\,T_\epsilon(Y,k_\perp,\Delta_\perp)\,, \\
\delta\vec{\mathcal{M}}_1(\vec{P}_\perp,\vec{\Delta}_\perp) &= 2\left(2\frac{\Delta_\perp^i\Delta_\perp^j}{\Delta_\perp^2}-\delta_{ij}\right)\int\frac{d^2\vec{k}_\perp}{2\pi}\,\frac{1}{(\vec{P}_\perp-\vec{k}_\perp)^2+m_Q^2} \\
&\times\ \frac{k_\perp^i k_\perp^j}{k_\perp^2}\,T_\epsilon(Y,k_\perp,\Delta_\perp)\,. \qquad \text{(B.2)}
\end{aligned}$$

The integral over azimuthal angles are as follows

$$\begin{aligned}\vec{I}_{ij} &= \int_0^{2\pi} \frac{d\phi_k}{2\pi} \frac{\vec{P}_\perp - \vec{k}_\perp}{(\vec{P}_\perp - \vec{k}_\perp)^2 + m_Q^2} \frac{k_\perp^i k_\perp^j}{k_\perp^2}, \\ I_{ij}^1 &= \int_0^{2\pi} \frac{d\phi_k}{2\pi} \frac{1}{(\vec{P}_\perp - \vec{k}_\perp)^2 + m_Q^2} \frac{k_\perp^i k_\perp^j}{k_\perp^2}\,. \end{aligned} \tag{B.3}$$

This vector integral will be proportional to $\vec{P}_\perp$. Therefore it could be written

$$\vec{I}_{ij} = \frac{\vec{P}_\perp}{P_\perp} I_{ij}^0(\vec{P}_\perp, k_\perp)\,, \tag{B.4}$$

with

$$I_{ij}^0(\vec{P}_\perp, k_\perp) = \frac{1}{P_\perp} \int_0^{2\pi} \frac{d\phi_k}{2\pi} \frac{P_\perp^2 - \vec{P}_\perp \cdot \vec{k}_\perp}{(\vec{P}_\perp - \vec{k}_\perp)^2 + m_Q^2} \frac{k_\perp^i k_\perp^j}{k_\perp^2}\,. \tag{B.5}$$

Then $I_{ij}^{0,1}$ should be decomposed into invariant functions $|\vec{P}_\perp|$ and $|\vec{k}_\perp|$, and two orthogonal tensor structures for which

$$I_{ij}^{0,1}(\vec{P}_\perp) = \Big(2\frac{P_\perp^i P_\perp^j}{P_\perp^2} - \delta_{ij}\Big)\frac{1}{2} I_\epsilon^{0,1}(P_\perp, k_\perp) + \delta_{ij}\,\frac{1}{2} I_0^{0,1}(P_\perp, k_\perp)\,. \tag{B.6}$$

When inserting this into Eq. (B.2), the contraction with δ_{ij} vanishes, and it is obtained that

$$\begin{aligned}\delta\vec{\mathcal{M}}_0(\vec{P}_\perp, \vec{\Delta}_\perp) &= 2\Big(2\frac{(\vec{P}_\perp \cdot \vec{\Delta}_\perp)^2}{P_\perp^2 \Delta_\perp^2} - 1\Big)\,\frac{\vec{P}_\perp}{P_\perp} \int_0^\infty k_\perp dk_\perp\, I_\epsilon^0(P_\perp, k_\perp)\, T_\epsilon(Y, k_\perp, \Delta_\perp) \\ &= \frac{\vec{P}_\perp}{P_\perp}\, 2\cos 2(\phi_\Delta - \phi_P) \int_0^\infty k_\perp dk_\perp\, I_\epsilon^0(P_\perp, k_\perp)\, T_\epsilon(Y, k_\perp, \Delta_\perp). \end{aligned} \tag{B.7}$$

It also needs to find the expression for the azimuthal integral $I_\epsilon(P_\perp, k_\perp)$. To do so, lets introduce the following

$$a = P_\perp^2 + k_\perp^2 + m^2\,, \qquad b = 2P_\perp k_\perp\,, \tag{B.8}$$

so that it is obtained

$$I_\epsilon^1(P_\perp, k_\perp) = \int_0^{2\pi} \frac{d\phi}{2\pi} \frac{\cos 2\phi}{a - b\cos\phi} \equiv g(a,b)\,, \tag{B.9}$$

and

$$\begin{aligned} P_\perp I^0_\epsilon(P_\perp, k_\perp) &= \int_0^{2\pi} \frac{d\phi}{2\pi} \frac{P_\perp^2 - \frac{1}{2} b\cos\phi}{a - b\cos\phi} \cos 2\phi \\ &= \int_0^{2\pi} \frac{d\phi}{2\pi} \frac{P_\perp^2 - \frac{1}{2}a + \frac{1}{2}(a - b\cos\phi)}{a - b\cos\phi} \cos 2\phi \\ &= (P_\perp^2 - \frac{1}{2}a) \int_0^{2\pi} \frac{d\phi}{2\pi} \frac{\cos 2\phi}{a - b\cos\phi} \\ &= \frac{1}{2}(P_\perp^2 - k_\perp^2 - m^2) g(a,b)\,, \end{aligned} \tag{B.10}$$

where

$$\begin{aligned} g(a,b) &= \frac{1}{b^2} \frac{2a^2 - b^2 - 2a\sqrt{a^2 - b^2}}{\sqrt{a^2 - b^2}} = \frac{1}{2P_\perp^2 k_\perp^2} \\ &\times \Big(\frac{(P_\perp^2 + k_\perp^2 + m_Q^2)^2 - 2P_\perp^2 k_\perp^2}{\sqrt{(P_\perp^2 - k_\perp^2 - m_Q^2)^2 + 4P_\perp^2 m_Q^2}} - (P_\perp^2 + k_\perp^2 + m_Q^2) \Big). \end{aligned} \tag{B.11}$$

This finally leads to getting an identity

$$a^2 - b^2 = (P_\perp^2 + k_\perp^2 + m^2)^2 - 4P_\perp^2 k_\perp^2 = (P_\perp^2 - k_\perp^2 - m^2)^2 + 4P_\perp^2 m^2\,. \tag{B.12}$$

References

[1] A. Szczurek, B. Linek, and M. Łuszczak, “Semiexclusive dilepton production in proton-proton collisions with one forward proton measurement at the LHC,” *Phys. Rev. D*, vol. 104, p. 074009, Oct 2021.

[2] B. Linek, M. Łuszczak, W. Schäfer, and A. Szczurek, “Two-photon Fusion Production of e^+e^- in Proton–Lead Collision,” *Acta Phys. Polon. Supp.*, vol. 16, no. 7, pp. 7–A29, 2023.

[3] B. Linek, A. Łuszczak, M. Łuszczak, R. Pasechnik, W. Schäfer, and A. Szczurek, “Probing proton structure with $c\bar{c}$ correlations in ultraperipheral pA collisions,” *JHEP*, 2023.

[4] B. Linek, M. Łuszczak, W. Schäfer, and A. Szczurek, “Probing gluon gtmds of the proton in deep inelastic diffractive dijet production at HERA,” *Phys. Rev. D*, vol. 110, p. 054027, Sep 2024.

[5] A. Szczurek, B. Linek, and M. Luszczak, “Central dilepton production in proton-proton collisions with rapidity gap and with forward protons,” *SciPost Phys. Proc.*, p. 083, 2022.

[6] A. Szczurek, B. Linek, and M. Luszczak, “Production of dileptons via photon-photon fusion in proton-proton collisions with one forward proton measurement,” in *Proceedings of Science*, 2021.

[7] B. Linek, “Semiexclusive dilepton production in proton-proton collisions with one forward proton measurement at the LHC,” in *Low-x Workshop 2021*, 6 2022.

[8] B. Linek, M. Łuszczak, W. Schäfer, and A. Szczurek, “Two-photon Fusion Production of e^+e^- in Proton–Lead Collision,” *Acta Phys. Polon. Supp.*, vol. 16, no. 7, pp. 7–A29, 2023.

[9] O. Nachtmann, A. Lahee, and W. Wetzel, *Elementary Particle Physics: Concepts and Phenomena.* Theoretical and Mathematical Physics, Springer Berlin Heidelberg, 2012.

[10] S. Bailey, T. Cridge, L. A. Harland-Lang, A. D. Martin, and R. S. Thorne, “Parton distributions from LHC, HERA, Tevatron and fixed target data: MSHT20 PDFs,” *Eur. Phys. J C*, vol. 81, p. 341, 2021.

[11] S. Bethke, “Experimental tests of asymptotic freedom,” *Progress in Particle and Nuclear Physics*, vol. 58, no. 2, pp. 351–386, 2007.

[12] S. Chatrchyan *et al.*, “Measurement of the ratio of the inclusive 3-jet cross section to the inclusive 2-jet cross section in pp collisions at $\sqrt{s} = 7$ TeV and first determination of the strong coupling constant in the TeV range,” *Eur. Phys. J C*, vol. 73, p. 2604, 2013.

[13] V. N. Gribov and L. N. Lipatov, “Deep inelastic ep scattering in perturbation theory,” *Sov. J. Nucl. Phys.*, vol. 15, pp. 438–450, 1972.

[14] Y. L. Dokshitzer, “Calculation of the Structure Functions for Deep Inelastic Scattering and e^+e^- Annihilation by Perturbation Theory in Quantum Chromodynamics.,” *Sov. Phys. JETP*, vol. 46, pp. 641–653, 1977.

[15] G. Altarelli and G. Parisi, “Asymptotic Freedom in Parton Language,” *Nucl. Phys. B*, vol. 126, pp. 298–318, 1977.

[16] A. V. Lipatov and N. P. Zotov, “Charm photoproduction at desy HERA: k_T factorization versus experimental data,” *Phys. Rev. D*, vol. 75, p. 014028, Jan 2007.

[17] M. Łuszczak and A. Szczurek, “Charm quark–antiquark correlations in photon–proton scattering,” *Phys. Lett. B*, vol. 594, no. 3, pp. 291–298, 2004.

[18] V. A. Saleev and A. V. Shipilova, “Inclusive b-jet and $b\bar{b}$-dijet production at the LHC via reggeized gluons,” *Phys. Rev. D*, vol. 86, p. 034032, Aug 2012.

[19] B. A. Kniehl, A. V. Shipilova, and V. A. Saleev, “Open charm production at high energies and the quark reggeization hypothesis,” *Phys. Rev. D*, vol. 79, p. 034007, Feb 2009.

[20] J. Kwiecinski, A. D. Martin, and A. M. Stasto, “Unified BFKL and Gribov-Lipatov-Altarelli-Parisi description of F_2 data,” *Phys. Rev. D*, vol. 56, pp. 3991–4006, Oct 1997.

[21] H. Jung and G. Salam, “Hadronic final state predictions from ccfm: the hadron-level monte carlo generator cascade,” *Eur. Phys. J C - Particles and Fields*, vol. 19, pp. 351–360, Feb 2001.

[22] B. A. Kniehl, V. A. Saleev, and A. V. Shipilova, “Inclusive b and $b\bar{b}$ production with quasi-multi-Regge kinematics at the tevatron,” *Phys. Rev. D*, vol. 81, p. 094010, May 2010.

[23] M. A. Kimber, A. D. Martin, and M. G. Ryskin, “Unintegrated parton distributions,” *Phys. Rev. D*, vol. 63, p. 114027, May 2001.

[24] G. Watt, A. D. Martin, and M. G. Ryskin, “Unintegrated parton distributions and inclusive jet productionat HERA,” *Eur. Phys. J C - Particles and Fields*, vol. 31, pp. 73–89, Oct 2003.

[25] L. Frankfurt, V. Guzey, A. Stasto, and M. Strikman, “Selected topics in diffraction with protons and nuclei: past, present, and future,” *Reports on Progress in Physics*, vol. 85, p. 126301, Oct 2022.

[26] L. A. Harland-Lang, V. A. Khoze, and M. G. Ryskin, “The photon PDF in events with rapidity gaps,” *Eur. Phys. J C*, vol. 76, p. 255, 2016.

[27] G. Aad *et al.*, “Observation and measurement of forward proton scattering in association with lepton pairs produced via the photon fusion mechanism at atlas,” *Phys. Rev. Lett.*, vol. 125, p. 261801, Dec 2020.

[28] ATLAS Collaboration, “ATLAS Forward Detectors for Measurement of Elastic Scattering and Luminosity: Technical Design Report,” atlas-tdr-18; cern-lhcc-2008-004, CERN, 2008.

[29] M. Vatrt, “Development, Application and Representation of Algorithms for Discoveries with the ATLAS Forward Proton (AFP) Detector at CERN,” Master’s thesis, CERN, May 2019. Presented 20 May 2019.

[30] ATLAS Collaboration, “Technical Design Report for the ATLAS Forward Proton Detector,” Tech. Rep. CERN-LHCC-2015-009. ATLAS-TDR-024, CERN, May 2015.

[31] R. Gemme *et al.*, “Commissioning and calibration of the zero degree calorimeters for the ALICE experiment,” *Nucl. Phys. B Proc. Suppl.*, vol. 197, pp. 211–214, 2009.

[32] C. Oppedisano *et al.*, “Physics performance of the ALICE zero degree calorimeter,” *Nucl. Phys. B Proc. Suppl.*, vol. 197, pp. 206–210, 2009.

[33] G. Puddu *et al.*, “Erratum to: "The zero degree calorimeters for the ALICE experiment” [nucl. instr. and meth. a 581 (2007) 397–401],” *Nuclear Instruments and Methods in Physics Research Section A: Accelerators, Spectrometers, Detectors and Associated Equipment*, vol. 604, no. 3, p. 765, 2009.

[34] M. Glück, C. Pisano, and E. Reya, “The polarized and unpolarized photon content of the nucleon,” *Phys. Lett. B*, vol. 540, no. 1, pp. 75–80, 2002.

[35] A. D. Martin, R. G. Roberts, W. J. Stirling, and R. S. Thorne, “Parton distributions incorporating QED contributions,” *Eur. Phys. J. C*, vol. 39, pp. 155–161, 2005.

[36] A. Martin and M. Ryskin, “The photon PDF of the proton,” *Eur. Phys. J. C*, vol. 74, 06 2014.

[37] R. D. Ball *et al.*, “Parton distributions with QED corrections,” *Nuc, Phys. B*, vol. 877, no. 2, pp. 290–320, 2013.

[38] C. Schmidt, J. Pumplin, D. Stump, and C. P. Yuan, “QED effects and Photon PDF in the CTEQ-TEA Global Analysis,” *PoS*, vol. DIS2014, p. 054, 2014.

[39] G. G. da Silveira, L. Forthomme, K. Piotrzkowski, W. Schäfer, and A. Szczurek, “Central $\mu^+\mu^-$ production via photon-photon fusion in proton-proton collisions with proton dissociation,” *JHEP*, vol. 1502, p. 159, 2015.

[40] V. M. Budnev, I. F. Ginzburg, G. V. Meledin, and V. G. Serbo, “The Two photon particle production mechanism. Physical problems. Applications. Equivalent photon approximation,” *Phys. Rept.*, vol. 15, pp. 181–281, 1975.

[41] H. Abramowicz, E. M. Levin, A. Levy, and U. Maor, "A parametrization of $\sigma T\ (\gamma^{*} p)$ above the resonance region for $Q^2 \geq 0$," *Phys. Lett. B*, vol. 269, pp. 465–476, 1991.

[42] H. Abramowicz and A. Levy, "The ALLM parameterization of sigma(tot)(gamma* p): An Update," *arXiv e-prints*, 12 1997.

[43] R. Fiore, A. Flachi, L. L. Jenkovszky, A. I. Lengyel, and V. K. Magas, "Explicit model realizing parton hadron duality," *Eur. Phys. J. A*, vol. 15, pp. 505–515, 2002.

[44] M. M. Block, L. Durand, and P. Ha, "Connection of the virtual $\gamma^{*} p$ cross section of ep deep inelastic scattering to real γp scattering, and the implications for νn and ep total cross sections," *Phys. Rev. D*, vol. 89, p. 094027, May 2014.

[45] A. Suri and D. R. Yennie, "The space-time phenomenoglogy of photon absorption and inelastic electron scattering," *Annals Phys.*, vol. 72, p. 243, 1972.

[46] M. Łuszczak, W. Schäfer, and A. Szczurek, "Two-photon dilepton production in proton-proton collisions: Two alternative approaches," *Phys. Rev. D*, vol. 93, p. 074018, Apr 2016.

[47] A. V. Manohar, P. Nason, G. P. Salam, and G. Zanderighi, "The photon content of the proton," *JHEP*, vol. 2017, p. 46, 2017.

[48] A. Manohar, P. Nason, G. P. Salam, and G. Zanderighi, "How bright is the proton? A precise determination of the photon parton distribution function," *Phys. Rev. Lett.*, vol. 117, no. 24, p. 242002, 2016.

[49] E. Bartoš, S. R. Gevorkyan, E. A. Kuraev, and N. N. Nikolaev, "Lepton pair production in heavy-ion collisions in perturbation theory," *Phys. Rev. A*, vol. 66, p. 042720, Oct 2002.

[50] G. Frolov, V. Gribov, and L. Lipatov, "On the vacuum pole in quantum electrodynamics," *Physics Letters B*, vol. 31, no. 1, pp. 34–35, 1970.

[51] H. Cheng and T. T. Wu, "High-energy production processes in quantum electrodynamics," *Phys. Rev. D*, vol. 1, pp. 456–458, 1970.

[52] F. Scheck, *Electroweak and Strong Interactions*. Springer Berlin, Heidelberg, 10 2011.

[53] P. Faccioli, “Instanton contribution to the electromagnetic form factors of the nucleon,” *Phys. Rev. C*, vol. 69, 06 2004.

[54] S. A. Kulagin and V. V. Barinov, “Hybrid model of proton structure functions,” *Phys. Rev. C*, vol. 105, p. 045204, Apr 2022.

[55] A. M. Sirunyan *et al.*, “Observation of proton-tagged, central (semi)exclusive production of high-mass lepton pairs in pp collisions at 13 TeV with the cms-totem precision proton spectrometer,” *JHEP*, p. 153, July 2018.

[56] L. A. Harland-Lang, M. Tasevsky, V. A. Khoze, and M. G. Ryskin, “A new approach to modelling elastic and inelastic photon-initiated production at the LHC: SuperChic 4,” *Eur. Phys. J C*, vol. 80, p. 925, 2020.

[57] T. Ahmed *et al.*, “Deep inelastic scattering events with a large rapidity gap at HERA,” *Nucl. Phys. B*, vol. 429, pp. 477–502, 1994.

[58] V. A. Khoze, A. D. Martin, and M. G. Ryskin, “Diffraction at the LHC,” *Eur. Phys. J C*, vol. 73, p. 2503, 2013.

[59] M. Łuszczak, W. Schäfer, and A. Szczurek, “Production of W^+W^- pairs via $\gamma^*\gamma^* \to W^+W^-$ subprocess with photon transverse momenta,” *JHEP*, p. 64, 2018.

[60] L. Forthomme, M. Łuszczak, W. Schäfer, and A. Szczurek, “Production of $t\bar{t}$ pairs via $\gamma\gamma$ fusion with photon transverse momenta and proton dissociation,” *JHEP*, p. 100, 2019.

[61] L. Forthomme, M. Łuszczak, W. Schäfer, and A. Szczurek, “Rapidity gap survival factors caused by remnant fragmentation for W^+W^- pair production via $\gamma^*\gamma^* \to W^+W^-$ subprocess with photon transverse momenta,” *Phys. Lett. B*, vol. 789, pp. 300–307, 2019.

[62] M. Kłusek-Gawenda, R. Rapp, W. Schäfer, and A. Szczurek, “Dilepton radiation in heavy-ion collisions at small transverse momentum,” *Phys. Lett. B*, vol. 790, pp. 339–344, 2019.

[63] M. Dyndal, A. Glazov, M. Luszczak, and R. Sadykov, “Probing the photonic content of the proton using photon-induced dilepton production in $p + \mathrm{Pb}$ collisions at the LHC,” *Phys. Rev. D*, vol. 99, p. 114008, Jun 2019.

[64] S. Acharya *et al.*, “Dielectron production in proton-proton and proton-lead collisions at $\sqrt{s_{\mathrm{NN}}} = 5.02\,\mathrm{TeV}$,” *Phys. Rev. C*, vol. 102, p. 055204, Nov 2020.

[65] S. R. Klein, J. Nystrand, J. Seger, Y. Gorbunov, and J. Butterworth, “Starlight: A monte carlo simulation program for ultra-peripheral collisions of relativistic ions,” *Computer Physics Communications*, vol. 212, pp. 258–268, 2017.

[66] A. van Hameren, M. Kłusek-Gawenda, and A. Szczurek, “Single- and double-scattering production of four muons in ultraperipheral pbpb collisions at the large hadron collider,” *Physics Letters B*, vol. 776, pp. 84–90, 2018.

[67] L. A. Harland-Lang, V. A. Khoze, M. G. Ryskin, and W. j. Stirling, “Standard candle central exclusive processes at the tevatron and LHC,” *Eur. Phys. J C*, vol. 69, p. 179, 2010.

[68] L. A. Harland-Lang, V. A. Khoze, M. G. Ryskin, and W. j. Stirling, “The phenomenology of central exclusive production at hadron colliders,” *Eur. Phys. J C*, vol. 72, p. 2110, 2012.

[69] D. Ashery, “High momentum diffractive processes and hadronic structure,” *Prog. Part. Nucl. Phys.*, vol. 56, pp. 279–339, 2006.

[70] N. N. Nikolaev and B. G. Zakharov, “Splitting the pomeron into two jets: A Novel process at HERA,” *Phys. Lett. B*, vol. 332, pp. 177–183, 1994.

[71] N. N. Nikolaev, W. Schäfer, and G. Schwiete, “Coherent production of hard dijets on nuclei in QCD,” *Phys. Rev. D*, vol. 63, p. 014020, 2001.

[72] X.-d. Ji, “Viewing the proton through ’color’ filters,” *Phys. Rev. Lett.*, vol. 91, p. 062001, 2003.

[73] A. V. Belitsky, X.-d. Ji, and F. Yuan, “Quark imaging in the proton via quantum phase space distributions,” *Phys. Rev. D*, vol. 69, p. 074014, 2004.

[74] S. Meissner, A. Metz, and M. Schlegel, “Generalized parton correlation functions for a spin-1/2 hadron,” *JHEP*, vol. 08, p. 056, 2009.

[75] C. Lorcé and B. Pasquini, “Structure analysis of the generalized correlator of quark and gluon for a spin-1/2 target,” *JHEP*, vol. 09, p. 138, 2013.

[76] R. Boussarie *et al.*, *TMD Handbook.* JLAB, 4 2023.

[77] Y. Hagiwara, Y. Hatta, and T. Ueda, “Wigner, husimi, and generalized transverse momentum dependent distributions in the color glass condensate,” *Phys. Rev. D*, vol. 94, p. 094036, Nov 2016.

[78] B. Z. Kopeliovich, L. I. Lapidus, and A. B. Zamolodchikov, “Dynamics of Color in Hadron Diffraction on Nuclei,” *JETP Lett.*, vol. 33, pp. 595–597, 1981.

[79] N. Nikolaev and B. G. Zakharov, “Pomeron structure function and diffraction dissociation of virtual photons in perturbative QCD,” *Z. Phys. C*, vol. 53, pp. 331–346, 1992.

[80] Y. Hatta, B.-W. Xiao, and F. Yuan, “Probing the Small- x Gluon Tomography in Correlated Hard Diffractive Dijet Production in Deep Inelastic Scattering,” *Phys. Rev. Lett.*, vol. 116, no. 20, p. 202301, 2016.

[81] D. Boer and C. Setyadi, “GTMD model predictions for diffractive dijet production at EIC,” *Phys. Rev. D*, vol. 104, no. 7, p. 074006, 2021.

[82] T. Altinoluk, N. Armesto, G. Beuf, and A. H. Rezaeian, “Diffractive Dijet Production in Deep Inelastic Scattering and Photon-Hadron Collisions in the Color Glass Condensate,” *Phys. Lett. B*, vol. 758, pp. 373–383, 2016.

[83] H. Mäntysaari, N. Mueller, and B. Schenke, “Diffractive Dijet Production and Wigner Distributions from the Color Glass Condensate,” *Phys. Rev. D*, vol. 99, no. 7, p. 074004, 2019.

[84] F. Salazar and B. Schenke, “Diffractive dijet production in impact parameter dependent saturation models,” *Phys. Rev. D*, vol. 100, no. 3, p. 034007, 2019.

[85] Y. Hagiwara, Y. Hatta, R. Pasechnik, M. Tasevsky, and O. Teryaev, “Accessing the gluon Wigner distribution in ultraperipheral pA collisions,” *Phys. Rev. D*, vol. 96, no. 3, p. 034009, 2017.

[86] M. Reinke Pelicer, E. Gräve De Oliveira, and R. Pasechnik, “Exclusive heavy quark-pair production in ultraperipheral collisions,” *Phys. Rev. D*, vol. 99, no. 3, p. 034016, 2019.

[87] R. Staszewski, “Forward proton physics at LHC,” in *30th International Workshop on Deep-Inelastic Scattering and Related Subjects*, 9 2023.

[88] M. Trzebinski, “Prospects for Proton-Proton Measurements with Tagged Protons in ATLAS,” in *International Conference on the Structure and the Interactions of the Photon*, pp. 144–149, 2019.

[89] E. Bossini, “The CMS Precision Proton Spectrometer: Precision timing with sc-CVD diamond crystals,” *Nucl. Instrum. Meth. A*, vol. 1047, p. 167823, 2023.

[90] M. Abramowitz and I. Stegun, *Handbook of Mathematical Functions: with Formulas, Graphs, and Mathematical Tables*. Dover Books on Mathematics, Dover Publications, 2012.

[91] Y. V. Kovchegov and E. Levin, “Quantum chromodynamics at high energy,” *Cambridge University Press*, vol. 33, p. ISBN:9780521112574, 2012.

[92] V. Barone and E. Predazzi, *High-Energy Particle Diffraction*, vol. v.565 of *Texts and Monographs in Physics*. Berlin Heidelberg: Springer-Verlag, 2002.

[93] N. N. Nikolaev and B. G. Zakharov, “On determination of the large 1/x gluon distribution at HERA,” *Phys. Lett. B*, vol. 332, pp. 184–190, 1994.

[94] N. N. Nikolaev, A. V. Pronyaev, and B. G. Zakharov, “Azimuthal asymmetry as a new handle on σ_L/σ_T in diffractive DIS,” *Phys. Rev. D*, vol. 59, p. 091501, 1999.

[95] Y. Hagiwara, Y. Hatta, and T. Ueda, “Wigner, Husimi, and generalized transverse momentum dependent distributions in the color glass condensate,” *Phys. Rev. D*, vol. 94, no. 9, p. 094036, 2016.

[96] I. P. Ivanov, N. N. Nikolaev, and A. A. Savin, “Diffractive vector meson production at HERA: From soft to hard QCD,” *Phys. Part. Nucl.*, vol. 37, pp. 1–85, 2006.

[97] B. Z. Kopeliovich, H. J. Pirner, A. H. Rezaeian, and I. Schmidt, “Azimuthal anisotropy of direct photons,” *Phys. Rev. D*, vol. 77, p. 034011, 2008.

[98] K. J. Golec-Biernat and M. Wüsthoff, “Saturation effects in deep inelastic scattering at low Q^2 and its implications on diffraction,” *Phys. Rev. D*, vol. 59, p. 014017, 1998.

[99] L. S. Moriggi, G. M. Peccini, and M. V. T. Machado, "Investigating the inclusive transverse spectra in high-energy pp collisions in the context of geometric scaling framework," *Phys. Rev. D*, vol. 102, no. 3, p. 034016, 2020.

[100] I. Balitsky, "Operator expansion for high-energy scattering," *Nucl. Phys. B*, vol. 463, pp. 99–160, 1996.

[101] Y. V. Kovchegov, "Small x F(2) structure function of a nucleus including multiple pomeron exchanges," *Phys. Rev. D*, vol. 60, p. 034008, 1999.

[102] K. J. Golec-Biernat and A. M. Stasto, "On solutions of the Balitsky-Kovchegov equation with impact parameter," *Nucl. Phys. B*, vol. 668, pp. 345–363, 2003.

[103] J. Berger and A. Stasto, "Numerical solution of the nonlinear evolution equation at small x with impact parameter and beyond the LL approximation," *Phys. Rev. D*, vol. 83, p. 034015, 2011.

[104] J. Berger and A. M. Stasto, "Small x nonlinear evolution with impact parameter and the structure function data," *Phys. Rev. D*, vol. 84, p. 094022, 2011.

[105] S. S. Gubser, "Conformal symmetry and the Balitsky-Kovchegov equation," *Phys. Rev. D*, vol. 84, p. 085024, 2011.

[106] L. D. McLerran and R. Venugopalan, "Gluon distribution functions for very large nuclei at small transverse momentum," *Phys. Rev. D*, vol. 49, pp. 3352–3355, 1994.

[107] E. Iancu and A. H. Rezaeian, "Elliptic flow from color-dipole orientation in pp and pA collisions," *Phys. Rev. D*, vol. 95, no. 9, p. 094003, 2017.

[108] H. Mäntysaari, K. Roy, F. Salazar, and B. Schenke, "Gluon imaging using azimuthal correlations in diffractive scattering at the Electron-Ion Collider," *Phys. Rev. D*, vol. 103, no. 9, p. 094026, 2021.

[109] H. Kowalski and D. Teaney, "An Impact parameter dipole saturation model," *Phys. Rev. D*, vol. 68, p. 114005, 2003.

[110] V. P. Gonçalves, G. Sampaio dos Santos, and C. R. Sena, "Exclusive heavy quark photoproduction in pp, pPb and $PbPb$ collisions at the LHC and FCC energies," *Nucl. Phys. A*, vol. 1000, p. 121862, 2020.

[111] Y. Hatta, B.-W. Xiao, F. Yuan, and J. Zhou, “Azimuthal angular asymmetry of soft gluon radiation in jet production,” *Phys. Rev. D*, vol. 104, no. 5, p. 054037, 2021.

[112] R. Aaij *et al.*, “Measurement of differential $b\bar{b}$- and $c\bar{c}$-dijet cross-sections in the forward region of pp collisions at $\sqrt{s}$ = 13 TeV,” *JHEP*, vol. 02, p. 023, 2021.

[113] R. Maciula and A. Szczurek, “Far-forward production of charm mesons and neutrinos at forward physics facilities at the LHC and the intrinsic charm in the proton,” *Phys. Rev. D*, vol. 107, no. 3, p. 034002, 2023.

[114] P. Newman and M. Wing, “The Hadronic Final State at HERA,” *Rev. Mod. Phys.*, vol. 86, no. 3, p. 1037, 2014.

[115] F. Aaron *et al.*, “Measurement of dijet production in diffractive deep-inelastic scattering with a leading proton at HERA,” *Eur. Phys. J C*, vol. 72, p. 1970, 2012.

[116] H. Abramowicz *et al.*, “Production of exclusive dijets in diffractive deep inelastic scattering at HERA,” *Eur. Phys. J C*, vol. 76, p. 16, 2016.

[117] M. Wüsthoff and A. D. Martin, “The QCD description of diffractive processes,” *J. Phys. G*, vol. 25, pp. R309–R344, 1999.

[118] L. Frankfurt, V. Guzey, A. Staśto, and M. Strikman, “Selected topics in diffraction with protons and nuclei: past, present, and future,” *Rept. Prog. Phys.*, vol. 85, no. 12, p. 126301, 2022.

[119] R. Boussarie, A. V. Grabovsky, L. Szymanowski, and S. Wallon, “Towards a complete next-to-logarithmic description of forward exclusive diffractive dijet electroproduction at HERA: Real corrections,” *Phys. Rev. D*, vol. 100, p. 074020, Oct 2019.

[120] D. Boer and C. Setyadi, “Probing gluon GTMDs through exclusive coherent diffractive processes,” *Eur. Phys. J. C*, vol. 83, no. 10, p. 890, 2023.

[121] V. Guzey and M. Klasen, “Inclusive dijet photoproduction in ultraperipheral heavy ion collisions at the CERN Large Hadron Collider in next-to-leading order QCD,” *Phys. Rev. C*, vol. 99, no. 6, p. 065202, 2019.

[122] D. Britzger, J. Currie, T. Gehrmann, A. Huss, J. Niehues, and R. Žlebčík, "Dijet production in diffractive deep-inelastic scattering in next-to-next-to-leading order QCD," *Eur. Phys. J. C*, vol. 78, no. 7, p. 538, 2018.

[123] R. Pasechnik and M. Taševský, "Multi-dimensional hadron structure through the lens of gluon Wigner distribution," *ADS Abstract Service*, 10 2023.

[124] M. Łuszczak, R. Maciuła, and A. Szczurek, "Single- and central-diffractive production of open charm and bottom mesons at the LHC: theoretical predictions and experimental capabilities," *Phys. Rev. D*, vol. 91, no. 5, p. 054024, 2015.

[125] J. Bartels, H. Jung, and M. Wüsthoff, "Quark - anti-quark gluon jets in DIS diffractive dissociation," *Eur. Phys. J. C*, vol. 11, pp. 111–125, 1999.

[126] Y. Hatta, N. Mueller, T. Ueda, and F. Yuan, "QCD resummation in hard diffractive dijet production at the electron-ion collider," *Phys. Lett. B*, vol. 802, p. 135211, 03 2020.

[127] M. Arratia, Y. Song, F. Ringer, and B. V. Jacak, "Jets as precision probes in electron-nucleus collisions at the future electron-ion collider," *Phys. Rev. C*, vol. 101, p. 065204, Jun 2020.

[128] M. Arratia, Z.-B. Kang, A. Prokudin, and F. Ringer, "Jet-based measurements of sivers and collins asymmetries at the future electron-ion collider," *Phys. Rev. D*, vol. 102, p. 074015, Oct 2020.

[129] R. Abdul Khalek *et al.*, "Science requirements and detector concepts for the electron-ion collider: EIC yellow report," *Nuc, Phys. A*, vol. 1026, p. 122447, 2022.

[130] B. S. Page, X. Chu, and E. C. Aschenauer, "Experimental aspects of jet physics at a future EIC," *Phys. Rev. D*, vol. 101, p. 072003, Apr 2020.

Załącznik nr 4 do Zarządzenia nr 228/2021 Rektora Uniwersytetu Rzeszowskiego z dnia 1 grudnia 2021 roku w sprawie ustalenia procedury antyplagiatowej w Uniwersytecie Rzeszowskim

OŚWIADCZENIE DOKTORANTA/ OSOBY UBIEGAJĄCEJ SIĘ O NADANIE STOPNIA DOKTORA

Barbara Angelika Linek
Imię (imiona) i nazwisko

Instytut Nauk Fizycznych, Uniwersytet Rzeszowski
Nazwa jednostki

Nauki fizyczne
nazwa dyscypliny

Oświadczam, że moja rozprawa doktorska pt: **Photon induced processes for LHC and EIC energies**

1) została przygotowana przeze mnie samodzielnie*,
2) nie narusza praw autorskich w rozumieniu ustawy z dnia 4 lutego 1994 roku o prawie autorskim i prawach pokrewnych (t.j. Dz.U. z 2021 r., poz. 1062) oraz dóbr osobistych chronionych prawem cywilnym,
3) nie zawiera danych i informacji, które uzyskałem/am w sposób niedozwolony,
4) nie była podstawą nadania tytułu zawodowego lub stopnia naukowego ani mnie ani innej osobie.

Ponadto oświadczam, że treść pracy przedstawionej przeze mnie do obrony, zawarta na przekazywanym nośniku elektronicznym, jest identyczna z wersją drukowaną.

Rzeszów, 23.09.2024 r.
(miejscowość, data)

Barbara Linek
(czytelny podpis autora pracy)

* *uwzględniając merytoryczny wkład promotora pracy*